eman ta zabal zazu

Universidad del País Vasco

Euskal Herriko Unibertsitatea

The Sm-Fe-V based 1:12 permanent magnets

a thesis submitted for the degree of Doctor by

Ana Maria Schonhobel Sanchez

Under the supervision of

Prof. Dr. José Manuel Barandiarán

the co-supervision of

Dr. Rajasekhar Madugundo

Facultad de Ciencia y Tecnologia,

Leioa, August 2019

ZTF-FCT

Zientzia eta Teknologia Fakultatea

Facultad de Ciencia y Tecnología

The Sm-Fe-V based 1:12 Permanent Magnets

Abstract

Keywords: Permanent magnets, $ThMn_{12}$, rare-earths, Sm-Fe-V

Permanent magnets (PMs) are magnetic materials that do not require a continuous supply of electrical energy to maintain an external magnetic field. Today they are particularly important for clean energy applications such as electric car motors and wind turbines. To maximize the energy and resource efficiency, they should be based on materials with high intrinsic magnetic properties, i.e. saturation magnetization $\mu_0 M_s > 1.0\ T$, anisotropy constant $K_1 > 10^6$ J/m^3 and Curie temperature $T_C > 250$°C as well as optimized microstructures. A wide range of magnets with different performances are available today in the market for various applications, starting from low performance alnico and ferrite magnets to more powerful magnets based on rare-earths (R) elements. Nevertheless, researchers must now consider the criticality of the constituent elements as a major factor in the development of permanent magnets, as the PMs industry relies on critical R elements, such as Nd, Pr and Dy.

In response to the increasing limitations on critical rare-earth metals supplies [1, 2], a global effort is being devoted to find rare-earth- lean/free magnetic materials suitable for PMs. Recently there has been a renewed interest in the compounds with $ThMn_{12}$-type structure as they contain only a 7.7% of R, compared with 11.8% in $Nd_2Fe_{14}B$ or 10.5% in Sm_2Co_{17} compounds. The need for a stabilizer of the phase also hints for a combination of Fe with some metals such as M = V, Ti, Mo, Cr, W, Al, or Si, so the most general phase composition is $R(Fe,M)_{12}$ (hereafter 1:12).

This thesis aims to the develop of Sm-based magnets with 1:12 structure with the magnetic properties required for permanent magnets applications and a lean use of critical raw materials. For this purpose, the thesis has been divided in three chapters of results (i) study of the intrinsic

properties in Sm-Fe-V systems (ii) development of coercivity and (iii) fabrication of 1:12 Sm-based the magnets.

The first part of the thesis was focused on the 1:12 phase stabilization and improvement of the intrinsic magnetic properties of a series of Sm-based systems. The stability range of the 1:12 was investigated in a series of $SmFe_{12-x}V_x$ by decreasing the stabilizer element V-content from x = 2.0 to 0.5. in an effort to improve the magnetic properties. The alloys were prepared by arc melting followed by long heat-treatments to obtain pure 1:12 phase. The systematic study revealed that the 1:12 was stable for x = 2, 1.5 and 1. The decrease of x from 2.0 to 1.0, increased the T_C from 321 to 361°C, M_s from 83 to 115 Am^2/kg and $\mu_0 H_A$ from 9.8 to 11 T.

The stability of the 1:12 structure was also explored by replacing Sm with another less expensive rare-earth element as Ce, and for a non rare-earth element as Zr. In the first case, a series of $Sm_{1-x}Ce_xFe_9Co_2Ti$ (x = 0.0, 0.25, 0.50, 0.75, 1.0) ribbons were studied by Mössbauer spectroscopy. By using this technique the different chemical environments in the 1:12 crystal lattice were resolved. Also the preference of Co occupation was analyzed when Sm was replaced by Ce. In the second case, the substitution of Zr for Sm in $Sm_{1-x}Zr_xFe_{11}V$ ($x = 0, 0.2, 0.4, 0.6$) bulk demonstrated to be positive. Although higher concentrations of Zr led to the formation of secondary phases such as $ZrFe_2$ and α-(Fe,V), for Zr = 0.6, the $\mu_0 H_A$ = 8.8 T is still reasonably high, M_s = 138 Am^2/kg and T_C = 310°C.

The second chapter of results deal with transferring the intrinsic properties into extrinsic properties, and the main task consisted in developing coercivity on stoichiometric and off-stoichiometric $SmFe_{10}V_2$ alloys. Two approaches were used to achieve this goal (i) through the refinement of the grains by using powder metallurgy and rapid solidification (ii) via bulk hardening by the precipitation of the eutectic Sm-La phase. The best route to achieve this goal involved a series of steps such as arc melting⟶homogenization of the 1:12→amorphization of the alloy by mechanical milling→ crystallization of the 1:12 phase using short heat treatments. Following this route, nanocrystalline $Sm_{12}Fe_{73}V_{15}$ powders demonstrated $\mu_0 H_c$ values up to 1 T.

The last chapter of results is devoted to the consolidation of the high-coercivity powders into a bulk magnet using hot compaction and hot deformation. During this process, the bulk material developed the proper microstructure and thus the magnetic properties. The isotropic $Sm_{12}Fe_{73}V_{15}$ magnet exhibited a $\mu_0 H_c$ = 1.06 T, $\mu_0 M_{3T}$ = 0.59 T, $\mu_0 M_r$ = 0.42 T and a $(BH)_{max}$ = 28 kJm^{-3} at 3 T applied field. Magnets with similar composition Sm-Fe-(V,M) (M

= Ti, Mo, Cu) were synthesized in order to investigate the effect on the magnetic properties of $Sm_{12}Fe_{75}V_{13}$ when V was reduced or partially substituted by another transition metal. All the mechanically milled powders were successfully consolidated into fully-dense magnets. The most striking result was that magnets with compositions $Sm_{12}Fe_{76.5}V_{11.5}$ and $Sm_{12}Fe_{73}V_{7.5}Mo_{7.5}$ developed a texture perpendicular to the deformation direction. This kind of behavior is different from that of die-upset Nd-Fe-B magnets, and suggest the use of hot extrusion rather than die-upsetting for the development of bulk magnets.

Acknowledgments

First and foremost I would like to thank my research advisors Manu Barandiarán and Rajasekhar Madugundo for their guidance and all the support over the last three years. Without your encourage and constant feedback this PhD would not have been possible. Your contribution to my professional career and personal development is invaluable.

Gracias a la fundación BCMaterials por la oportunidad de realizar mi tesis en el Pais Vasco, y al grupo administrativo por proporcionarme todo aquello que he necesitado. I greatly thank to the EU Horizon 2020 Programme for funding Novamag and Inapem projects (grants 686056 and 691235), and by extension my Phd work. During my research I had the opportunity to attend to international conferences, visit other universities and meet so many interesting people.

Many thanks to George Hadjipanayis, a big part of this research was done in his lab at University of Delaware. Despite his busy schedule, he never missed the weekly group meetings to see my progress and giving me his advice. To Alex Gabay, for taking care of everything in the lab and make it functional. I gained a lot of experimental skills thanks to you. I am also very grateful to Robert Schmith for the SEM training and lab support, and to Derrick Allen for his assistance in the mechanical workshop.

No podría olvidarme de Garita, quien dedicó parte de su tiempo a explicarme los ajustes Mössbauer, su ayuda y experticia fueron invaluables en esta tesis. Gracias también a las personas de servicios generales de la UPV/EHU, en especial a Iñaki Orue, quien estuvo siempre atento a cualquier incoveniente que tuviese con las medidas magnéticas, y a Aitor Larrañaga por las mediciones de rayos X.

También agradecer a mis profesores en Colombia, Germán, Ligia y Anselmo que durante una corta estancia, me prestaron su laboratorio para hacer las medidas Mössbauer a mis muestras. Una mención especial a Luis Alfredo Rodriguez, quien me motivó a aplicar al proyecto ESTEEM3

y que originó a que hiciera medidas mas especializadas de microscopía. También a David Reyes quien fue el que me apoyó haciendo las mediciones de TEM en Tolousse.

How to forget my lab mates in Delaware, thanks Vimal, Shirin and Onur, my stay in USA and Sharp lab would not have been the same without you. To Barry, Rachel and Chris, I really enjoyed our weekly wallyball time. Also my international friends, cubans, dominicans, georgians, colombians and to the talented Maria, I won't forget the Pat's and timothy's nights. Thanks Yarina for listening my many thoughts. You guys, somehow always kept me in balance and made my stay unforgettable. También agradecer a mis compañeros y excompañeros del BC: Dani, Edu, Cristina, Maite, Andrés, Irati, Anabel, Ari y muchos más que en algún momento hicieron este camino más agradable. Como olvidarme de mi amiga Elena, que fue como mi familia durante el primer año de doctorado, su sentido del humor me mantuvo siempre alegre.

Por último, agradecer a mi familia que siempre me han apoyado en cada una de las decisiones que he tomado. Y por supuesto a Richard, no solo por su punto de vista profesional sino por su amor incondicional durante este capítulo de nuestras vidas. Aunque estéis lejos, no podríais estar mas cerca.

A todos ellos, gracias.

Contents

List of Figures

List of Tables

Chapter 1

Introduction

1.1 Permanent magnets

Permanent magnets (PMs) are magnetic materials that retain their magnetization and create an external magnetic field in the absence of an inducing field or current. The use of PMs offer an unbeatable option in producing a magnetic field over other devices (e.g. electromagnets, current carrying conductors) as they do not require a continuous power supply to maintain the magnetic field. If designed properly, once magnetized, the magnet retains its stored energy indefinitely. Currently PMs are used in a wide variety of devices including electronic devices (e.g. mobile phones, audio devices), motors and generators (e.g. hybrid and full electric car motors and wind turbines), data processing (e.g. hard disk drives), medical devices (e.g. magnetic resonance imaging) and even in general home appliances (e.g. washing machines).

The first reference of a magnet dates back to the 6th century B.C, when the natural mineral lodestone, which is just naturally magnetized magnetite (Fe_3O_4), was described as a stone that attracted iron and other lodestones. For many years and centuries, the lodestone magnetism was just a curious natural phenomenon and it was not until 9th century A.D. that chinese developed the first practical application of a magnet, the compass. Despite this early discovery, the development of artificial magnets only started by the end of 1800s, when the foundations of electromagnetism were laid by Maxwell, and it was possible to link the conversion of mechanical energy to electric energy and vice versa. Since then, the efforts to improve the hard magnetic properties has resulted in a nearly exponential increase in the maximum energy product,

$(BH)_{\max}$ (which is a measure of the working strength of a magnet), over the last one hundred years. Fig. 1.1 shows the evolution of PMs.

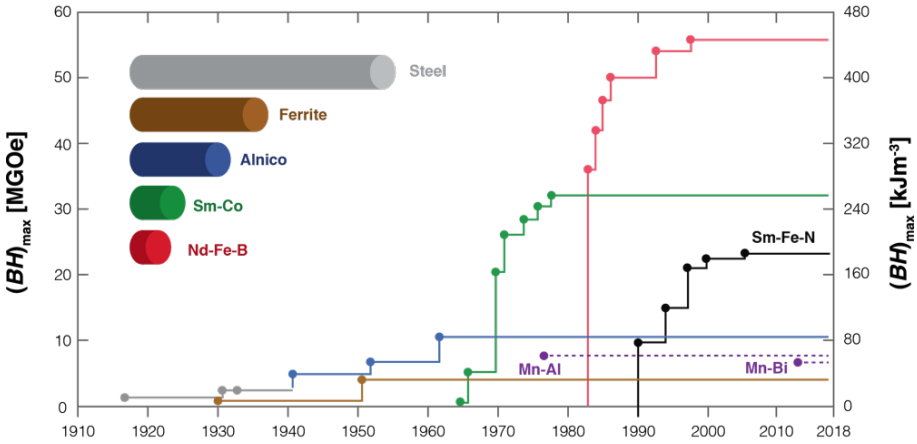

Figure 1.1: Development of permanent magnets, data taken from [3, 4, 5, 6].

Through the first half of the 20th century, most PMs were Fe-based alloys, with the steels being the only PM materials known. In an effort to achieve high remanence (M_{r}), high $(BH)_{\max}$ (see definition on page 5) and greater resistance to demagnetization i.e., coercivity (H_{c}), they were replaced by intermetallic compounds and oxides. The first improvement in the $(BH)_{\max}$ was achieved with the Alnicos. The Alnico magnets were one of the first modern "fine-particle" magnets discovered by Mishima [16] in 1931. The magnetic hardness originates from the shape anisotropy of FeCo-rich magnetic rods which are embedded in a non-magnetic NiAl-rich matrix [17]. This microstructure is obtained through spinodal decomposition after a special heat-treatment. Until here, the permanence of the magnetism was conditional on the magnet's shape.

The shape barrier was broken in the mid 20th century thanks to a different source of anisotropy, the magnetocrystalline anisotropy. In 1950 Philips laboratories patented the first commercial ceramic magnets based on hexagonal ferrites $\mathrm{MFe_{12}O_{19}}$ (M = Sr, Ba) [18]. These magnets are inexpensive, chemically inert, can be produced in any shape but exhibit a low $(BH)_{\max}$ value. The magnetocrystalline anisotropy in hard ferrites produces an easy magnetization direction along the hexagonal c-axis of the unit cell. They exhibit an unusual increase of H_{c} with temperature, making them suitable for applications that require high operating temperatures.

The next breakthrough came with the rare-earth (R) based compounds. First, in the 1960s with the discovery of the $SmCo_5$ and later with the $Nd_2Fe_{14}B$ compounds. In the late 1970s, a global Co metal crisis occurred and triggered a search for a Fe-based intermetallic compounds. During 1983 and 1984, Hadjipanayis et al. [19] investigated a variety of melt spun R-Fe-metalloid systems and reported a $(BH)_{\max}$ of 103 kJ/m^3 (13 MGOe) in heat treated $Pr_{0.16}Fe_{0.76}Si_{0.03}B_{0.05}$ ribbons. At the same time Croat et al. [20, 21] reported 111 kJ/m^3 (14 MGOe) in $Nd_{0.135}(Fe_{0.945}B_{0.055})_{0.865}$ ribbons. In 1984, Sagawa et al. [22] using powder metallurgy developed a magnet based on the $Nd_{0.15}Fe_{0.77}B_{0.08}$ obtainig a $(BH)_{\max}$ of 286 kJ/m^3 (36 MGOe). This new magnet presented superior magnetic properties and low cost compared with the Sm-Co magnets. The Nd-Fe-B magnets replaced Sm-Co magnets, with the exception of high-temperature applications. In the Nd-Fe-B compounds, the Fe contributes for most of the magnetization and Curie temperature (T_C), the Nd provides the magnetocrystalline anisotropy, which aligns the magnetization with the tetragonal c-axis, and the B is necessary to stabilize the tetragonal structure. Nd-Fe-B magnets with a $(BH)_{\max}$ up to 440 kJ/m^3 (55 MGOe) can be found on the market today.

1.2 Basics of Magnetism

The field created by a permanent magnet is proportional to the magnets magnetization ($\boldsymbol{M}$), which is determined by the magnetization M of the magnetic material. The M is the density of induced magnetic dipole moments defined as $M = \frac{1}{V}\sum_i m_i$, where V is the crystal volume per atom and m is the atomic moment, often measured in the units of Bohr magneton (μ_B), which is the magnitude of the elementary magnetic dipole moment of an orbiting electron with an orbital angular momentum of $h/2\pi$. Mainly, the m depends on the spin angular momenta ($\mathbf{S}$), which is related to the number of unpaired electrons of the atom or the crystalline material. There are two main series of magnetic elements. From transition metals Cr to Ni, the magnetic moment is due to electrons on the $3d$ shell. From rare-earth metals Ce to Yb, the magnetic moment is due to electrons on the $4f$ shell. Nevertheless, the orbital angular momentum (the magnetization induced by the orbital motion) ($\boldsymbol{L}$) is also important in some magnetic compounds.

Permanent magnets include ferromagnetic or ferrimagnetic materials. Fig. 1.2 shows a plot of magnetization vs. temperature of pure Ni, which is the typical behavior of a ferromagnet. These materials undergo a sharp transition in their magnetic properties at T_C, in this case

T_C = 358°C. Below T_C, magnetic dipoles are aligned causing spontaneous magnetism. Above T_C, random thermal motions lead dipoles out of alignment resulting in zero net magnetization.

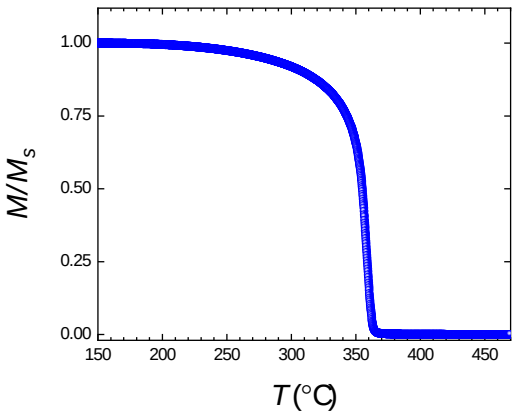

Figure 1.2: Typical plot of magnetization vs temperature of pure Nickel.

Ferromagnetic materials exhibit a substantial spontaneous magnetization at room temperature and are characterized by their hysteresis loop. The hysteresis loop, often referred to as the *M*-*H* loop (magnetization) or *B*-*H* loop (flux density) is a way to evaluate the magnetic response of a material, and can be visualized by considering a thermally demagnetized sample subjected to a magnetic field (H). A typical hysteresis loop of a ferromagnetic material is shown in Fig. 1.3. Under the influence of the magnetic field, the magnetization (M) (starting from point 0), increases along the dashed line. When the magnetic field is high enough (point a) all domains are aligned along the field and then the sample reaches the saturation magnetization (M_s). When the field is removed, the magnetization does not decrease in the same way, since the reorientation of the domains is not completely reversible, hence it reaches a residual or remanent magnetization (M_r). At this state some of the magnetic domains remain aligned but others are not (point b). The increase of a reverse field results in a continued decreased of the magnetization, and it is reduced to zero when the applied field has flipped enough domains so that the net magnetization is zero (point c). This field required to remove the residual magnetization is known as intrinsic coercive field (H_c) (and for *B*-*H* curve is known as flux coercivity ($_BH_c$)). This portion of this curve, between the remanence and the coercive field, is referred to as the demagnetization curve. Further increase in reverse field results in an increase of reverse magnetization until it reaches a negative saturation magnetization (point d). The rest of the

cycle is achieved by increasing the applied magnetic field again.

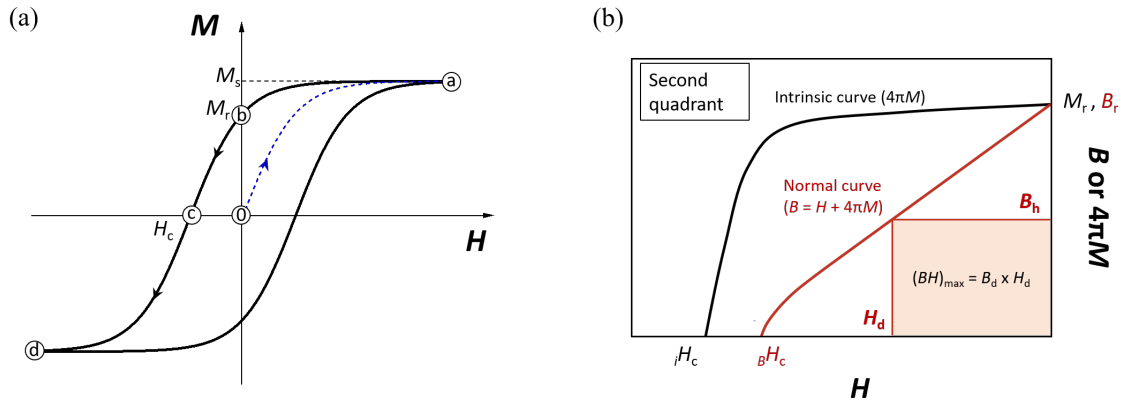

Figure 1.3: (a) The hysteresis loop (M vs H) and characteristic parameters (b) Determination of the energy product BH of a permanent magnet. The red rectangle corresponds to $(BH)_{\max}$.

In the SI system, both H and M are measured in A/m, albeit the quantities $\mu_0 H$ and $J{=}\mu_0 M$, both measured in T, are often used instead, here μ_0 is the permeability of free space ($\mu_0 = 4\pi \times 10^7$ H/m). In the cgs system, these units are Oe = 79.6 A/m (H), emu/cm^3 = kA/m (volume M) or emu/g = Am^2/kg (mass M).

An important value which quantifies the work done by a permanent magnet is the maximum energy product $(BH)_{\max}$. This parameter can be determined from the $B(H)$ from the demagnetization curve as shown in Fig. 1.3(b) and it corresponds to the magnitude of the maximum of the product BH as H is varied, and equivalent to the area of the largest rectangle that can be inscribed under the demagnetized curve (red rectangle). The units are given in kJ/m^3 (in SI units) or in MGOe (in cgs units) (kJ/m^3 = $4\pi/100$ MGOe $\approx$ 0.13 MGOe). The $(BH)_{\max}$ is the most convenient single figure of merit for a magnet. Since 1900, it has increased from 2 to 440 kJ/m^3 today, doubling roughly every 12 years. Theoretically, the $(BH)_{\max}$ is limited by the M_r according to Eq. (1.1), which cannot exceed the M_s, for randomly oriented non-interacting single domain particles $M_r = M_s/2$, or more generally for textured magnets, $M_r \leq M_s$.

$$(BH)_{\max} \leq \frac{1}{4}\mu_0 M_s^2. \tag{1.1}$$

1.3 Rare earth and transition metals coupling

The rare-earth (R) and transition metal (T) compounds are attractive for magnetic materials research as large number of R-T intermetallic compounds can be used as starting materials for permanent magnets of exceptional performance. The magnetic properties of R-T intermetallic compounds are attributed to their spin-spin exchange interactions and to crystalline electric field interactions. The magnetic properties of rare-earth and transition metal elements are due to the incomplete $4f$ and $3d$ electron shell, respectively [23].

In a R-T intermetallic compound, there are two sublattices, one formed from R atoms and the other from T atoms. The exchange interactions between R and T moments can be indirect R-R, indirect R-T, and direct T-T. A simple way to describe these interactions is by means of the Heisenberg Hamiltonian,

$$H = -\frac{1}{2}\sum_{\langle i,j\rangle} J_{ij}\mathbf{S}_i \bullet \mathbf{S}_j, \tag{1.2}$$

where J_{ij} is the exchange parameter of the interaction between the atomic spins S_i and S_j at ith and jth lattice sites. The summation is over the nearest-neighbors. For $J_{i,j} > 0$ the interaction is ferromagnetic and for $J_{i,j} < 0$ antiferromagnetic. The exhange interaction falls off rapidly with increasing distance between atoms i and j.

The strong T-T interaction is a result of $3d$ wave function overlap and is sensitive to crystal structure and cell volume. The interaction is usually ferromagnetic, but strongly depends on the ratio of the interatomic distance to the atomic size. In the case of iron, according to Néel, a distance of 2.86 Å (which is the typical Fe-Fe distance in iron alloys) for next nearest neighbors in the bcc phase lies within the appropriate range for ferromagnetic coupling.

The R-T exchange between the $4f$ and $3d$ electrons is indirect and likely mediated by the rare-earth $5d$ electrons. The $4f$-$5d$ interaction is ferromagnetic but the $5d$-$3d$ coupling is antiferromagnetic when the $5d$ band is less than half full and the $3d$ band is more than half full, as it is the case in alloys of rare-earths and ferromagnetic transition metals. The transition metal spin, S_{T}, then couples antiparallel to the rare-earth spin, S_{R}, if one assumes the rare-earth moment is derived only from $4f$ electrons. By Hunds rules, the magnetization of the transition metal and rare-earth are coupled parallel for the light rare-earths (less than half filled shell, $J = L - S$), and antiparallel for heavy rare-earths (more than half filled $4f$ shell, $J = L + S$) [24].

The interaction between the R ions can be explained through a RKKY interaction [25]. For this type of interaction, the conduction electrons s are polarized by $4f$ magnetic moment, mediating the R-R interactions. The interaction can be seen by considering a single localized magnetic moment surrounded by a gas of conduction electrons. The nature of the interaction is oscillatory, yielding positive and negative values for J_{RR}, depending on the distance between the R ions, and on the electronic band structure. The R-R separations are large enough in most R-T compounds that the $4f$ radial matrix elements, leading to negligible direct exchange between R spins [26]. The R-R separation in most R-T compounds is of the order 0.3 nm while the $4f$ radial matrix element is less than 0.1 nm. Thus, the R-R exchange can be considered weaker than the T-T, and R-T interactions.

1.4 Intrinsic and extrinsic properties

In magnetism, the magnetic properties of a material are classified into intrinsic and extrinsic properties. The former depend on the crystal structure and chemical composition of a magnetic phase and are independent of the sample form and microstructure. The latter depend on sample microstructure and crystallite orientation. High performance permanent magnets are formed from intermetallic compounds of R and $3d$ transition metals. The reason is natural, simultaneously one can benefit from the intrinsic properties, from the high magnetic moment per atom and the high magnetocrystalline anisotropy of the R metals.

Table 1.1: Intrinsic and extrinsic properties.

Properties	**Physical variable**
Intrinsic	Curie temperature T_{C} (K)
	atomic magnetic moment μ (μ_{B}/atom)
	spontaneus magnetization M_{s} (volume: A/m, mass: $\mathrm{Am^2/kg}$)
	magnetocrystalline anisotropy K ($\mathrm{J/m^3}$)
	anisotropy field H_{A} (A/m)
Extrinsic	remanence M_{r} (volume: A/m, mass: $\mathrm{Am^2/kg}$)
	coercivity H_{c} (A/m)

Both the intrinsic and extrinsic magnetic properties must be optimized in producing a practical magnet, but it is more convenient, dealing first with the intrinsic properties as they set limits on the extrinsic properties; $M_r < M_s$, $H_c < H_A$.

An ideal material to be considered as a potential permanent magnet should meet the following conditions:

1. A T_C higher than the maximum operating temperature, $T_C \geq 600$ K.
2. Large M_s. This implies that the material must be mainly (if not entirely) composed of magnetic atoms, the individual atomic moments should be large and they should couple parallel in a ferromagnetic structure.
3. Large H_A. The crystal structure must have an appropriate symmetry, for instance, tetragonal, hexagonal.
4. Little temperature dependence of the coercivity and remanance (which implies the same for M and H_A) in the working temperature range.
5. Possibility of obtaining a uniaxial grain-oriented microstructure, to maximize M_r.
6. Low cost of raw materials.

1.4.1 Magnetocrystalline anisotropy

Magnetocrystalline anisotropy is the tendency of the magnetization to align itself along a preferred crystallographic direction (easy axis) and the energy associated inhibits the switching of the magnetization from the easy axis to the hard axis. The magnetocrystalline anisotropy consists of a contribution of the T sublattice and a contribution of the R sublattice, however it is mainly dominated by contribution from the R sublattice. Phenomenologically, the uniaxial anisotropy energy E_A (also called MAE) of a tetragonal compound may be expressed as,

$$E_A = K_1 \sin^2\theta + K_2 \sin^4\theta + K_2' \sin^4\theta \cos 4\varphi + K_3 \sin^6 + K_3' \sin^6\theta \cos 4\varphi, \tag{1.3}$$

where K_1, K_2, K_2', K_3 and K_3' are the anisotropy constants, and θ and φ are the polar angles for the sublattice magnetization relative to the c- and a- crystallographic axes, respectively. In the

case of strong uniaxial anisotropy, it is appropriate to utilize only the first term of the expansion, $E = K_1 \sin^2\theta$, where K_1 is the first anisotropy constant. In this approximation, positive K_1 values imply that magnetization is be along the c-axis whereas negative values indicate in the ab-plane (the basal plane of the crystal). Many models of magnetization ignore higher order terms when dealing with uniaxial anisotropy. However, if $K_1 < 0$, the lowest energy term alone does not determine the direction of the easy axes in the ab-plane. For this, higher-order terms are needed, and these depend on the particular crystal system (hexagonal, tetragonal or rhombohedral) [27].

It is well known that the R sublattice anisotropy originates from the crystal field interactions due to the asymmetric charge cloud (non-spherical potential) of the $4f$ electrons (from the unpaired $4f$ electrons) and the electrostatic field of the charges surrounding the $4f$ electrons. For the tetragonal $RFe_{12-x}M_x$ (see section 1.6) compounds, the Hamiltonian for a R ion at the $2a$ site, can be given as

$$\mathcal{H}_{\mathrm{CF}} = B_2^0 O_2^0 + B_4^0 O_4^0 + B_4^4 O_4^4 + B_6^0 O_6^0 + B_6^4 O_6^4, \tag{1.4}$$

where O_n^m are the Stevens operators, which are functions of the angular momentum operators and are known for a magnetic ion with a given J value and B_n^m the crystal field parameters. The crystal field parameters are defined as

$$B_n^m = \theta_m \langle r^m \rangle A_n^m, \tag{1.5}$$

where θ_m are the Stevens factors α_J, β_J and γ_J for $m = 2$, 4, and 6, respectively. The $\langle r^m \rangle$ is the expected value of the $\mathrm{m^{th}}$ power of the radius of the R ion at the R site, and A_n^m are the crystal field coefficients which contain the interaction of the R charge density with the remaining crystal charge density. The coefficients B_n^m are determined by the environment of the R site, as well as by the ground state of the R^{3+} ion.

From the transformation properties of the Stevens operator equivalents (Eq. (1.5)) it is possible to derive relations between the anisotropy constants K_i and the crystal field parameters as,

$$K_1 = -\left[\frac{3}{2}\alpha_J \left\langle r^2 \right\rangle A_2^0 \left\langle O_2^0 \right\rangle + 5\beta_J \left\langle r^4 \right\rangle A_4^0 \left\langle O_4^0 \right\rangle\right] \tag{1.6}$$

and

$$K_2 = -\frac{35}{8}\beta_J \left\langle r^4 \right\rangle A_4^0 \left\langle O_4^0 \right\rangle . \tag{1.7}$$

A more detailed discussion of the effect of higher order terms on the magnetic properties of $RFe_{12-x}M_x$ compounds can be found in reference [28]. The thermal averages of the corresponding Stevens operators vary with a high power to the reduced rare-earth sublattice magnetization $m_r = M_r(T)/M_r(0)$. If the temperature is high enough, it is enough to consider only the lowest term of Eq. (1.6). From here, we can see the anisotropy field can be determined by the second order term of the crystal field, A_2^0. The magnetic anisotropy is parallel to the c-axis if $K_1 > 0$, so if $A_2^0 < 0$ then $\alpha_J > 0$, and if $A_2^0 > 0$ then $\alpha_J < 0$.

Table 1.2: Second order Stevens factor, $\alpha_J > 0$ for the trivalent rare-earth ions taken from [11].

Ce^{3+}	Pr^{3+}	Nd^{3+}	Sm^{3+}	Gd^{3+}	Tb^{3+}	Dy^{3+}	Ho^{3+}	Er^{3+}	Tm^{3+}	Yb^{3+}
-5.714	-2.101	-0.643	4.127		-1.010	-0.635	-0.222	0.254	1.010	3.175

Stevens factor of trivalent rare-earth ions are shown in Table 1.2. $\alpha_J > 0$ is only positive for the rare-earth atoms Sm, Er, Tm and Yb. In particular, α_J describe the shape of the charge distribution of the $4f$ electron distribution, the shapes are depicted for example in the book of Coey [11]. For $\alpha_J > 0$, the electron distribution is prolate i.e., elongated along the moment direction, for $\alpha_J < 0$, the electron distribution is oblate i.e., elongated perpendicular the moment direction.

Related with the magnetocrystalline energy is the anisotropy field H_A. The anisotropy field is the necessary field to rotate the magnetization from the easy to the hard axis. The orientation of the magnetization is determined by the condition $dE/d\theta = 0$, and for $\theta = \pi/2$ the anisotropy field is

$$H_A = \frac{2K_1 + 4K_2 + 6K_3}{\mu_0 M_s} \tag{1.8}$$

and considering only the first order constant K_1,

$$H_A = \frac{2K_1}{\mu_0 M_s}. \tag{1.9}$$

For an uniaxial magnet, when both K_1 and K_2 are taken into account; minimizing the anisotropy energy from Eq. (1.3), an easy cone phase appears when $K_1 < 0$ and $K_2 > K_1/2$. The cone angle is $\sin^{-1}\sqrt{|K_1|/2K_2}$. In practice, when $K_1 > 0$, the two anisotropy constants K_1 and K_2 can be determined by plotting the hard axis magnetization curve as H/M versus M^2. This is the Sucksmith-Thomson method, which is based on the equilibrium condition

$$\frac{H}{M} = \frac{2K_1}{M_s^2} + \left(\frac{4K_2}{M_s^4}\right) M^2. \tag{1.10}$$

Here K_1 can be obtained from the intersection of the straight line with the ordinate and K_2 from the slope.

1.4.2 Coercivity and magnetization reversal models

The coercivity in a permanent magnet can arise from different magnetization reversal mechanisms, (i) by cohererent rotation in single domain particles (ii) domain wall pinning and (iii) nucleation.

In the first case, if magnetic reversal of the material occurs only through coherent rotation of the magnetic moments from the easy axis to another against the magnetocrystalline anisotropy (Stoner-Wohlfarth reversal [29]), the upper limit of the H_c is determined by the H_A ($H_c \leq H_A$), that in the case of strong uniaxial anisotropy is given by Eq. (1.10). However in practice magnets barely reaches 20-30% of theoretical maximun. This is due to a number of factors, but mainly to the formation of reverse domains that arise from crystal imperfections including defects such as dislocations, interstitials, solute atoms and vacancies. Thus, the coercivity observed in a particular material is limited by the intrinsic properties but strongly dependent on processing.

Magnetic particles are composed of magnetic domains separated by domain walls or Bloch walls. Domains and domain walls are created in order to decrease the magnetostatic energy of a uniformly magnetized sample. When magnetic domains are subjected to a magnetic field in a opposite direction of their easy axis of magnetization, there is a gradual reorientation of individual moments in the domain wall leading that magnetization in adjacent domains points in opposite directions. The domain wall thickness ($\delta = \sqrt{A/K}$, with A being the exchange stiffness constant typically, $A \approx 10^{-6}$erg/cm) depends on the anisotropy of the material and the exchange interaction between the magnetic moments, on average spans across around 100-150 atoms.

The Bloch walls and the corresponding reversed domains are generated around all types of defects where the local values of the exchange field and anisotropy field deviate sufficiently from the values in the remaining material to make a local magnetization reversal possible. Such nucleation of the Bloch walls at defects may take place spontaneously or under the influence of a reversed magnetic field. The field necessary to create a region of reverse polarization, commonly referred to as the nucleation field (H_{N}), is often used to describe the ${}_iH_{\mathrm{c}}$ value. A first empirical approximation of the intrinsic coercivity is derived from the Brown-Aharoni model, and is given by Kronmüller [30] as

$$H_{\mathrm{c}} = \alpha H_{\mathrm{A}} - N_{\mathrm{eff}} M_{\mathrm{s}}, \tag{1.11}$$

where α and $\mathrm{N_{eff}}$ are microstructural parameters, the former describing the reduction of the crystal field by defects and by misaligned grains and the latter is the effective demagnetization factor due to the macroscopic sample or the microscopic grains. Both parameters can be estimated by analyzing temperature dependence of ${}_iH_{\mathrm{c}}$, H_{A}, and M_{s} assuming that the microstructure of the material does not change with temperature.

The coercivity in a permanent magnet is based either on the nucleation, pinning mechanism or a mixture of the above mentioned reversal mechanisms. Which mechanism is predominating depends on the magnetic properties and microstructure. An example of the microstucture dependece is the grain size (D) dependence of coercivity of sintered magnets shown in Fig. 1.4. The solid line corresponds to the theoretical calculation and the dashed line describes qualitatively the effect of the microstructure on H_{c}. According to this behavior, the coercivity of sintered magnets increases with the reduction of grain size going through a maximum at the single domain size and then decreases for ultra small particles due to thermal effects.

In region I, the magnetization reversal occurs at very small grain sizes $D \approx 2-5$ nm by thermal effects. These grains correspond to superparamagnetic particles. In region II, reversal occurs at grain sizes up to 10 nm by a homogenous rotation process. In region III the process occurs by inhomogenous rotation (curling process) and coercivity decreases with increasing grain sizes. In region IV, the magnetization reversal is via domain wall displacements in multidomain grains. In the single domain range (region I, II and III) the crystal imperfections reduce the

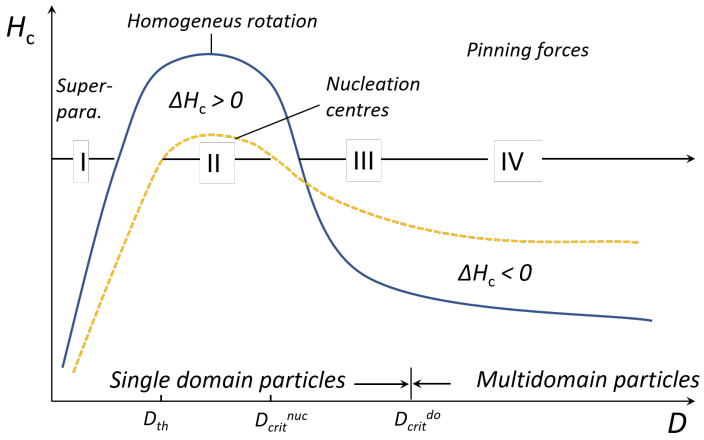

Figure 1.4: Representation of coercivity as a function of the grain size D taken from [7]. Solid line represent perfect particle and dashed line the imperfect particle.

coercivity whereas in the multidomain regime imperfections increase coercivity due to pinning of domain walls.

For strongly anisotropic materials with reasonably high magnetization, the single domain particle size is a fraction of a micron ($D_c \approx 0.3$ µm for $Nd_2Fe_{14}B$ [31], and $D_c = 0.7 - 2.2$ µm for $SmCo_5$ [32, 33]) and therefore, when materials are made with microstructure of this size, their coercivity is enhanced.

1.4.3 Other thermal properties

Besides the basic properties of permanent magnets, T_C, M_s, H_A, M_r, ${}_iH_c$ and $(BH)_{max}$, it is also important to quantify the changes in magnetic properties with temperature. Two coefficients commonly used for this purpose are the reversible temperature coefficients α and β. The α is the reversible temperature coefficient of remanence, and β of coercivity. Both parameters are a measure for the average change in M_r (or H_c) as a function of temperature, and they are expressed as $\%K^{-1}$ (or $\%°C^{-1}$).

If the variation of M_r (or H_c) is linear in a temperature range from T_1 to T_2, α and β are defined as,

$$\alpha \equiv \frac{M_{r(T_2)} - M_{r(T_1)}}{M_{r(T_1)}} \frac{1}{\Delta T} \times 100\% \tag{1.12}$$

and

$$\beta \equiv \frac{\mu_0 H_{c(T_2)} - \mu_0 H_{c(T_1)}}{\mu_0 H_{c(T_1)}} \frac{1}{\Delta T} \times 100\% \tag{1.13}$$

For non-linear variations one can calculate these coefficients with more accuracy using the expressions that can be found in the Appendix B.

1.5 Manufacturing of permanent magnets

There are several methods to produce permanent magnets, but the most common involves **powder metallurgy**. In this process, the potential magnetic alloy is pulverized into fine particles, compacted and heated to improve the densification. These type of magnets are called sintered magnets. Alnicos, ferrites, and anisotropic Nd-Fe-B and Sm-Co are made by this method. Another route of processing involves the **rapid solidification** of thin metallic ribbons that can be hardened either quenching directly from the melt or by annealing the overquenched ribbons. The ribbons are usually blended with a polymer to make a bonded magnet. Table 1.3 shows the performance of all types manufactured magnets.

Table 1.3: Performance of all types manufactured magnets taken from [12]. Values in brackets are in MGOe.

Magnet	$(BH)_{max}$ (kJ/m^3)	T_C (°C)	Max. working T (°C)	Oxidation and corrosion resistance	Machining property	Price
Sintered AlNiCo	10-103 [1.2-13]	890	600	good	outstanding	medium
Hard ferrite	6-41 [0.8-5.2]	450	300	good	normal	cheap
Sintered $SmCo_5$	119-191 [15-24]	740	250	good	normal	expensive
Sintered Sm_2Co_{17}	175-255 [22-32]	926	550	good	normal	expensive
Sintered NdFeB	239-414 [30-52]	310	230	poor	normal	medium
Bonded NdFeB	24-103 [3-13]	350	160	good	good	medium

In **sintered magnets**, the rare earth magnet alloy is first strip cast to produce large-grained material with a relatively fine-scale solidification microstructure. Hydrogen decripitation (HD) and milling are used to get the desired particle size, at which each particle is a single crystal grain. The particles are compacted at high pressure in an aligning magnetic field and then vacuum sintered to fuse into a solid block. The aligning magnetic field for die pressed magnets can be either parallel or perpendicular to the pressing direction. Also the pressure can be applied in all directions (isostatically pressed magnets). After sintering, the magnet shape is rough so it is machined to achieve close tolerances.

In rapid solidification techniques, metallic ribbons of ≈ 30-40 microns of thickness are obtained directly from the molten alloy by rapid quenching. The ribbons are magnetically isotropic powder particles of very small grains, about 30-50 nm in diameter. In the case of Nd-Fe-B, the nanocrystalline isotropic flakes may exhibt $(BH)_{\max}$ values of 10 to 16 MGOe. To transform these flakes into a **bonded magnet**, the powder particles can be blended with a polymer binder and then molded by injection or compression. However in this process the $(BH)_{\max}$ is reduced by approximately a 50% of the fully oriented (anisotropic)material. Rapidly quenched Nd-Fe-B powder freezes in random domain orientation resulting in an isotropic material structure which does not benefit from aligning and the finished magnet can be magnetized in any combination of poles and in any direction relative to the magnet. In order to increase the $(BH)_{\max}$ is necessary to use more expensive techniques involving hydrogenation, disproportionation, desorption, recombination process (HDDR), which uses Hydrogen at high temperatures to decompose the Nd-Fe-B material, and reconstitute it in anisotropic form. To fully densify the magnets, vacuum hot pressing and die upsetting are also needed.

1.6 Literature review: compounds with $ThMn_{12}$-type crystal structure

After the discovery of $R_2Fe_{14}B$ compounds with excellent magnetic properties, research and development in the field of permanent magnets has been focused almost exclusively on these alloys. However, in the last decade, because of the exponentially increasing demand for these magnets, increasing cost and supply risks involving the R-metals, there has been a renewed interest in the study of $RT_{12-x}M_x$ compounds with $ThMn_{12}$-type structure (lso known as 1:12), where T is a $3d$ transition metal (T = Fe, Co, Ni, Mn) and M is a stabilizing element (M = V,

Ti, Mo,Cr, W, Al, or Si) [34, 35, 36]. The M is essential as the 1:12 structure is not stable in bulk.

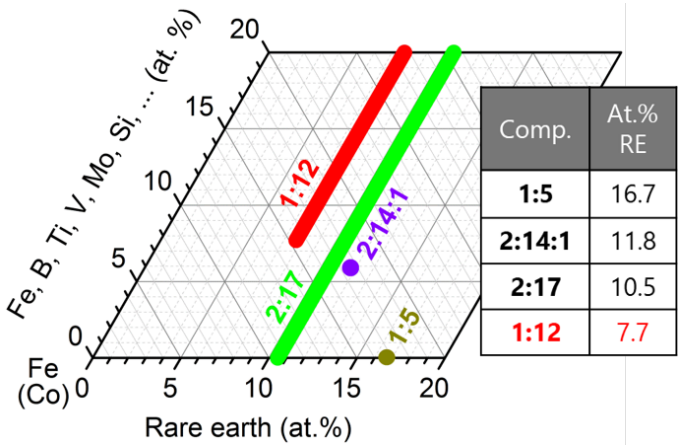

Figure 1.5: Rare-earth atomic percentage in different magnetically hard compounds: $SmCo_5$ (1:5), $Nd_2Fe_{14}B$ (2:14:1), Sm_2Co_{17} (2:17) and $ThMn_{12}$-type (1:12) (taken from [8]).

The 1:12 compounds contain only a 7.7% of R and they have a tetragonal structure, which is a requirement for uniaxial magnetocrystalline anisotropy. The nature of the MAE and the corresponding easy moment direction in the various $RFe_{12-x}M_x$ compounds is governed by the competition of the Fe and R sublattices, as was comented in section 1.4.1. The corresponding K_1 value have about the same magnitude as in $R_2Fe_{14}B$ compounds. However, the crystal field induced of the former differs both in sign and magnitude from that $R_2Fe_{14}B$ compound. This has as a consequence in the lowest order term of the R sublattice anisotropy (Eq. (1.6)), leading to an easy magnetization direction parallel to the c-axis only in those $RFe_{12-x}M_x$ compounds in which the second order Stevens factor α_j is positive (Sm, Er, Tm). Because the Er and Tm sublattice couple antiparallel to the Fe sublattice, the Sm-compounds are potential candidates to develop permanent magnets.

In addition to the magnetic potential, the Sm is comparatively cheaper than other rare-earth elements such as Nd, Pr or Dy, and there is plentiful supply (see Fig. 1.6).

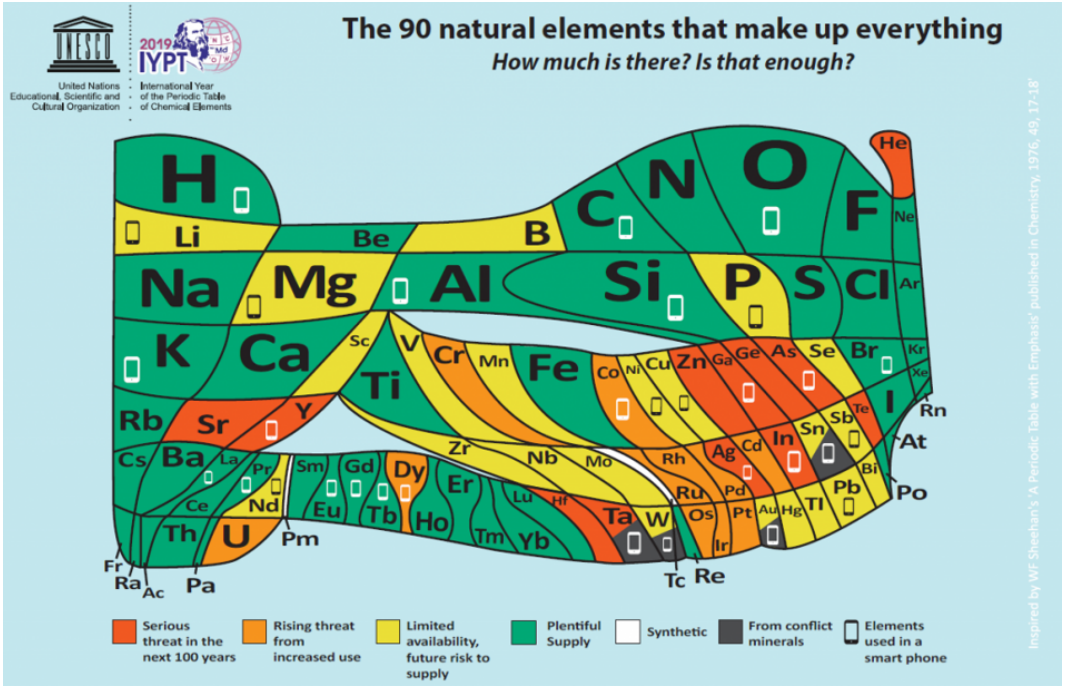

Figure 1.6: Periodic table relative to the abundance or scarcity of 90 naturally occurring elements on Earth. The size of the boxes shows the relative abundance of each element. Credit: European Chemical Society [9].

Table 1.4: Price (USD/kg) of rare-earth metals and oxides as of July 2019 according to [13].

	Pr	Nd	Dy	Y	Ce	La	Sm
Metal	114	74	349	34	6	6	15
Oxide	59	55	296	3	2	2	2

The $ThMn_{12}$ structure, shown in Fig. 1.7, is a body-centered tetragonal structure (space group $I4/mmm$) with a unit cell of 26 atoms. The R atom, usually the largest, occupies the single $2a$ thorium site, while the M and T elements are distributed over the three inequivalent crystallographic manganese sites, $8f$, $8i$, and $8j$. The atomic positions in the unit cell are for $2a$:(0,0,0), for $8f$: (1/4, 1/4, 1/4), for $8i$: (x_i, 0, 0) and for $8j$: (x_j, 1/2, 0). The values for x_i and x_j are, as for the $ThMn_{12}$ [37], close 0.36 and 0.28 [38, 39] respectively.

For the different stabilizing elements in $RFe_{12-x}M_x$, there are different stabilization ranges. The x-values are generally small, between 1 and 2, and in a few cases up to ≈ 3.5. The occupation criteria for the stabilizing metal depend on metallic radii and enthalpy values concerning the

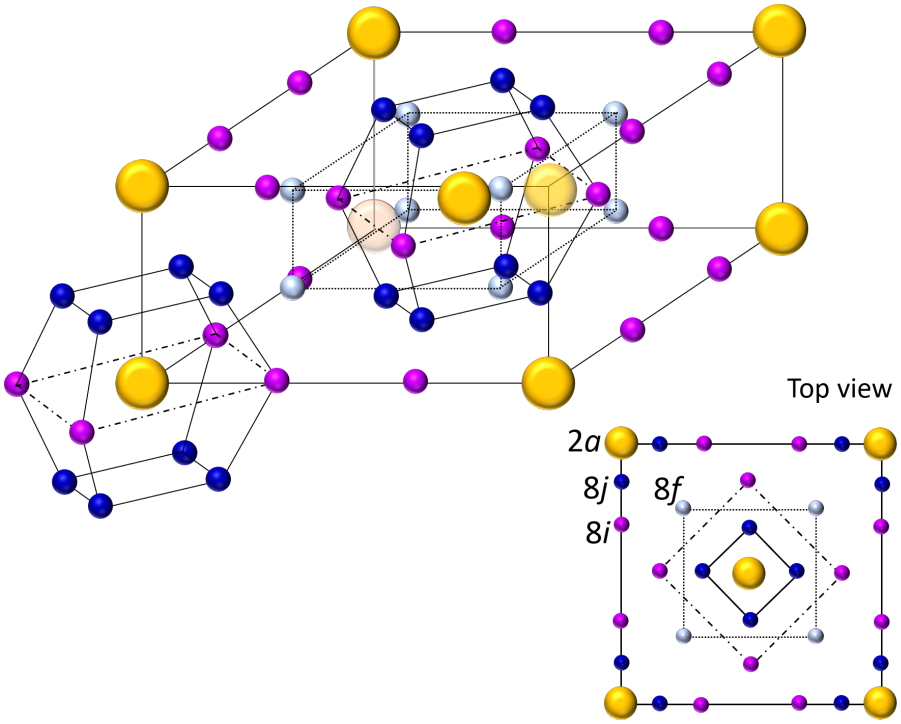

Figure 1.7: $ThMn_{12}$ crystal structure. Large spheres represent the position $2a$. The three different Wyckoff positions $8i$, $8j$, and $8f$ are represented by medium spheres

R-M bond [40, 41, 28]. In most of the cases, the M component shows a preference for the $8i$ site when M equals another transition metal (Ti, V, Mo) [42, 34, 43]. The situation changes, however, when M represents an s, p element (Al, Si), in these cases the M atoms occupy preferentially the $8f$ and $8j$ sites. Most of these results have been confirmed by neutron diffraction studies [44, 45, 46, 47] with the exception of Sm-based compounds due to its extremely high absorption cross-section, in this case Mössbauer spectroscopy have shown to be very powerful to analyze the M occupancies [48, 49, 14].

Several $RFe_{12-x}M_x$ compounds have been studied by various authors and the most explored among them are the Sm-Fe-Ti based. The $SmFe_{11}Ti$ was first reported by Ohashi et al. [50, 51]; in his work, the new phase had been proved to be titanium-stabilized SmT_{12} (T = Fe, Co, and Fe+Co) which was isomorphous to the $ThMn_{12}$ structure. Nikitin et al. [52] reported the $Sm(Fe,Co)_{11}Ti$ composition exhibiting best intrinsic properties of high M_s of 130 Am^2/kg, high H_A of around 8 MA/m (100 kOe), and a T_C of 600 K (327°C). Similar RET_{12} compounds were reported by De Mooij and Buschow [53, 54], with RE = Gd or Y and with V, Ti, Si, Cr, Mo,

and W as stabilizers. Singleton et al. [55] reported the magnetic and structural properties of melt-spun ribbons of $RFe_{11}Ti$ (R = Nd, Sm, Dy, Gd), where 1:12 crystallization was achieved with short annealing times (1-15min). The H_c was found to be strongly dependent on the microstructure. A H_c of 159 kA/m (2 kOe) was obtained in the samples with a grain size about 50 nm, and the annealed samples showed the presence of α-Fe. Pinkerton et al. [56] employed melt-spinning in $NdFe_{11}$(Mo,Ti) alloys. They found that 1:12 structure was obtained only in ribbons quenched at low speed (≤ 17.5 m/s). At higher speeds, the ribbons quenched instead into the disordered $TbCu_7$-type crystal structure. Several authors have observed the presence of α-Fe in annealed ribbons based on Sm. Most of the authors have attributed these phenomena to the evaporation of Sm from the melt-spun ribbons during annealing, because of the high vapor pressure of Sm. Okada et al. [57] demonstrated the importance of Sm atmosphere during the annealing to minimize the Sm evaporation from ribbons. The intrinsic magnetic properties of the most studied $RFe_{12-x}M_x$ compounds are given in Table 1.5.

Some works had been focused on reducing the content of the nonmagnetic element M in $RFe_{12-x}M_x$ compounds, with the aim to obtain higher values of M_s and T_C. For example, Kou et al. [58] studied $SmFe_{12-x}Mo_x$ compounds with a wide range of Mo content, and they stabilized the 1:12 phase for Mo content as low concentrations as x = 0.5, although α-Fe was detected as well. The H_A for x = 0.5 was of 8 MA/m (100 kOe) and T_C of 544 K (271°C).

Table 1.5: Intrinsic properties of some $RFe_{12-x}M_x$ compounds. Easy magnetization direction (EMD), anisotropy field, H_A, saturation magnetization, M_s, and Curie temperature T_C.

Material	EMD	$\mu_0 H_A$ (T)	M_s (Am^2/kg)	T_C (K)	Refs.
$SmFe_{11}Ti$	*c*-axis	10.5	122	600	[59, 60, 61, 52]
$SmFe_{10}V_2$	*c*-axis	10.5	86	605	[46]
$SmFe_{10}Mo_2$	*c*-axis	3.7	65	483	[42]
$SmFe_{10}Cr_2$	*c*-axis	5.9	84	575	[42]
$SmFe_{10}Si_2$	*c*-axis	5.2	112	590	[42]
$NdFe_{11}Ti$	*c*-axis	2.4	133	570	[59, 60]
$YFe_{11}Ti$		2.0	120	538	[62, 60, 63]
$GdFe_{11}Ti$		3.6	81	610	[62, 60]
$TbFe_{11}Ti$	Planar		74	580	[60]
$DyFe_{11}Ti$		2.8	75	560	[62, 60]
$HoFe_{11}Ti$		2.8	82	540	[62, 60]
$ErFe_{11}Ti$		2.6	84	530	[60]
$CeFe_{11}Ti$	*c*-axis	1.5	108	485	[64]
$CeFe_{10}V_2$	*c*-axis	1.0	76	425	[64]
$CeFe_{10.5}Mo_{1.5}$	*c*-axis	1.0	76	386	[64]
$YFe_{10}V_2$	*c*-axis	2.7	106	537	[44, 46]
$NdFe_{10}V_2$	*c*-axis	1.8	112	583	[46]
$GdFe_{10}V_2$	*c*-axis		61	610	[46]
$DyFe_{10}V_2$	*c*-axis	7.0	58	532	[46]
$ErFe_{10}V_2$	*c*-axis	3.3	86	507	[46]
$PrFe_{10.5}V_{1.5}$			121	625	[65]
$NdFe_{10}Mo_2$	Planar	0.1	75	410	[66, 67, 68]

Recently, there is an increasing interest on the studies of the stability of the $RE(Fe,T)_{12}$ structure by replacing the R element by cheaper one, such as Ce [69, 70, 71] or Zr [72, 73, 74, 75]. The effect of Zr on the stability of 1:12 phases was reported by Sakurada et al. [76] in $RFe_{12}Si_2$ and very recently by Gabay and Hadjipanayis in $Zr_{1-x}Ce_xFe_{10}Si_2$ [75]. They found a pure or nearly pure $ThMn_{12}$ structure for $0 \leq x \leq 0.6$. A more extended study was done by the same author [73] in $Zr_{1-x}R_xFe_{10}Si_2$ alloys with R = Y, La, Ce, Pr, and Sm and they found that the effect of Sm was by far the strongest with a H_A value of 3.2 MA/m (40.7 kOe). They realized that compared with the R-free parent compound, Y, Ce, and Sm reinforced the magnetocrystalline

anisotropy whereas Pr weakened it. The effect of Sm was also demonstrated in melt-spun ribbons. In other work, Goll et al. [69] studied the $CeFe_{11-x}Co_xTi$ alloy and obtained best intrinsic magnetic properties of $\mu_0 M_s = 1.27$ T and $K_1 = 2.15$ MJ/m^3 for 15 at% of Co content. Afterward, Gabay et al. [70] studied $Ce_{1-x}Sm_xFe_9Co_2Ti$ alloys prepared by melt-spinning and mechanochemical syntesis. Values of H_c up to 64 kA/m (0.8 kOe) and 167 kA/m (2.1 kOe) were obtained. Submicron partially anisotropic particles collected after the mechanochemical syntesis for $x = 0.5$ and $x = 1$ exhibited H_c of 143 kA/m (1.8 kOe) and 462 kA/m (5.8 kOe) and $(BH)_{max}$ of 43.2 kJ/m^3 (5.4 MGOe) and 79.2 kJ/m^3 (9.9 MGOe), respectively.

Another area of research has been focused on the nitrogenation of the $RFe_{12-x}M_x$ compounds. Yang et al. [60] showed that nitrides of the type $RTiFe_{11}N_x$ had a significant improvement of magnetic properties. The nitrogen atoms not only had an effect of increasing both the Curie temperature and iron moment, but also might change the magnetocrystalline anisotropy. Although these compounds present intrinsic properties very promising, it is rather difficult to convert them into magnets.

Despite the nonexistence of binary $SmFe_{12}$ in bulk, the formation of this phase was successful synthetized in thin films by Refs. [77, 78]. More recently, Hirayama et al. [79] prepared $NdFe_{12}N_x$ film with $\mu_0 M_s$ of 1.6 T (16 kG), H_A of 6.4 MA/m (80 kOe), and T_C of 550 K (277°C), but the H_c barely reached 80 kA/m (1 kOe). Sato et al. [80] prepared the same film but thinner and they obtained a H_c of 342 kA/m (4.3 kOe). Hirayama et al. [79] also prepared the $Sm(Fe_{1-x}Co_x)_{12}$ compound in thin films and found excellent intrinsic hard magnetic properties with $\mu_0 M_s$ of 1.78 T, H_A of 9.6 MA/m (120 kOe) and Curie temperature of 859 K (586°C), all of which are superior to those for $Nd_2Fe_{14}B$. Despite, the binary 1:12 films have promising values to fabricate PMs it is still necessary to produce 1:12 compounds in bulk by conventional methods, such as melt spinning and mechanical alloying, to be suitable for industrial applications.

1.7 Objectives and scope

The aim of this thesis was to develop a Sm-based magnet with $ThMn_{12}$ structure with the magnetic properties required for permanent magnets applications and a lean use of critical raw materials.

This aim translates into two specific objectives:

1. The search of elements (M) that guarantee the stability of the tetragonal 1:12 structure, including the determination of the smallest amount of M needed in order to obtain the largest saturation magnetization, anisotropy field and Curie temperature.

2. Manufacturing of a 1:12 Sm-based magnet, which includes the study of the effect of microstructure on coercivity, as well as the study of the processing parameters to develop the bulk magnet.

In order to do this, several Sm-based compounds are studied over the course of this thesis, including bulk materials of Sm-Fe-V-M (M= Cu, La, Ti, Mo). This thesis is divided in 6 chapters. **Chapter 2** deals with the experimental procedures and the description of the techniques used throughout the study. **Chapters 3** presents the structural and the intrinsic magnetic properties of the systems studied. **Chapter 4** presents different approaches to obtain the hard magnetic properties, among them grain size reduction by mechanical milling, bulk hardening by intergrain boundary phases and mechanical milling/rapidly solidify ribbons: amorphization and recrystallization. Here is shown the importance of microstructure and processing. **Chapter 5** is devoted to the fabrication of the isotropic 1:12 Sm-based by hot-compaction, and the attempts to get an anisotropic magnet by using hot-deformation. Finally **Chapter 6** contains general conclusions and summarizes the work contained in the thesis.

Chapter 2

Experimetal Procedures

This chapter presents the experimental methods used for the preparation and characterization of Sm-based 1:12 magnets. The chapter is divided into two parts. The first part explains the synthesis and processing of the alloys. Melting of the intermetallic alloys by arc-melting and heat treatment procedures to obtain desired phases are explained. Processing routes like mechanical milling and melt-spinning are discussed in detail, as well as consolidation techniques such as hot-compaction and hot-deformation. The second part part describes the techniques used for investigating the crystal structure, microstructure, thermal and magnetic properties.

2.1 Methodology

This section outlines the processing routes employed to prepare the samples starting from melting alloys from pure metals, ribbons, powders to bulk magnets. Fig. 2.1 shows a flow diagram summarizing the different paths. For intrinsic property studies, alloys with stoichiometric 1:12 composition were prepared by arc melting (AM) followed by heat treatment (HT), the optimal annealing conditions, for obtaining the 1:12 phase, was determined by trying different combinations of heat treatment temperatures and time. After the heat treatment the ingots were quenched in water, to avoid any possible phase transition during the cooling process.

Some of the alloys with best intrinsic properties were selected to develop coercivity, either in ribbons or powder form. In the case of Sm-Fe-(Ti/V) alloys, highly disordered ribbons were produced by melt-spinning and subsequently heat treated to get a fine microstructure with nano

sized grains of 1:12 phase. For powder processing, Sm-Fe-V, Sm-Fe-(V,Mo), Sm-Fe-(V,Cu), Sm-Fe-(V,Ti) based alloys were produced by arc-melting, followed by a long homogenization. The heat-treated ingots were crushed and then high energy ball-milled (HEBM) to pulverize and decrease the particle size of the resultant powders. The powders were consolidated by hot compaction (HC) and hot deformation (HD). The Sm-losses were observed in every stage of the processing which involved high temperatures, therefore every stage was optimized in order to keep the initial composition.

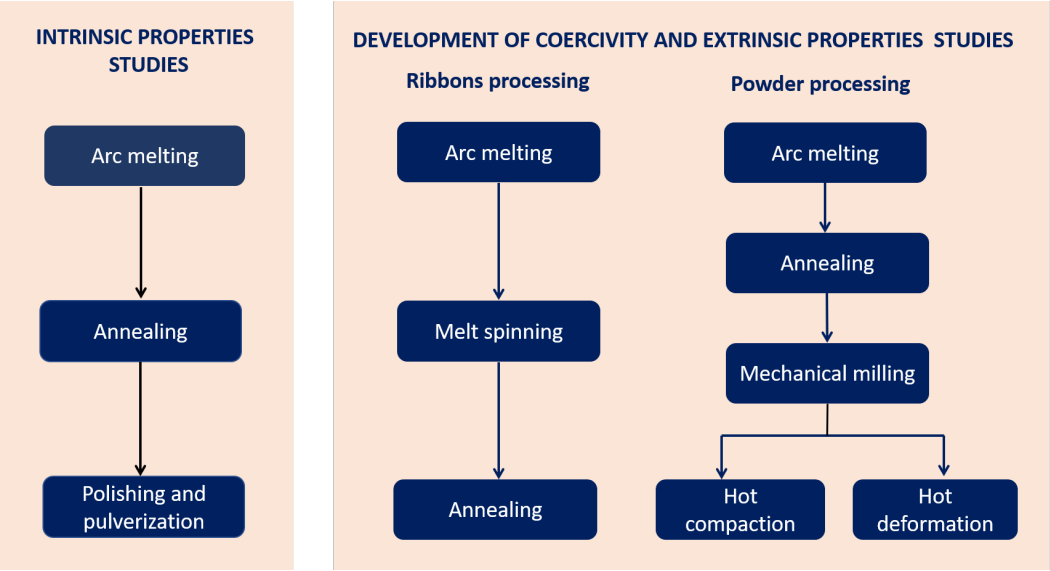

Figure 2.1: Different paths followed to prepare the samples

A list of all the samples prepared in this thesis are shown in Table 2.1. The upper part of the table shows different stoichiometric Sm-based alloys prepared to study the intrinsic properties and the development of coercivity. The lower part, shows exclusively off-stoichiometric alloys, prepared to study the development of coercivity, to produce isotropic and anisotropic bulk magnets.

Table 2.1: Samples prepared in this thesis. AM = Arc melting, MS = Melt spinning, HT = Heat treatment, HEBM = High energy ball milling, HC = Hot compaction, HD = Hot deformation.

Sample	**Synthesis**	**Processing**	**Study**
$SmFe_{12-x}V_x$ (x=0.5, 1, 1.5, 2)	AM	HT	Intrinsic properties
$Sm_{1-x}Zr_xFe_{11}V$ (Zr=0, 0.2, 0.4)	AM	HT	Intrinsic properties
$Ce_xSm_{1-x}Fe_9Co_2Ti$ (x=0, 0.25, 0.5, 0.75, 1)	AM + MS	HT	Mössbauer spectroscopy
$SmFe_{10}V_2$	AM	HT + LEBM	Development of coercivity
$(Sm_{10}La_2Fe_{75}V_{13})_{98}La_2$	AM	HT	Development of coercivity
$Sm_{10}Fe_{73}V_{15}$	AM	HT + HEBM + HT	Development of Coercivity
$Sm_{10}Fe_{73}V_{15}$	AM	HT + HEBM + HC + HT	Isotropic magnet
$Sm_{10}Fe_{73}V_{15}$	AM	HT + HEBM + HD	Texture
$Sm_{10}Fe_{73}V_{15}$	AM	HT + HEBM + HC-field assisted	Texture
$Sm_{10}Fe_{73}V_{7.5}M_{7.5}$ (M=Ti, Mo)	AM	HT + HEBM + HC + HD	Texture
$Sm_{10}Fe_{73}V_{13}Cu_2$	AM	HT + HEBM + HC + HD	Texture
$Sm_{10}Fe_{76.5}V_{11.5}$	AM	HT + HEBM + HC + HD	Texture

2.2 Synthesis

2.2.1 Arc melting

Arc melting is a metallurgical technique used for melting and alloying. This process consists of melting the pure elements of the alloy with a certain stoichiometry. Melting is achieved by discharging an electric arc between a sharp tungsten electrode (cathode) and the elements placed in a water-cooled copper crucible (anode). The low temperature (coming from the water flow) of the crucible and tip prevents any reaction and contamination of the alloy, in spite of the very high temperatures reached by the arc discharge. Controlling the current, electrode distance and chamber pressure ensure the production of a well-homogenized alloy.

To produce the arc, a high voltage in a proper atmosphere is needed. Before melting, the arc melter chamber was evacuated and purged with Ar at least two times. After the last purge, the vacuum pump was switched off and the chamber pressure was kept at 500 mbar (50 kPa) above the atmospheric pressure, with the Ar inlet and exhaust simultaneously open. This equilibrium guaranteed a continuous flow of the residual gases. The alloy piece was flipped and remelted typically four times to ensure homogeneity. The alloys were prepared from 99.9% pure elements to form ingots of desired compositions with a mass of 3 to 7 grams. The mass loss after the melting was kept under 0.5% of the desired sample mass. Sm-losses were compensated by extra Sm addition. To avoid the spattering of the elements (due to the power of the arc) and to minimize the Sm-losses, the Sm and lightest pieces were placed at the bottom, and heavier pieces, covering the previous ones at the top.

2.2.2 Melt spinning

Melt spinning is a technique used for rapid solidification of molten metals. The alloy usually solidifies in the same structure of a liquid, forming a metallic glass, or in a highly disordered crystalline state. Usually glass transition temperature and crystallization or recrystallization temperatures may be identified for the quenched alloys. For the crystalline materials, melt spinning may eliminate the formation of unfavorable phases and/or produce metastable ones which cannot be obtained by other means. Its use in permanent magnets technology represents a different technique from conventional ones as powder metallurgy.

A typical procedure for melt spinning is explained in Fig. 2.2. Solid pieces are melted by an induction coil (i) in a crucible and pushed out of the crucible by gas pressure (P). A jet of molten alloy (A) is then ejected on a water-cooled copper wheel, which is rotating at a high speed. The liquid solidifies at a cooling rate of up to 10^6°C/s and results in ribbons which are ejected off the wheel. The wheel speed, ejection conditions, and melt temperature are fundamental parameters that need to be properly chosen according to the nature of the alloy.

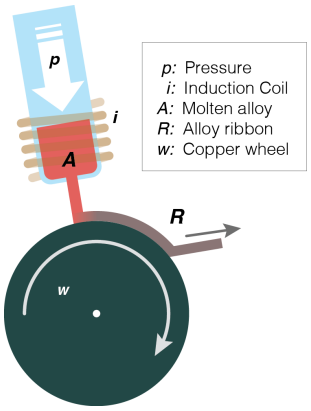

Figure 2.2: Diagram of melt-spinning process. The metal (A) is melted by the induction coil (i) and pushed by gas pressure (P), in a jet through a small orifice in the crucible over the spinning roller where is rapidly cooled to form amorphous or highly disordered ribbons.

In the production of hard magnetic materials, this technique is used to obtain ribbons with a fine uniform nanocrystalline grains. To crystallize the ribbons and to develop coercivity, it is necessary to anneal the melt-spun ribbons or to adjust the quenching rate by changing the wheel speed. The ribbons are crushed into powders and afterward they can be shaped into isotropic polymer-bonded magnets or hot compacted into dense magnets.

2.2.3 Heat treatment

During the heat treatment process, the alloys are heated to a specific temperature for a certain time and then cooled down. Heat treatment temperatures, times and cooling rates are chosen depending on the objective, such as homogenization, phase stabilization or recrystallization.

In this work, as-cast alloys were generally heat treated at high temperatures $T \geq$ 800°C for a long time (12 to 24 h) in order to obtain the 1:12 phase. Melt-spun ribbons and milled

powders were heat treated at temperatures T< 800°C for short times (1 to 30 min) in order to recrystallize and to induce the growth of the 1:12 phase grains from amorphous precursors.

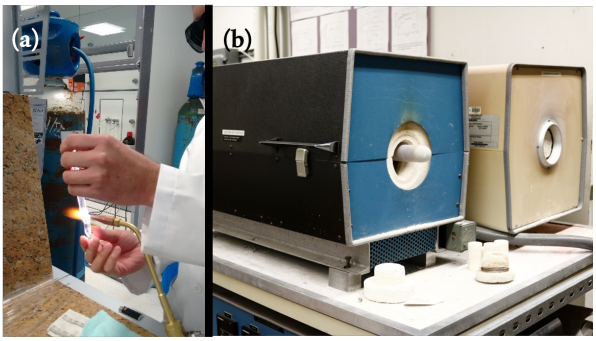

Figure 2.3: (a) Constriction of the quartz tube to make easier the sealing (b) High temperatures tube furnaces Lindberg/Blue M

Heat treatment was performed in quartz tubes sealed under Ar at 10 kPa (100 mbar) below the atmospheric pressure, after evacuating the tube to 10^{-4} mbar to avoid oxidation (see Fig. 2.3(a)). A Thermolyne 47900 furnace was used for heat treatments $T < 900$°C, and a Lindberg/Blue M STF54453C tube furnace for $T > 900$°C (see Fig. 2.3(b)). The furnace temperature on the display furnace was confirmed using a K-type thermocouple. Once heat treated, the samples were quickly cooled to room temperature by quenching in water. Quenching is often necessary in order to investigate compounds which are only stable in certain temperature ranges and decompose at lower temperatures. By quenching, the decomposition is usually negligible and the metastable phase is retained.

2.2.4 Mechanical milling

Mechanical milling is a processing technique where powder of pure elements or prealloyed compounds are mixed and undergo grinding, cutting, pressing, or crushing to produce finer particles with sizes in micrometer range. A ball mill is often used for mechanical milling. Here, the powders collides repeatedly with the balls. The kinetics of the ball milling depends on the energy transferred to the powders from the balls, this energy in turn depends on many factors such as the mill speed, ball to powders weight ratio, ball size distribution, milling media, milling temperature, and milling time. Depending on the conditions, not only the size of the coarse particles are reduced but different processes can occur during the milling. For example, mechanical alloying

(MA) can take place by mixing different components to produce new alloys. In this process, the particles are repeatedly flattened, cold welded, fractured and rewelded to produce a homogeneous material. Furthermore, with this method it is possible to synthesize non-equilibrium alloy phases such as metastable crystalline and quasicrystalline phases, amorphous, nanostructured and highly disordered alloys.

There are several types of ball mills, the planetary mill and the shaker mill are the most often used for laboratory purposes, while the horizontal ball mills are for industry. In this work, an SPEX 8000M Mixer/Mill was used.

In the SPEX high-energy mill (Fig. 2.4(a)), the vial partially filled with balls, is shaken in a complex motion that combines back-and-forth swings with short lateral movements, each end of the vial describing a figure-8. Because of the amplitude and velocity of the clamp's swing, each ball develops fairly high G-forces, enough to pulverize the sample. The Mill shakes the containers back and forth approximately 1080 cycles per minute (60 Hz).

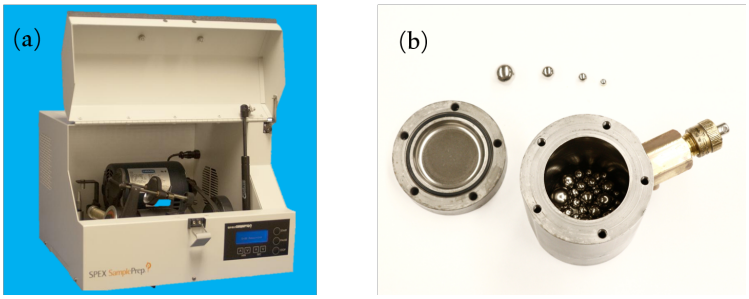

Figure 2.4: (a) SPEX 8000M mixer/mill (b) custom-made hardened steel vial and balls. The milling jar is equipped with a vacuum valve.

The prealloyed powders and several steel balls of 12, 8, 5.5 and 4 mm were placed together in a hardened steel vial (Fig. 2.4(b)) and in a suitable atmosphere; Ar (dry milling) or hexane (wet milling). For the dry milling, the jar was evacuated to $3{\times}10^{-5}$ mbar using a PFEIFFER VACUUM turbomolecular pump and back-filled with Ar. The powder was milled for the desired time and then, according with the milling atmosphere, the powder was washed and removed from the vial.

During the milling, the temperature rises because of continuous collisions of the balls. To minimize this effect, the milling was done for a predetermined time, paused until the vial cooled

down and then it was resumed. To minimize the powder contamination, hardened steel milling tools were used.

2.2.5 Consolidation Techniques

The production of powders with the required properties of microstructure and coercivity is only the first step in achieving a bulk magnet. The milled powders must be consolidated and sintered or heat treated to obtain a bulk piece. During heat treatment grain growth is inevitable but it should be restricted to an optimum amount.

Die compaction

Metallic powders are usually compacted by using two techniques, cold and hot pressing. Cold pressing is the most common technique used in shaping metallic powder. It consists of applying uniaxial pressure to the powders placed in a die between two rigid punches. The compacted piece must be strong enough to resist the ejection forces and handling prior sintering.

Hot pressing is one of the primary methods used to produce isotropic rare-earth permanent magnets. In this technique, the powders are compacted and sintered simultaneously in a single process, in which a combination of diffusion (induced by the sintering) and stress at high temperatures causes a time dependent plastic deformation below the yield strength of the metal [81]. Hot pressing achieves higher densities (> 92%) and better mechanical properties than that of cold pressing. The mold is usually made of graphite to facilitate the heating and the process is carried out in vacuum to avoid the contamination of the compact. As a consequence of the friction between the powders and die walls, a density gradient occurs inevitably in the compact, with the highest density next to the moving punch face and the lowest near the fixed punch.

The main steps during the hot pressing were: (1) loading the powder into the die cavity (2) chamber evacuation ($P \sim 10^{-4}$mbar) (3) heating the powder (4) compacting the powder by applying pressure and high temperature (5) pressure release and cooling down (6) removing the compacted from the die. The Fig. 2.5 shows the hot compacting setup.

In the hot pressing device, the powder was indirectly heated by an electrical resistance. A graphite mold was placed into a tungsten carbide (WC) die cavity, and filled with the powders. As the heating process was not direct, the heat transfer from the die cavity (acting like a

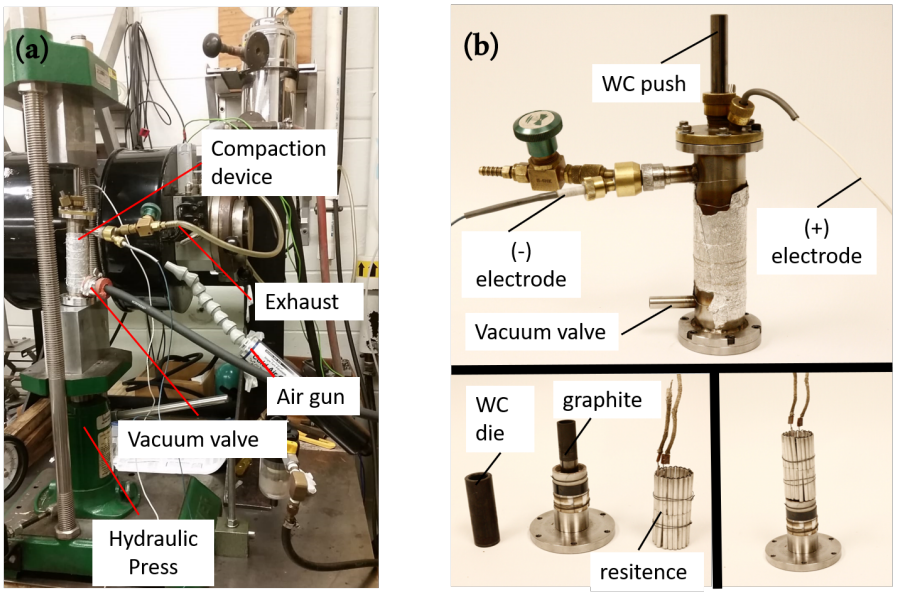

Figure 2.5: (a) Hot compaction set up (b) inside of the device (c) WC die and resistence heater.

furnace) to the mold surface and subsequently throughout the cross-section of the mold takes time (approx. 13 min). When the mold reached the desired temperature, the powders were uniaxially pressed and sintered between two WC punches. Molybdenum foils were used to prevent the compact from sticking to the WC punches.

After the compact piece was prepared, a very thin slice was cut using a a BUHLER ISOMET low speed diamond saw and was used for characterization. The remaining compact was collected to do the hot deformation.

Hot deformation

Hot deformation process is one of the main techniques to produce anisotropic R permanent magnets. In this technique, the hot compacted piece is heated up to plastic stage and a compressive force is applied. Thus, the height of the piece is decreased while allowing to expand freely in the cross section area.

In the case of Nd-Fe-B magnets this technique is used to induce grain alignment by plastic flow, and gives a strong crystallographic texture with the c-axes of the platelet like grains parallel to the compression direction [82].

The setup of the hot deformation is shown in Fig. 2.6. The main steps during the process were: (1) loading the compacted piece between two alumina punches (2) chamber evacuation ($P \sim 10^{-4}$ mbar) (3) heating and deformation of the compacted piece (4) pressure release and cooling down (5) removing the deformed piece from the press. As a consequence of the hot deformation process, internal cracks may appear, such situation can be minimized by optimizing the processing parameters.

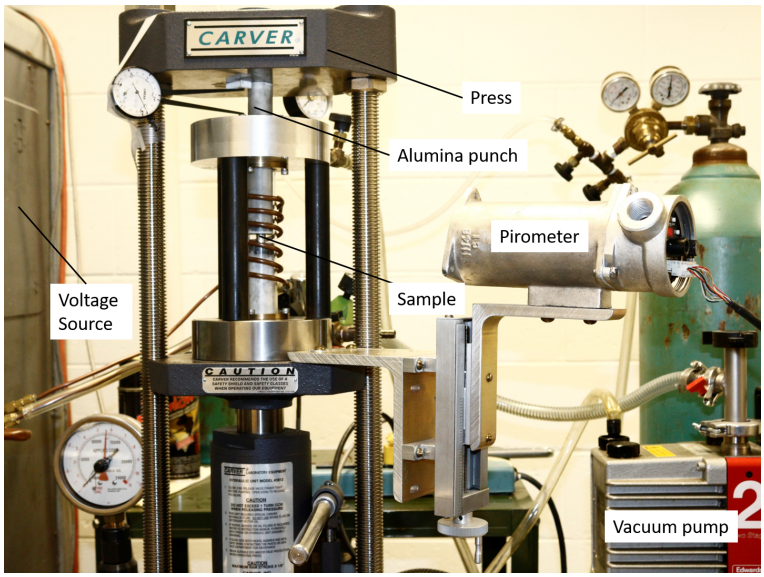

Figure 2.6: Hot deformation equipment

In this work, heating was produced by induction, therefore the heat transfer to the compacted piece was very fast. Depending on the material, the deformation was done in less than 5 minutes.

As the heating process was induction, the involved tools were thermal insulators. Mica sheets between the alumina punches and the compact were used to prevent the deformed sample from sticking to the punches. Before starting the deformation, it was important to ensure the alignment between the compacted and the two punches to prevent bending of the compact, the base and lid (as the compact was cylindrical) should be completely parallel. Once the sample was deformed the mica was removed from the top and bottom surfaces using a bench grinder and polished it by 800 grit sandpaper. Ethanol was used to rinse the surfaces.

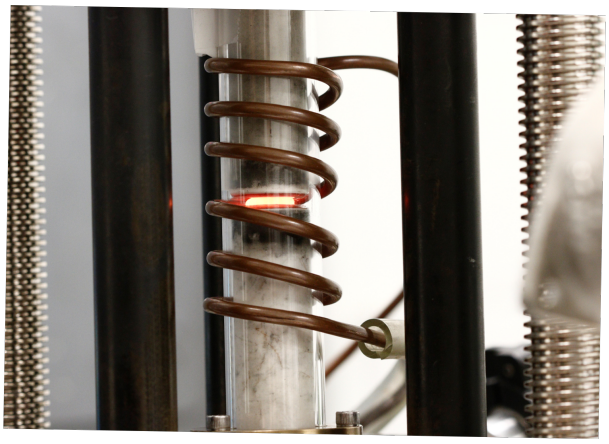

Figure 2.7: Hot deformed magnet

2.3 Characterization techniques

The alloys were characterized for structure, microstructure, magnetic and thermal properties by different techniques. Structural and morphological characterization was carried out by X-ray diffraction (XRD) and Scanning (SEM) and Transmission (TEM) Electron Microscopy, respectively. Thermal and magnetic properties were investigated by thermogravimetric (TGA) and differential thermal analysis (DTA), vibrating sample magnetometry (VSM) and Mössbauer spectroscopy.

2.3.1 X-ray diffraction (XRD)

Powder XRD is a powerful technique to determine the structure of crystalline solids. A typical diffractometer consists of a X-ray source, a sample holder and a X-ray detector which collects the diffracted X-rays.

XRD technique is based on constructive interference of monochromatic X-rays diffracted from a crystalline sample. The X-rays are generated by a cathode ray tube, filtered to produce monochromatic X-rays, collimated to narrow the beam, and directed toward the sample. A spherical wave is radiated when X-rays are diffracted by atoms from internal crystal planes of the sample. If there are different scattering centers, the spherical waves can interfere with each other either constructively or destructively. The diffraction of X-rays takes place only at those particular incident angles which satisfy Bragg's law

$$2d\ \sin\theta = n\lambda, \tag{2.1}$$

where λ is the wavelength of the X-rays, d is the inter planar distance, n is the diffraction order ($n > 0$) and θ is the incident angle of the X-ray. The diffracted X-rays are then detected, processed and counted. By scanning the sample through a range of 2θ angles, all the possible diffraction directions of the lattice should be gotten due to the random orientation of the powder material.

Powder samples, obtained from bulk samples and ribbons, were examined using two different diffractometers, a Philips X'pert PRO automatic at advanced research facilities (SGIker) of the University of Basque Country and a Rigaku Ultima IV at University of Delaware. The Philips X'pert PRO automatic is operated at 40 kV and 40 mA, in $\theta - \theta$ configuration, and Cu-K_α radiation (λ = 1.5418 Å). The Rigaku Ultima IV is also operated at 40 kV and 40 mA, with Cu-K_α radiation, but $\theta - 2\theta$ configuration.

From XRD patterns, the presence of one or more crystalline phases were observed. The identification of the phases was performed with standard diffraction patterns downloaded from ICSD database. The XRD patterns were refined using Maud software based on the Rietveld method. From the refinement, the volume fractions and lattice parameters of the phases present were obtained.

2.3.2 Electron microscopy

Electron microscopy is a technique that produces high magnification images by using electrons, which have wavelengths of the order of nanometers, as the source of radiation. Two kinds of microscopes SEM and TEM were used in this work.

Scanning electron microscope (SEM-EDX)

In SEM, electrons are generated by an electron gun situated at the top of the microscope, accelerated down and passed through a combination of condenser lenses and apertures to produce a focused beam of electrons which hits the surface of the sample. From the interaction of the electrons and the sample, elastic collisions lead to backscattering and electron diffraction. Inelastic collisions lead to the emission of secondary electrons, Auger electrons, or characteristic

X-rays. Secondary electrons are primarily used for imaging and they provide good topological contrast. Backscattered electrons are used for imaging as well but they are more sensitive to atomic number differences and give better phase contrast. The X-rays can be used for the compositional analysis by energy dispersive X-ray spectroscopy (EDX).

Two SEM were used in this work, a JEOL JSM-6335F model equipped with an IXRF Systems microanalyzer at University of Delaware, and a Hitachi TM3000 Table Top Scanning Electron Microscope at University of Basque country. The SEM is used in order to investigate the microstructural features of samples (bulk and ribbons) and the presence of different phases by using secondary electron (SEI) and backscattered electron (BSE) image modes.

Samples for SEM were prepared using different ways. Powder was sprinkled onto a double side adhesive carbon tape. Bulk samples were embedded in a epoxy (Spurr Low-Viscosity embedding Kit) and cured for 8 hours at 70°C. In order to obtain a shiny and smooth surface, the cured samples were successively polished with emery papers of grit sizes 120, 300, 600, 1200 and 4000. For hot deformed and hot compacted pieces, they were broken and then attached to a sample holder by conductive tape, with the broken surface facing up.

The EDX studies were carried out to analyze the composition of the constituent elements of the phases observed in the SEM images. The X-rays emitted from the specimen which is being electron-bombarded are detected by a sensitive Si(Li) crystal detector. EDX spectrum peaks are evaluated to determine the elemental composition of the sample in a particular volume. Features or phases as small as 1 μm or less are analyzed. EDX analysis was performed using Quantax70, an additional system which is housed within the Hitachi TM3000; this system is equipped with a silicon drift detector (SDD), that operates without liquid nitrogen cooling.

Transmission electron microscope (TEM-EEELS)

The main difference between SEM and TEM, is that the former depends on the emission of secondary electrons from the surface of the sample, while the TEM is used to view ultra thin (electron transparent) samples through which electrons can pass generating a projection image.

The main parts of the microscope are: (1) an electron gun, which generates a stream of electrons, and a system of condenser lenses which focus the electrons onto the sample, (2) the image-producing system, consisting of the objective lens, movable sample holder, and intermediate and projector lenses, which focus the electrons passing through the specimen to form a real,

highly magnified image, and (3) the image-recording system consisting of a fluorescent screen for viewing and focusing the image and a digital camera for recording the images. In addition, a vacuum system is required for the electrons to travel without any scattering from the source to the sample.

The electron energy loss spectroscopy (EELS) is another technique to do compositional analysis. Typically is integrated to the TEM microscope. This technique is based on the energy loss process undergone by inelastic scattered electrons that pass through the sample. The main difference with EDX is the energy resolution, being ~1 eV or better for EELS while a few tens of eV for EDX.

The TEM images were obtained using the a high resolution TEM Hitachi HF-3300(C) 300 kV (I2TEM) at CEMES laboratory in Toulouse, France by Dr. David Reyes. TEM lamella were prepared on a dual-beam FIB-SEM (ThermoFisher Helios Nanolab 600i) with thickness ranging approximately 100-130 nm.

2.3.3 Thermogravimetric and Differential Thermal Analysis

Simultaneous thermogravimetric (TG) and differential thermal analysis (DTA) combines the measurement of a change in mass of a sample as a function of temperature with the temperature difference between the sample and a reference during constant heating/cooling rate. This device allows to determine whether an endothermic or exothermic transition is associated with mass loss in contrast to a melting or crystallization process.

The technique takes advantage of the heat absorption when a sample undergoes a physical transformation. When the sample undergoes a phase transition, more or less (depending on whether the process is exothermic or endothermic) heat will need to flow to it than the reference to maintain both at the same temperature. For example, in the case of a melting process, it will require more heat flowing to the sample to increase its temperature at the same rate as the reference. This is due to the absorption of latent heat by the sample as it undergoes the endothermic phase transition from solid to liquid. Likewise, as the sample undergoes exothermic processes (such as crystallization) less heat is required to raise the sample temperature.

The TG is also used to determine the T_C. The magnetic sample is placed in a tared TG pan located near a magnet which is placed over/under the pan. The magnet has to be strong enough to produce an apparent mass loss/gain (depending on the position of the magnet) of

approximately 2%. When the sample is heated over T_C, it loses its ferromagnetic properties, resulting in a apparent mass loss/gain that can be detected by the TG.

A Perkin Elmer Diamond TG/DTA was used in this work. Samples of approximately 30 mg were weighed to a precision of 0.001 mg. Typical scans were recorded from room temperature to 1000°C at a heating rate of 10°C/min under Ar gas at a flow rate of 200 ml/min.

2.3.4 Vibrating sample magnetometer (VSM)

A VSM was used to measure the magnetic and thermomagnetic properties of the samples. The VSM is based on Faraday's law. In a VSM, a sample is placed within sensing coils, and then it is vibrated in a sinusoidal motion, this motion introduces perturbations in the external magnetic field and it generates an (emf) in the sensing coils that is proportional to the magnetic moment of the sample. The signal is amplified by a transimpedance amplifier and lock-in detected by the VSM detection module. The magnetic field may be generated by an electromagnet, or a superconducting magnet.

A VersaLab 3 T cryogen-ree PPMS, with a temperature range of 50-400 K (sensitivity 0.16 μemu, magnet: 0.016 mT) from Quantum Design and a high field VSM with a superconducting magnet up to 14 T cooled with He closed circuit refrigerator (CFMS from Cryogenic Ltd) were employed. The calibration of VSM was performed using a Ni standard sample.

Anisotropy field measurements were performed on oriented samples prepared by mixing the powders with a cold-curing epoxy structural adhesive (RS 132-605) placed in a gel capsule and dried under a 2 T magnetic field. A chain structure develops under the field, as shown Fig. 2.8(a). To do the magnetic measurement the gel capsule was placed in a plastic straw. The straw did not give any magnetic contribution to the measured signal and the gel cap only showed a small diamagnetic contribution, as shown in Fig 2.8(b). Other way of sample preparation was by placing the powders in a teflon mold (4 of diameter and 5 mm of length) with wax, then heated up to 60°C, and afterward dried under a 2 T magnetic field. For hot deformed pieces, a small rectangular prism shaped was cut using an electrical discharge (spark erosion) machine EDM ONA Prima E-250. The hysteresis loop was measured in two directions, along and perpendicular to the pressing direction.

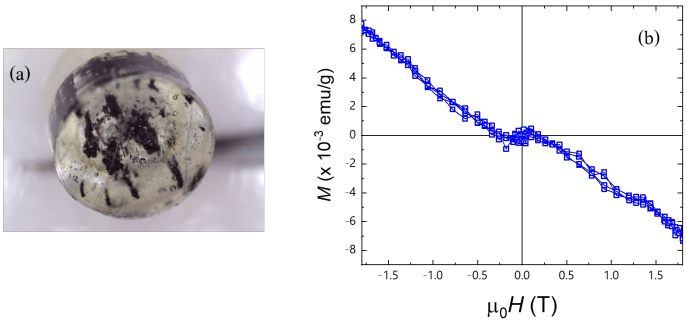

Figure 2.8: (a) Gel cap cross section of cured oriented powder. (b) Diamagnetic contribution of the gelcap.

2.3.5 Mössbauer spectroscopy

Mössbauer spectroscopy is a technique based on recoil-free, resonant absorption and emission of γ-rays in solids. Only a few nuclei are appropriate for this technique. The most common one is ^{57}Fe which is present in a 2% atomic concentration in natural Fe. As the main component of all compounds studied in this thesis is Fe, Mössbauer spectroscopy is a very important technique for their microscopic study. Figure 2.9 is a schematic illustration of a regular setup used in a ^{57}Fe Mössbauer transmission experiment. The setup has 4 main components: the γ-rays source, the drive system, the absorber (sample) and the γ-rays detector. The spectral line shape of source and absorber approximates to the ideal nuclear transition of Lorentzian line shape. For example, the ^{57}Fe 14.4 keV excited state of mean lifetime $\tau \approx 1.4 \times 10^{-7}$s corresponds to a Lorentzian line of width $\Gamma_{nat} \approx 10\times^{-9}$eV ($\gamma\tau = h/2\pi$). In practice a combined source and absorber linewidth of $\Gamma_{obs} = \Gamma_s + \Gamma_a \approx 0.24 mm/s$ can be obtained in the laboratory compared with the ideal value for the minimum observable linewidth of $2\Gamma_{nat} = 0.194 mm/s$. The additional broadening is due mainly to thickness effects in sample and to external vibrations.

In a regular Mössbauer setup, the γ-rays are emitted by the source that is moving toward and away from the sample at a velocity of a few mm/s. The movement of the source produces a change of energy via Doppler-Fizeau effect. The modulated γ-rays pass through an absorber that is stationary (the sample) and are detected by a radiation detector. When the incident radiation energy corresponds to the nuclear transition energy, the radiation is absorbed, and therefore the intensity decreases. The output of the detector, after amplification, is processed by a single channel analyzer. The logic pulses from it are further analyzed by a multichannel

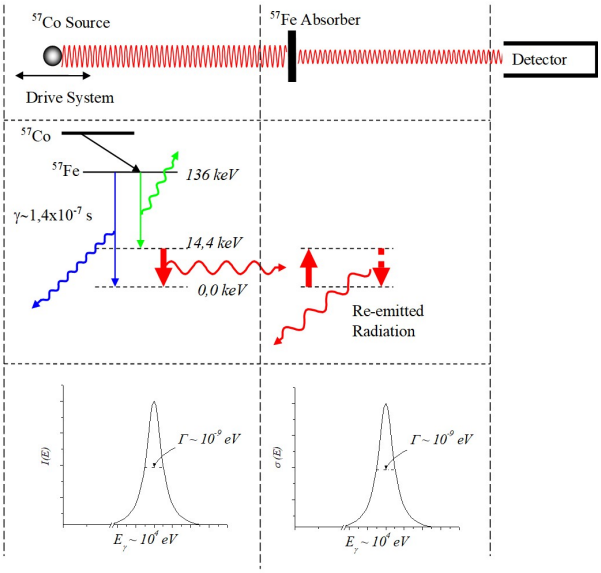

Figure 2.9: Schematic representation of a standard Mössbauer transmission experiment. The decay scheme of ^{57}Co source to ^{57}Fe is also shown with the 14.4 keV Mössbauer transition indicated by the heavy arrows. The high resolution of a Mössbauer experiment can be appreciated from the width of the Lorentzian line shapes for emission and absorption compared with E_γ the energy of the transition ($\Gamma/E_\gamma \sim 10^{-9}/10^{4} \sim 10^{-13}$)

analyzer as a function of the source velocity (energy). A Mössbauer spectrum is thus a plot of the transmitted gamma rays through an absorber versus velocity of the source.

Resonant absorption occurs when the atoms in the emitting and absorbing matrices are in identical environments. In the more common case, the emitting and absorbing materials differ, and resonant absorption will occur at slightly different energies.

Nuclei in the absorber atoms undergo several interactions with the sourronding, which are reflected in the emission or absorption of a γ-ray. The nuclear energy levels change or split due to hyperfine interactions with the electronic and magnetic environment, so these changes in energy levels can be used to provide information about the local structure and properties of the atoms in a system. The energy levels perturbation of the absorbing nuclei are reflected in the isomer shift (δ), quadrupole splitting (QS), and magnetic hyperfine splitting (B_{hf}).

Isomer shift: isomer shift arises as a result of the Coulomb interaction between the nuclear charge and the electron charge density at the nucleus. Any difference in the s-electron environment between the source and absorber will result in a shift in the resonance transition energy.

Isomer shift is useful in determining valence states, ligand bonding states, electron shielding and the electron-drawing power of electronegative species.

Quadrupole splitting: nuclei in states with an angular momentum quantum number $I > 1/2$ have a non-spherical charge distribution. This produces a nuclear quadrupole moment. In the presence of an asymmetrical electric field this splits the nuclear energy levels. The charge distribution is characterized by a single quantity called the Electric Field Gradient.

Magnetic hyperfine splitting: hyperfine splitting is caused by the dipole interaction between the nuclear spin moment and a magnetic field, i.e., the Zeeman splitting. The effective magnetic field experienced by the nucleus is a combination of the applied magnetic field and another three fields: $\boldsymbol{B}_{\text{contact}}$ is due to the spin density of s-electrons penetrating the nucleus, which are polarized by magnetic interactions with the magnetic electrons, $\boldsymbol{B}_{\text{orbital}}$ is due to the orbital moment of magnetic electrons, which is almost quenched in $3d$ elements, and $\boldsymbol{B}_{\text{dipolar}}$ is the dipolar field due to the spin of magnetic electrons other than s-electrons.

In the present work, ^{57}Fe Mössbauer spectra were obtained at room temperature, with a 25 mCi ^{57}Co/Rh source, on a constant-acceleration 512-channel spectrometer. The calibration, performed with bcc-iron foil, gave a linewidth for the external peaks of 30 mm/s. The final natural iron concentration in the samples was around 12 mg/cm^2. The spectra were fitted with the software NORMOS, developed by Richard Brand [83]. The estimated errors were at most ±0.1 T for hyperfine fields, ±0.005 mm/s for isomer shifts, and ±0.01 mm/s for the quadrupole splitting.

Chapter 3

Intrinsic magnetic properties in Sm-Fe-M (M = V, Ti) systems

3.0.1 Introduction

In response to the increasing limitations on critical R metals supplies [1, 2], a global effort is being devoted to find R-lean/free magnetic phases suitable for permanent magnets applications. As a result, there has been a renewed interest in the $R(Fe,M)_{12}$ compounds, that were studied in the late 80's and early 90's, because of the reduced R content, as compared with the other R based compounds. Recently, there have been reports investigating the stability of the $R(Fe,M)_{12}$ phase by replacing the R = Nd or Sm with less expensive R metals, such as Ce [69, 84], or even by non R metals, for instance Zr [85, 86, 87].

In all the cases, there is a need of stability studies, prior or in parallel with the optimization of composition and the magnetic properties of the 1:12 phases. In addition to the commonly used structural, microstructural, thermal and magnetic characterization techniques, the use of spectroscopy tools as Mössbauer spectroscopy, can give a special insight on the local environment and its influence on the stability of different compounds.

This chapter is devoted to the study of the stability of Sm based 1:12 phases with different substitutions for R and M elements, and their intrinsic magnetic properties. The first section shows an example of how Mössbauer spectroscopy can resolve different chemical environments in a 1:12 structure. In particular, the preference of Co occupation is analyzed when Sm is

replaced by Ce in a series of compounds of $(Sm_{1-x}Ce_x)Fe_9Co_2Ti$ (x = 0.0, 0.25, 0.50, 0.75, 1.0). Despite Ce-based 1:12 systems show poor magnetic properties [84, 69, 88, 70], alloys with partial Sm-substitution for Ce could be used in applications with medium performance demands. The reason behind the type and amount of the stabilizing element selected, and the amount of Co (2 atoms per unit cell), is magnetic properties optimization as already determined by others authors. For instance, the substitution of small amounts of Co for Fe in $Sm(Fe,Co)_{11}Ti$ was reported to be beneficial to the T_C, M_s and $\mu_0 H_A$ [52, 79, 87].

The second section studies the intrinsic magnetic properties of the $SmFe_{12-x}V_x$ ($0.5 \leq x \leq 2$) compounds. The stability range of the $ThMn_{12}$ structure is investigated for low V concentrations in an effort to improve the magnetic properties. In the last section, substitution of Zr for Sm in $Sm_{1-x}Zr_xFe_{11}V$ ($0 \leq x \leq 0.6$) is studied in order to analyze the evolution of the magnetic and structural properties with a non rare-earth element.

Not only the third element M in $R(Fe,M)_{12}$ is essential to stabilize the $ThMn_{12}$ structure, but also the amount of the stabilizer is an important factor in terms of the magnetic properties. Different authors have reported changes in M_s and T_C with the stabilizer concentration. For instance Verhoef et al. [89] in $YFe_{12-x}M_x$ (M = Ti, V, Mo, W) and Zhong et al. [90] in $RFe_{12-x}V_x$ (R = Er and Ho) systems reported a decrease in the magnetic moment with increase in stabilizer concentrations. Also Buschow [34] reported a decrease in the T_C in $YFe_{12-x}M_x$ (M = Ti, Mo, V, Cr) systems.

So far, in $SmFe_{12-x}V_x$ compounds, the 1:12 structure has been obtained only for high V concentration ($x \geq 1.5$) and is very difficult to synthesize it as a single phase material [53, 42, 91]. Single phase materials are required to study the intrinsic properties and in most of the cases for subsequent processing. Initially, in $SmFe_{10}V_2$ system, the formation of 1:12 was reported in the ingots subjected to very long annealing, 10 days at 950°C [42] and 2 weeks at 850-900°C [53]. However, shorter annealing times were reported later; for 1 day at 1050°C [59] and 20 hours at 1100-1200°C [10]. In the case of $SmFe_{10.5}V_{1.5}$, the 1:12 structure was obtained after annealing at 900-1000°C for 1 week [91].

Isothermal sections of Sm-Fe-V phase diagram at 1100 and 1200°C published by Sugimoto et al. [10] are shown in Fig. 3.1. Here the phase regions appearing in this system are characterized by two or three phase fields among the compounds $Sm_3(Fe,V)_{29}$, $Sm(Fe,V)_{12}$, $Sm_2(Fe,V)_{17}$, α-(Fe,V), γ-(Fe,V) and liquid. The dashed lines in figures are expected from both experimental results and binary phase diagrams. From these results it can be seen that pure 1:12 phase is

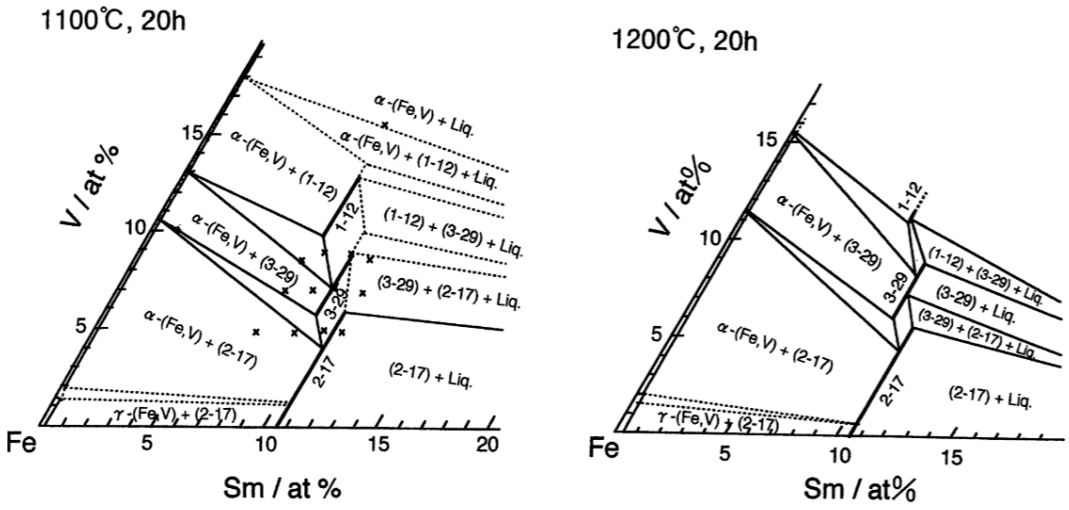

Figure 3.1: Isothermal section of the Sm-Fe-V system at 1100 and 1200°C taken from [10]

stable for 7.9 < Sm(at.%) < 9.5 and 7.1 < V(at.%) < 12.9 at 1100°C. If Sm is equal to 7.7 at.% (equivalent to 1 atom of Sm per unit cell), a combination of 1:12 phase and α-(Fe,V) can be obtained when V is equal to 10 at.%. Considerable changes in the 1:12 stability are produced with 100°C of difference therefore it may be possible to change the stabilitity range by using different annealing temperatures. For instance, at 1200°C the 1:12 stability moves to higher V and lower Sm concentrations. If Sm is equal to 7.7 at.% and V to 11 at.% (equivalent to 1.4 atoms per unit cell) is possible to stabilize the pure 1:12 phase.

In the last section, substitution of Zr for Sm in $Sm_{1-x}Zr_xFe_{11}V$ ($0 \leq x \leq 0.6$) is studied in order to analyze the evolution of the magnetic and structural properties with a non rare-earth element. Despite Zr being more expensive than Ce or Sm, it is not considered as a critical raw material. According to the previous studies [92, 93], Zr atoms occupy only the rare-earth $2a$ sites. Sakurada et al. [76] reported that substitution of Nd with Zr stabilized the $ThMn_{12}$ phase even for $x \approx 0.75$ in $Nd_{1-x}Zr_xFe_{10}Si_2$. More recently Gabay et al. [75] synthesized $Zr(Fe,Si)_{12}$, the first RE-free $ThMn_{12}$ compound. They reported a $ZrFe_{10.4}Si_{1.6}$ system with $\mu_0 M_s$ of 1.15 T but with a very weak uniaxial anisotropy of $\mu_0 H_A \approx 1.9$ T.

Partial substitution of Zr with R = Y, La, Ce, Pr, Sm has been investigated by Gabay et al. [73] and Nd by Gjoka et al. [74]. In terms of $\mu_0 H_A$, the effect of Sm was the strongest with a value of 4.07 T in $Zr_{0.7}Sm_{0.3}Fe_{10}Si_2$. In the same direction, Tozman et al. [87] in 2018,

attained the $ThMn_{12}$ structure for $Sm_{1-y}Zr_y(Fe_{0.8}Co_{0.2})_{11.5}Ti_{0.5}$ (y = 0.1 to 0.3) compounds. However, with increase in Zr content from x = 0 to 0.3, $\mu_0 M_s$ decreased from 1.61 to 1.52 T and $\mu_0 H_A$ from 8.4 to 1.53 T. A largest T_C of 830 K was found for $(Sm_{0.8}Zr_{0.2})(Fe_{0.8}Co_{0.2})_{11.5}Ti_{0.5}$ alloy. Since Sm-substitution with Zr in Sm-Fe-Ti and Sm-Fe-Si systems has been successfully investigated, the same approach was used in this thesis in the $SmFe_{11}V$ alloy system.

3.1 Preferent Co occupation in the $Sm_{1-x}Ce_xFe_9Co_2Ti$ series: Mössbauer analysis

3.1.1 Sample preparation

The series of samples of $Sm_{1-x}Ce_xFe_9Co_2Ti$ (x = 0.0, 0.25, 0.50, 0.75, 1.0) were kindly provided by Dr. Salazar, produced at the University of Delaware, USA. The alloys were prepared by arc melting the pure elements. Ribbon samples were prepared by melt spinning technique, where the molten alloy was ejected onto a copper wheel rotating at a linear speed of 35 m/s [94]. The as-spun ribbons shown in Fig. 3.2 were sealed in Ar and annealed at 700-850°C for 3-120 min to crystallize into 1:12 structure.

Figure 3.2: Photograph of the $Sm_{0.5}Ce_{0.5}Fe_9Co_2Ti$ as-spun ribbons. The thickness was 30 μm approximately.

3.1.2 Statistical calculation of the chemical environments

First neighbours and Wigner-Seitz cell (WSC) volumes for the different Fe crystallographic sites in $SmFe_{11}Ti$ unit cell are given in the Table 3.1.

Table 3.1: Near neighbour environments and volumes of $SmFe_{11}Ti$ unit cell derived from Wigner-Seitz analysis [14].

site	Fe($8i$)	Fe($8j$)	Fe($8f$)	WSC volume (Å^3)
Fe($8i$)	5	4	4	18.84
Fe($8j$)	4	2	4	11.94
Fe($8f$)	4	4	2	11.64

When Fe atoms occupy the three inequivalent $8i$, $8j$, and $8f$ crystallographic sites and Ti atoms occupy only the $8i$ sites, at least three sextets, corresponding to the $8i$, $8j$ and $8f$ sites, are required to fit the Mössbauer spectra. However, when Ti enters randomly into the structure, it creates different chemical environments around the Fe atoms and, therefore, each crystallographic site would have several different environments. This means that the three sextets must be further subdivided to take into account the distribution of the titanium atoms in the neighbourhood of each of the Fe sites.

The substitution of Fe by Co, also produces new environments. However, as Co is a magnetic atom and is next to Fe, it was considered that its presence would not affect too much the hyperfine levels in such environments. In the following, it was assumed that a number of Co atoms in an environment do not create a new splitting nor another set of subspectra, although this environment will be affected by the presence of Co [95].

In the first step of the analysis, the relative sextet areas were calculated by using a binomial distribution,

$$P(n,m) = \frac{(n+m)!}{n!m!} p^n (1-p)^m, \tag{3.1}$$

where $P(n,m)$ is the probability of an environment with n Fe atoms and m Ti atoms, and p is the Fe concentration at that site. These relative areas are associated with the Mössbauer resonant areas of Fe nuclei at each site. Table 3.2 presents the number of Fe and Ti atoms per site in the stoichiometry of $SmFe_{11}Ti$. These values allows us to calculate the Fe concentration per site.

Table 3.2: Number of Fe and Ti atoms at each site $SmFe_{11}Ti$ unit cell

site	Total	Fe	Ti
$8i$	8	6	2
$8j$	8	8	0
$8f$	8	8	0
Total	24	22	2

Table 3.3 shows all the environments together with their probability of occurrence. For example, an iron atom in $8i$ site will have a 6.47% of probability of having 5 Fe and 0 Ti neighbours, 10.79% of probability to have 4 Fe and 1 Ti neighbours and so on. Summarizing, there are 16 different environments for Fe atoms, which implies that it would be needed a total of 16 subspectra to fit the Mössbauer spectra.

Table 3.3: Atomic distribution and the probabilities of each magnetic environment of each position of Fe, $P(n_{\mathrm{Fe}}, m_{\mathrm{Ti}})$ is the probability of an Fe atom that has n Fe atoms and m Ti atoms.

Mössbauer atom	Neighbor $8j$		Neighbor $8f$		Neighbor $8i$		Total	$P(n_{\mathrm{Fe}}, m_{\mathrm{Ti}})$ (%)	Normalized probability
	nFe	mTi	nFe	mTi	nFe	mTi	Fe n		
Fe($8i$)	4	0	4	0	5	0	13	6.47	6.90
	4	0	4	0	4	1	12	10.79	11.50
	4	0	4	0	3	2	11	7.19	7.7
	4	0	4	0	2	3	10	2.40	
	4	0	4	0	1	4	9	0.40	
	4	0	4	0	0	5	8	0.03	
Fe($8j$)	2	0	4	0	4	0	10	11.51	12.30
	2	0	4	0	3	1	9	15.34	16.40
	2	0	4	0	2	2	8	7.67	8.20
	2	0	4	0	1	3	7	1.70	
	2	0	4	0	0	4	6	0.14	
Fe($8f$)	4	0	2	0	4	0	10	11.51	12.30
	4	0	2	0	3	1	9	15.34	16.40
	4	0	2	0	2	2	8	7.67	8.20
	4	0	2	0	1	3	7	1.70	
	4	0	2	0	0	4	6	0.14	

However, there are several environments with probabilities lower than 3%. These environments were discarded because they were in the limit of the measurement resolution. The probabilities were renormalized and the new values are shown in the last column of the Table 3.3. Only nine sextets with their corresponding areas (the $8i$ sextet is subdivided into three sextets with 6.9, 11.5, and 7.7 percent areas, and each of the $8j$ and $8f$ sextets is subdivided into three sextets with 12.3, 16.4, and 8.2 percent areas) were used to simulate the $ThMn_{12}$ phase, labeled as i_0, i_1, i_2; j_0, j_1, j_2; f_0, f_1, f_2, where the subscript refers to the presence of 0, 1, 2 adjacent Ti neighbours to the i, j, f Fe atom.

3.1.3 Spectra classification

Three hyperfine parameters define each sextet, the hyperfine field (B_{hf}), the isomer shift (δ) and the quadrupole shift (QS). In order to reduce the number of free parameters, it was assumed that the three hyperfine parameters of the nine sextets (for each crystallographic inequivalent Fe site) varied linearly with the number of Ti near neighbours. The δ is very sensitive to the different chemical environments. From previous works in similar compounds, it was observed that an increase of the nonmagnetic atom (at expenses of Fe) resulted in a decrease of the δ [96], so this was assumed true here too.

The areas ratios were also fixed. For instance, for $8i$ site the areas were 6.9, 11.5 and 7.7 (see Table 3.3), so the system was constraint to $A_2 \approx A_1\,(11.5/6.9)$, $A_3 \approx A_1\,(7.7/6.9)$. For $8j$ the areas were 12.3, 16.4, 8.2, and the constraints $A_5 \approx A_4\,(16.4/12.3)$ and $A_6 \approx A_4\,(8.2/12.3)$.

According to the XRD results [94], in addition to 1:12 phase, α-Fe was also present, then ten sextets were used to fit the Mössbauer spectra, nine sextets for 1:12 phase and one for α-Fe. In total 27 hyperfine parameters, one linewidth, and one total absorption area were used to fitting the spectra.

The WSC values (Table 3.1) of the three inequivalent Fe sites in $SmFe_{11}Ti$ indicates that the $8i$ site has the largest average number of Fe near neighbours, whereas the $8j$ and $8f$ Fe sites have only nine Fe near neighbours. Consequently, the sextets with the largest B_{hf} were assigned to the $8i$ site, both on the basis of its percent contribution and its Fe near-neighbour environment. As $8j$ and $8f$ sites have identical percentage areas and Fe near-neighbour environments, their assignment was based on the δ on the basis of the WSC volume analysis, i.e. $8j > 8f$.

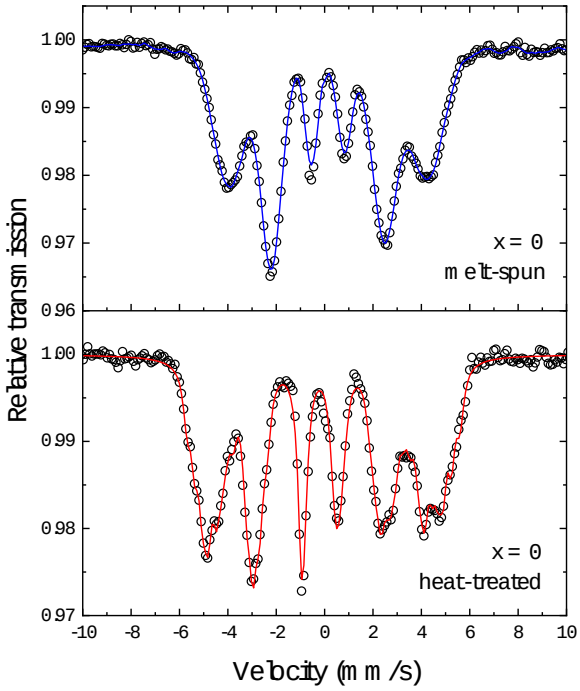

Figure 3.3: Mössbauer spectra comparison of as-spun and heat-treated $Sm_{1-x}Ce_xFe_9Co_2Ti$ ($x = 0.0$) ribbons

3.1.4 As-spun ribbons

The Mössbauer spectra of as-spun and heat-treated $Sm_{1-x}Ce_xFe_9Co_2Ti$ ($x = 0.0$) ribbons, obtained at 300 K are shown in Fig. 3.3. Here, the difference between spectra of the amorphous (as-spun) and crystallized ribbons (heat-treated) is clear. The first one presents much wider lines than the crystallized. Such a broadening is due to chemical and structural disorder, because there are plenty of different equivalent positions. Other features are also visible, for example, (i) the outer lines are wider than inner ones and they follow the relation $\Gamma_1 > \Gamma_2 > \Gamma_3$, and $\Gamma_6 > \Gamma_5 > \Gamma_4$. Being Γ_i the line width i, indexed from negative to positive velocity, (ii) the position of the absorption peaks is symmetric with respect to the centre of the spectrum and (iii) the resonant areas follow the relations $A_1 < A_6$, $A_2 > A_5$ and $A_3 > A_4$.

Due to the disordered nature of as-spun ribbons, the Mössbauer spectra were fitted with a distribution of hyperfine magnetic fields ($\langle B_{\rm hf} \rangle$). The theoretical spectra were produced with a superposition of 40 subspectra and variation of δ as well. Fig. 3.4 shows the field distributions obtained for all samples. For low concentrations of Ce ($x < 0.5$), the field distributions show an

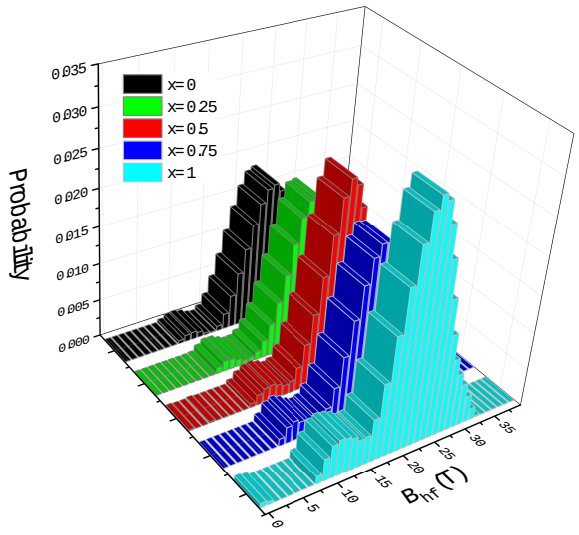

Figure 3.4: Hyperfine field distribution of $Sm_{1-x}Ce_xFe_9Co_2Ti$ (x = 0.0, 0.25, 0.50, 0.75, 1.0) as-spun ribbons

almost unimodal behaviour, with a sharp peak around $\langle B_{\mathrm{hf}} \rangle = 21$ T. For higher concentrations, $x > 0.5$, the environments around 10 T take importance, and it is more visible when the Sm is completely substituted by Ce, for which also the probability around 21 T becomes stronger.

3.1.5 Crystallized ribbons

The Mössbauer spectra of the heat-treated ribbons, together with their fits are presented in Fig. 3.5. Here all samples show a complete crystallization into two phases, 1:12 and α-Fe. Black circles correspond to the experimental data, the colored lines to the contribution of each environment (3 sites for 8i, 3 sites for 8j, 3 sites for 8f from $ThMn_{12}$ phase and one site for α-Fe) and the black line to the superposition of all the sextets.

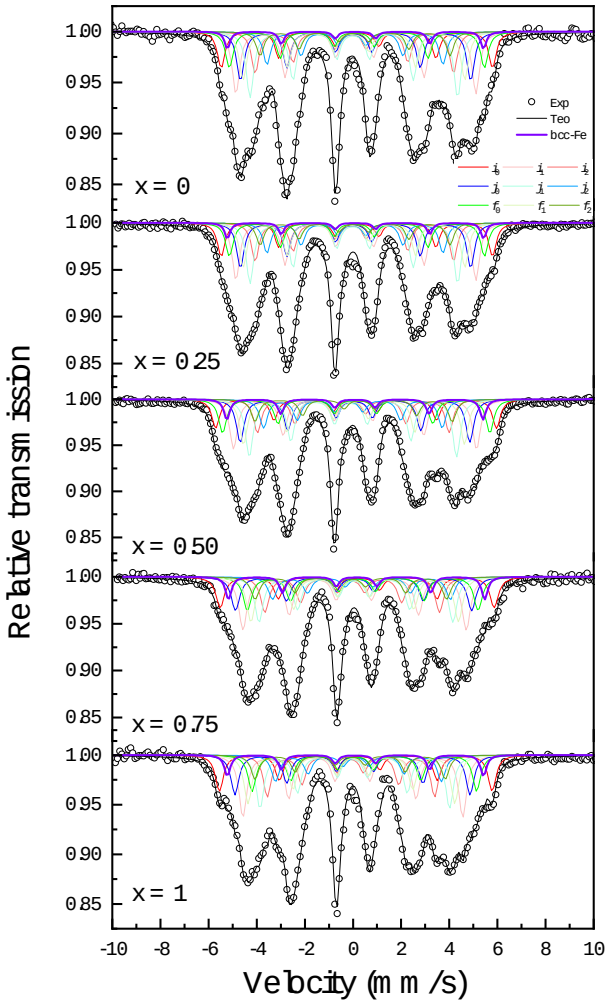

Figure 3.5: Mössbauer spectra of $Sm_{1-x}Ce_xFe_9Co_2Ti$ at 300K. Nine sextets, corresponding to the 1:12 phase (colored lines) and one to the α-Fe (purple line) are shown. The black solid line corresponds to the superposition of all sextets

From Fig. 3.5, it is evident that the resonant area of α-Fe phase (purple curve) is much smaller than the resonant areas of $ThMn_{12}$ phase. Also the shape of the spectra changes when the Ce concentration is higher than 0.5, especially through modifications in the $8j$ and $8f$ sites, as it can be verified in the fitted values of Table 3.4.

Table 3.4: Mössbauer parameters for heat-treated $Sm_{1-x}Ce_xFe_9Co_2Ti$ ribbons, $\langle\delta\rangle$: isomer shift, B_{hf}: hyperfine field, QS: quadrupole splitting and the resonant area. The nCo corresponds to the Co occupation.

x	Site	$\langle\delta\rangle$ (mm/s)	$\langle B_{hf}\rangle$ (T)	$\langle Q\rangle$ (mm/s)	Area (%)	nCo
0.00	8i	-0.120	30.5	0.065	34.3	0.0
	8j	-0.148	28.6	0.086	26.6	1.5
	8f	-0.164	26.4	0.077	36.1	0.5
	α-Fe	-0.087	33.0	0.000	3.1	
0.25	8i	-0.120	30.4	0.094	34.2	0.0
	8j	-0.107	28.8	-0.008	27.7	1.4
	8f	-0.187	26.4	0.087	36.2	0.6
	α-Fe	-0.087	33.0	0.000	1.8	
0.50	8i	-0.141	30.7	0.074	31.3	0.0
	8j	-0.098	29.4	-0.029	28.2	1.4
	8f	-0.200	26.4	0.091	36.0	0.6
	α-Fe	-0.087	33.0	0.000	4.4	
0.75	8i	-0.190	28.8	0.018	35.3	0.0
	8j	-0.108	26.1	0.047	30.0	1.0
	8f	-0.169	27.0	0.095	29.8	1.0
	α-Fe	-0.087	33.0	0.000	4.8	
1.00	8i	-0.182	28.3	-0.021	36.4	0.0
	8j	-0.123	25.4	0.031	31.2	0.9
	8f	-0.153	26.7	0.099	28.3	1.1
	α-Fe	-0.087	33.0	0.000	4.2	

Table 3.4 summarizes the Mössbauer parameters of the heat-treated ribbons. From the resonant areas the occupation of Co atoms for each site were calculated. From the results it can be seen that for concentrations up to 0.5, 70% of Co occupies 8j sites and 30% 8f sites, while for concentrations above 0.5, there is a redistribution of Co: About 50% goes to 8j and 50% to 8f. This is in agreement with the decrease of the hyperfine field in the 8j site while the hyperfine field of 8f site is increasing. The tendency of the δ also shows variations for concentrations above 0.5.

3.2 Study of $SmFe_{12-x}V_x$ series

3.2.1 Sample preparation

Ingots of $SmFe_{12-x}V_x$ (x = 2.0, 1.5, 1.0, 0.5) alloys were prepared by arc melting in Ar atmosphere. Samarium loss during the melting was compensated by adding an appropriate excess amount. The ingots were homogenized at temperatures ranging from 900 to 1100°C for 1-3 days and then quenched in water. The annealed ingots were ground in a mortar and the fine powders were used for XRD measurements. Anisotropy fields were determined from the initial magnetization curves of oriented samples measured ∥ and ⊥ to the oriented direction.

Figure 3.6: Arc-melted polished Sm-Fe-V ingots.

3.2.2 Structural properties

The XRD patterns of $SmFe_{12-x}V_x$ (x = 2.0, 1.5, 1.0 and 0.5) alloys with different V concentration heat-treated at 1000°C for 2 days are presented in Fig. 3.7. Apart from the sample with x = 0.5, the main phase in all the samples is $ThMn_{12}$-type (space group $I4/mmm$), with a very low content of α-(Fe,V) (space group $Im\bar{3}m$) around 0.5-1%.

Along the series, the parameters a and c decrease almost linearly from 8.522 and 4.765 to 8.509 and 4.758 Å, respectively with decreasing V concentration from x = 2.0 to 1.0, as seen in Fig. 3.8. The lattice contraction with decreasing V concentration makes the characteristic 1:12 peaks to shift slightly towards higher angle. This is reasonable considering the atomic radius of V (1.34 Å [97]), which is larger than that of Fe (1.26 Å [97]). The cell volume decreased from 346.05 to 344.52 $Å^3$. For x = 0.5 alloy, the rhombohedral Th_2Zn_{17}-type structure and α-(Fe,V) were observed. Different heat treatments were performed in the range of 900-1100°C for 1 and 3 days but the 1:12 phase did not formed.

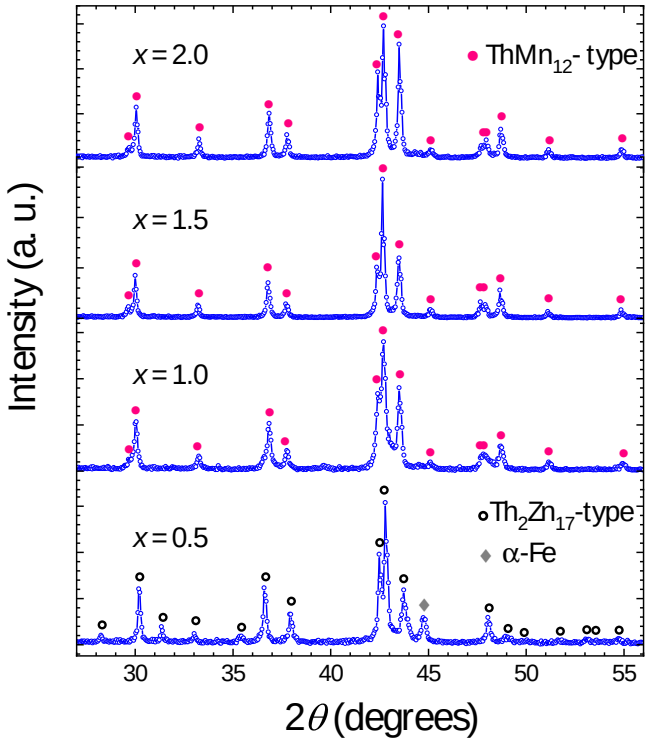

Figure 3.7: The XRD patterns of $SmFe_{12-x}V_x$ alloys with different V concentration annealed at 1000°C for 2 days.

BSE-SEM images of the as-cast and annealed samples are shown in Fig. 3.9. Examination of the as cast sample (Fig. 3.9(a)) revealed the composition of the light gray areas to be Sm: 33.8 at.%, Fe: 61.8 at.% and V: 4.4 at.%, the dark gray areas to be Sm: 13.6 at.%, Fe: 80.7 at.% and V: 5.7 at.%, and darker inclusions to be Sm: 1.4 at.%, Fe: 88.0 at.% and V: 10.6 at.%. The excess Sm appears as lighter inclusions, which are more visible in the inset of Fig. 3.9(a). After annealing, no phase contrast was observed in the BSE-SEM image (Fig. 3.9(b)), confirming the nearly pure $SmFe_{11}V$ phase.

3.2.3 Magnetic properties

Macroscopic properties

The T_C values of $SmFe_{12-x}V_x$ (x = 2.0, 1.5, 1.0) annealed samples were determined by using a thermogravimetric analyser with a magnet. An example plot, for x = 1, is shown in the inset of

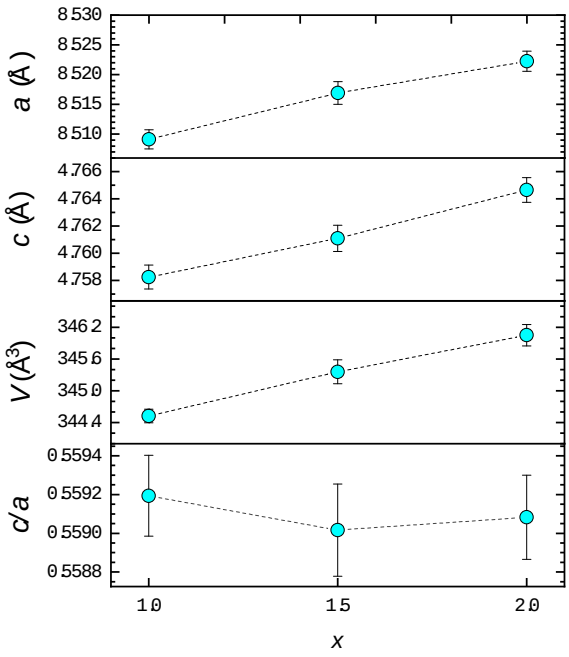

Figure 3.8: Variation of lattice parameters of $SmFe_{12-x}V_x$ (x = 2.0, 1.5, 1.0) alloys annealed at 1000°C for 2 days.

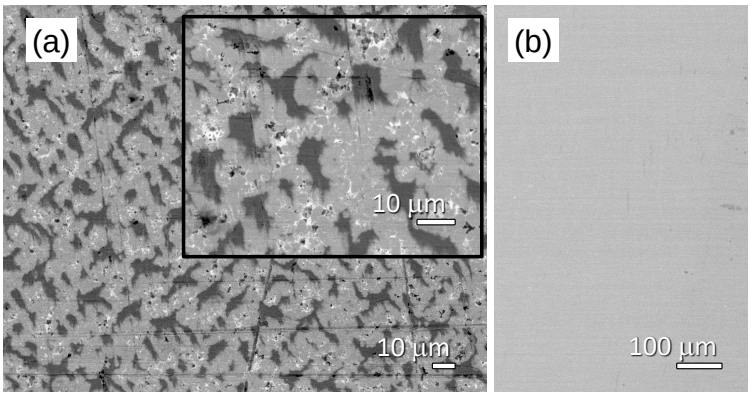

Figure 3.9: BSE-SEM images of $SmFe_{12-x}V_x$ (x = 1) (a) as-cast alloy and (b) annealed at 1000°C for 2 days.

the Fig. 3.10. When heated, the sample loses its ferromagnetic properties at T_C, resulting in an apparent mass gain that can be detected by the TGA. As Fig. 3.10 displays, the T_C increases when V concentration is reduced. The T_C of $SmFe_{12-x}V_x$ compounds is determined by the Sm-Sm, Sm-V, Sm-Fe and Fe-Fe exchange interactions. Among them, the Fe-Fe interactions are

the strongest, and in a first approximation they determine the ordering temperature. Therefore, it is reasonable that when the V concentration is reduced, the number of Fe-Fe interactions is increased and hence the T_C is increased. The non-linearity of the T_C dependence on V concentration is also observed. This non-linearity behavior has been recently predicted by T. Fukazawa et al. [98] in $RFe_{12-x}Cr_x$ (R = Sm, Nd and Y) at low concentrations of Cr.

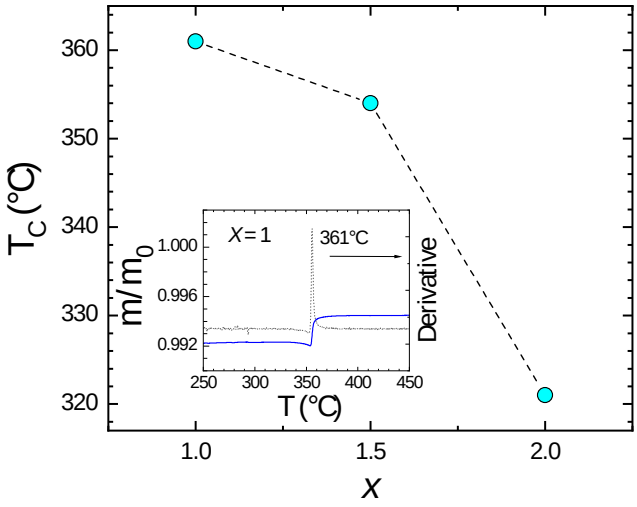

Figure 3.10: Dependence T_C on V concentration $SmFe_{12-x}V_x$ heat-treated alloys. The inset shows a TGA plot for $x = 1$.

Figure 3.11(a) shows the isothermal magnetization curves of oriented powders measured at room temperature along ($\parallel$) and perpendicular ($\perp$) to the magnetic field. The M_s for $x = 2$ is 83 Am^2/kg (0.81 T, 12.0 μ_B/ f.u.), which is consistent with the values reported by Ohashi et al. [42] (79.6 Am^2/kg) and Wang et al. [59] (85 Am^2/kg). An M_s value of 115 Am^2/kg (1.12 T, 16.8 μ_B/ f.u.) was obtained for $SmFe_{11}V$ ($x = 1$), which is 35% higher than M_s of $SmFe_{10}V_2$ ($x = 2$). Assuming the magnetic moment of the Sm atoms is 1.5 μ_B [11], and the coupling of the Sm and Fe moments to be parallel, the average magnetic moment per Fe atom would be 1.1 μ_B/Fe ($x = 2$) and 1.4 μ_B/Fe ($x = 1$), which means that the increase of magnetization when V is reduced, is due to the increase of the magnetic moment per Fe atom (32%) also and not just due to the increase of Fe concentretion (10%).

The $\mu_0 H_A$ value was determined by plotting M in the $\perp$ direction as a function of $[(\mu_0 H)^{-2}]$, where a change in the slope of the M in the vicinity of $\mu_0 H_A$ is expected, because at this point a transition from macroscopic to microscopic spin rotations takes place [99]. As the change of slope

in M was not clear, it was considered that the minimum of the M derivative (see Fig. 3.11(b)) was related with the anisotropy field, as other authors have done it recently [87, 100]; these values are consistent with those obtained from a rough estimation of the point at which the ∥ and ⊥ initial magnetization curves merge (the difference is less than 10%).

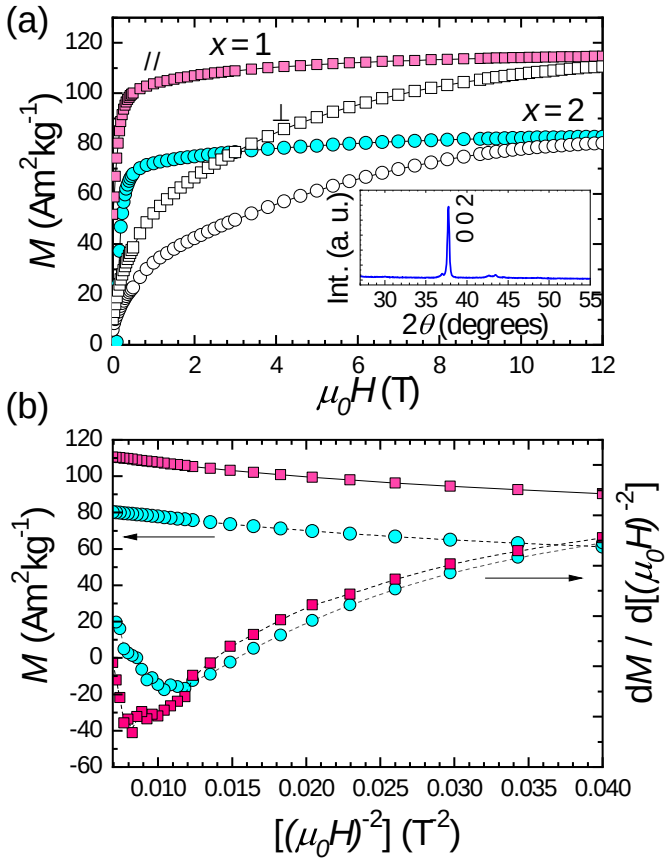

Figure 3.11: (a) Magnetization curves of magnetically aligned powder particles of $SmFe_{10}V_2$ (x = 2) and $SmFe_{11}V$ (x = 1) measured at room temperature in parallel (∥) and perpendicular (⊥) direction to the magnetic field. The inset shows the XRD pattern of the oriented $SmFe_{11}V$ compound, indicating the easy magnetization direction (002) along the c-axis. (b) M and $\mathrm{d}M/\mathrm{d}[(\mu_0 H)^{-2}]$ as a function of $[(\mu_0 H)^{-2}]$. The anisotropy field is determined from the derivative minimum.

For x = 1, $\mu_0 H_A$ is found to be 1.1 T, which is slightly higher than for x = 2. The difference can be attributed to a higher contribution from the second order anisotropy constant K_2 for x = 1. An anisotropy field of 9.8 T was obtained for x = 2. This is 1 T higher than the value reported by Grössinger et al. [101], which was determined by the singular point detection method

Table 3.5: Experimental magnetic properties of $SmFe_{12-x}V_x$ heat-treated alloy.

x	$\mu_0 M_s$ (T)	M_s (μ_B/f.u.)	$\mu_0 H_A$ (T)	$K_1 + 2K_2$ (MJ/m^3)	MAE (MJ/m^3)	T_C (°C)
2.0	0.81	12.0	9.8	3.2	1.58	321
1.0	1.12	16.8	11.0	4.9	1.92	361

using pulsed fields. An effective anisotropy constant was determined by using the equation $\mu_0 H_A = 2(K_1 + 2K_2)/\mu_0 M_s$ [102], and the MAE was determined by calculating the area between the $\parallel$ and $\perp$ direction curves. These results are summarized in Table 3.5. Coercivity of the optimally annealed samples found to be around 0.045 T.

Local magnetic properties: Mössbauer analysis

The Mössbauer spectra at room temperature for $SmFe_{12-x}V_x$ (x = 2.0, 1.5, 1.0) heat-treated alloys, and the fits are shown in Fig. 3.12. The spectra were fitted according to the local environment of each of the three crystallographic Fe sites, 8*i*, 8*j* and 8*f*, and considering the 8*i* as the preferred site of V atoms. The choice of the 8*i* site for the V atoms was based on the results of previously reported neutron diffraction studies in $RFe_{12-x}V_x$ (R = Y, Tb, Er, Nd, Dy, Ho, Er) [103, 104, 38]. A visual inspection of the spectra indicates that is necessary to use more than three sextets to fit the spectra.

The statistical distribution of V atoms over 8*i* site modifies the local environment of each 8*i*, 8*j* and 8*f* Fe atom, and thus the spectra of 8*i*, 8*j* and 8*f* sites are split in a set of subspectra. Each subspectrum corresponds to one different environment, i.e. a different number of V atoms, around the Mössbauer nuclei. The number and the relative areas of each subspectrum was calculated from a binomial distribution [48]. The environments with probabilities lower than 3% were discarded. Nine sextets (3 for 8*i*, 3 for 8*j* and 3 for 8*f*) were used to fit the spectrum for x = 1, eleven (3 for 8*i*, 4 for 8*j* and 4 for 8*f*) for x = 1.5 and ten (4 for 8*i*, 3 for 8*j* and 3 for 8*f*) for x = 2. The sum of all the subspectra for a given site is presented in each spectrum of Fig. 3.12. The assignment of the Fe sites was according with reports by Denissen et al. [96], where the site dependence of hyperfine fields follows the condition 8*i* > 8*j* > 8*f*. The linewidths and areas of the relative subspectra were fixed, and the total area of a given site, i.e. the sum of all the subspectra of such site, was a free parameter.

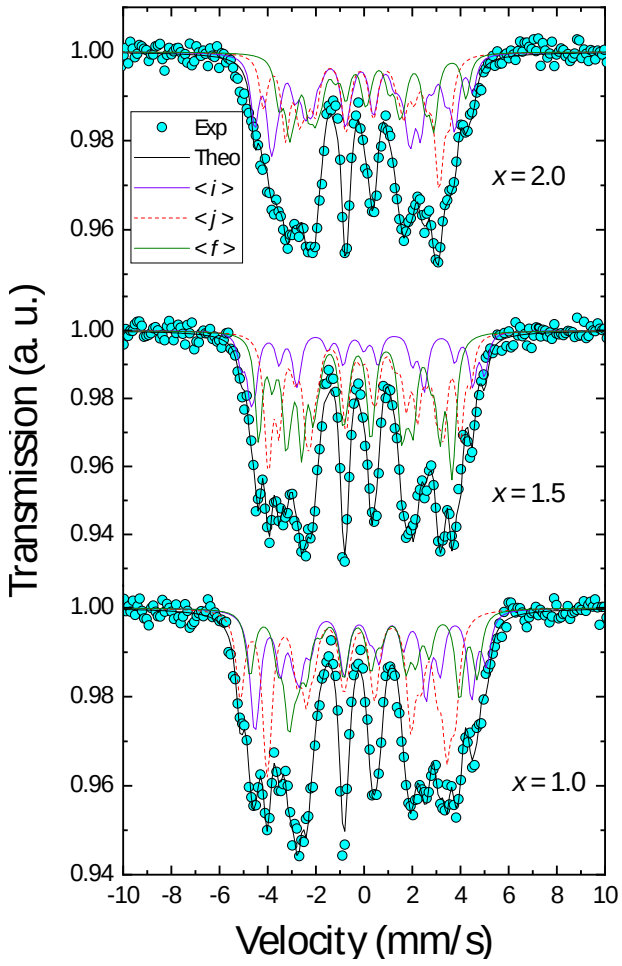

Figure 3.12: Room temperature Mössbauer spectra for $SmFe_{12-x}V_x$ with different V concentration x.

Average $\langle B_{\rm hf}\rangle$ and average of $\langle\delta\rangle$ of all Fe sites, as a function of V concentration x, are listed in Table 3.6. As it shows, the contribution of the $8i$ subspectra with the highest $B_{\rm hf}$ values increases when going from x = 2 to 1. When the V concentration is reduced, the probability of finding Fe atoms in $8i$ site is higher, then environments with more adjacent Fe atoms are more likely, and the hyperfine fields are larger. This effect can be seen in Fig. 3.12, when the Mössbauer spectrum of $SmFe_{10}V_2$, appears contracted in comparison with that of $SmFe_{11}V$. A similar behaviour was observed by Sinnemann et al. in $GdFe_{12-x}V_x$ and Denissen et al. in $YFe_{12-x}V_x$ series [48, 96]. The increase of $B_{\rm hf}$ values are in agreement with the results of the magnetization measurements, where there is an increase of the average moment per Fe atom

Table 3.6: Mössbauer hyperfine parameters for $SmFe_{12-x}V_x$ (x = 2.0, 1.5, 1.0). Average hyperfine field ($\langle B_{\rm hf}\rangle$), average isomer shift ($\langle\delta\rangle$), and average hyperfine field per site. The values in brackets are assumed moments of Fe in the different sites, in $\mu_{\rm B}$/Fe.

x	$\langle\delta\rangle$ (mm/s)	$\langle B_{\rm hf}\rangle$ (T)	$\langle B_{\rm hf}^{8i}\rangle$ (T)	$\langle B_{\rm hf}^{8j}\rangle$ (T)	$\langle B_{\rm hf}^{8f}\rangle$ (T)
2.0	-0.08	21.0	22.5	20.6	19.2
			[1.13]	[1.03]	[0.96]
1.5	-0.09	22.0	25.6	21.7	20.3
1.0	-0.15	25.0	26.9	24.6	23.4
			[1.50]	[1.37]	[1.30]

from 1.1 $\mu_{\rm B}$/Fe to 1.4 $\mu_{\rm B}$/Fe when going from x = 2 to 1.

It is usual that the experimental $\langle B_{\rm hf}\rangle$ values are converted to local moments by means of a factor (hyperfine constant), which is considered the same for all Fe sites, and can be defined as the ratio of the $\langle B_{\rm hf}\rangle$ to the average moment per Fe atom. For $SmFe_{11}V$, using μ = 1.4 $\mu_{\rm B}$/Fe and $\langle B_{\rm hf}\rangle$ = 25.0 T, leads to a conversion factor of 18.0 T/$\mu_{\rm B}$ and for $SmFe_{10}V_2$ a factor of 20.0 T/$\mu_{\rm B}$. With these factors, the magnetic moments of Fe at different sites were calculated, as the values listed in square brackets in Table 3.6.

The negative values of $\langle\delta\rangle$ indicate an increase in s electrons charge density at the Fe nuclei in $SmFe_{12-x}V_x$, compared to pure Fe [96]. The $\langle\delta\rangle$ decreases with decreasing V concentration. This behavior could be explained in terms of a redistribution of the $4s$ electron charge with a slightly higher tendency to be around the Fe atoms than V ones. When the V concentration is reduced, the screening effect of the $4s$ electrons is reduced as well, producing an increase of the s charge density at the nucleus and hence a decrease of the isomer shift.

3.2.4 Theoretical calculations

A collaboration was open with Dr. Vekilova, Dr. Herper and Dr. Eriksson from University of Uppsala, who studied $SmFe_{11}V$ and $SmFe_{10}V_2$ phases from first principles in order to compare our experimental results.

For the electronic structure, lattice parameters and phase stability, VASP simulation package [105, 106, 107] was used within the projector augmented wave (PAW) method [108]. The

electronic exchange and correlation effects were treated by the generalized gradient approximation (GGA) in the Perdew, Burke, and Ernzerhof (PBE) form [109]. A 13 atom cell of $SmFe_{12-x}V_x$, where $x = 1$ and 2, was considered. The plane-wave energy cut-off was set to 268 eV. The converged k-point mesh was found to be 16×16×16 Monkhorst-Pack k-points [110]. For the estimation of phase stability of ternary compounds the following equation was used:

$$\Delta H_f = \frac{1}{26}\begin{bmatrix} 2H\left(SmFe_{12-x}V_x\right) - H\left(Sm_2Fe_{17}\right) \\ -2xH\left(V\right) - (7-2x)\,H\left(\alpha\text{-Fe}\right) \end{bmatrix}, \tag{3.2}$$

where $x = 1$, 2 is the number of V atoms in the cell on the Fe sublattice. The enthalpy of the $SmFe_{12-x}V_x$ system was calculated and compared with the enthalpy of another phase stable at these conditions (Sm_2Fe_{17}) as well as with the enthalpy of pure elements, V and α-Fe. The obtained VASP lattice parameters were used for the calculation of the magnetic properties with help of the highly accurate all-electron FP-LMTO method implemented in the RSPt code [111, 112]. Integration over the Brillouin zone was performed using the tetrahedron method with Blochl's correction [113]. The k-point convergence of the MAE for the chosen supercell size was found when increasing the Monkhorst-Pack mesh [110] to 24×24×24 and it was further used in all calculations. For the treatment of the $4f$ electrons of rare-earth Sm atom the spin polarized core approximation was used.

Table 3.7 summarizes the values of formation of enthalpies, structural and magnetic properties of $SmFe_{12-x}V_x$ ($x = 1$ and 2) obtained theoretically. Negative formation enthalpy indicates that the structure is stable. Calculations show that with decreasing concentration of V from 2 to 1 the $SmFe_{12-x}V_x$ structure maintains its stability. The close numbers of the formation enthalpies with one slightly lower for the $SmFe_{10}V_2$ phase might reflect the preferential stabilization of this phase. However, $SmFe_{11}V$ is nearly as stable as $SmFe_{10}V_2$, which is consistent with the experimental results.

Table 3.7: Theoretically obtained enthalpy of formation, cell volume, c/a ratio, magnetization and MAE of $SmFe_{11}V$ and $SmFe_{10}V_2$.

x	ΔH_f (eV/u. cell)	V (Å^3)	c/a	M_s (μ_B/f.u.)	$\mu_0 M_s$ (T)	MAE (MJ/m^3)
2	-0.87	339.6	0.5519	12.4	0.85	1.31
1	-0.73	336.4	0.5520	15.8	1.00	1.66

As one can see from Table 3.7, the volume of the structure slightly reduces, but the c/a ratio remains almost unchanged with the decrease of the V concentration. That is in line with the observation made in experiment. The MAE was calculated as the energy difference between the (110) and (001) crystallographic directions. The MAE and magnetic moment of $SmFe_{11}V$ are substantially higher than those of $SmFe_{10}V_2$. Theoretically obtained MAE increases with the decrease of the V concentration in good agreement with experiment. A 26% increase of MAE was obtained when the concentration of V was reduced from 2 to 1 atom per formula unit. Theoretical values of 1.66 and 1.31 MJ/m^3 for $SmFe_{11}V$ and $SmFe_{10}V_2$, respectively, are in good agreement with corresponding experimental values of 1.92 and 1.58 MJ/m^3. An increase of the magnetization by about 18% was also observed; magnetic moment increases due to reduction of V content, which induces an increase of the Fe magnetic moment, in addition to the increase of the Fe content.

3.3 The Zr substituted $Sm_{1-x}Zr_xFe_{11}V$ series

In some 1:12 Nd compounds, the substitution of Nd by Zr has been shown to increase the stability of the 1:12 phase [76, 75]. This section reports the effect on the structural and magnetic properties of the partial substitution of Sm by Zr in $Sm_{1-x}Zr_xFe_{11}V$ ($0 \leq x \leq 0.6$). The alloys were prepared by arc melting and homogenized at temperatures ranging from 1000 to 1100°C for 3-4 days, then they were quenched in water. The Sm losses were compensated by adding appropriate amount of excess Sm.

3.3.1 Structural properties

Figure 3.13 displays the XRD patterns of the optimally annealed samples of $Sm_{1-x}Zr_xFe_{11}V$ ($0 \leq x \leq 0.6$). The major phase in all these samples is the 1:12, followed by the cubic α-(Fe,V) and the cubic laves phase $ZrFe_2$ ($MgCu_2$-type, space group $Fd\bar{3}m$). As the Zr content increases the α-(Fe,V) phase increases and the Laves phase only appears when $x \geq 4$. Laves-phase compounds occur frequently in alloy systems involving transition metals [114]. Lattice parameters and volume percentages 1:12, α-(Fe,V) and $ZrFe_2$ laves phase in each sample obtained from the Rietveld analysis of the XRD patterns are listed in Table 3.8.

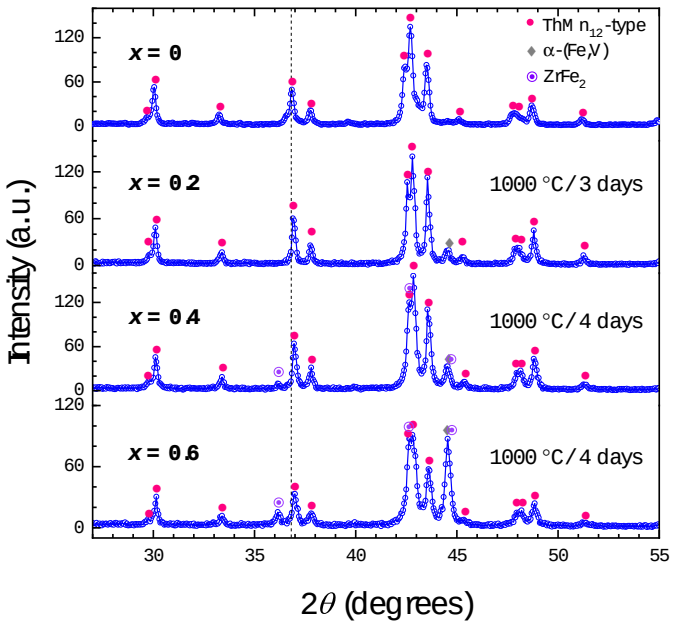

Figure 3.13: XRD patterns of optimally annealed $Sm_{1-x}Zr_xFe_{11}V$ optimally heat-treated alloys.

As Zr has a smaller atomic radius (1.60 Å [97]) than Sm (1.80 Å [97]), the substitution of Zr results in lattice contraction (unit cell decreases). A good indication of this, is the shifting of the characteristic 1:12 peaks to higher 2θ angles with increasing Zr content, as it is displayed from the vertical dashed line (Fig. 3.13).

Table 3.8: Volume fraction and lattice parameters of the phases present in $Sm_{1-x}Zr_xFe_{11}V$ ($0 \leq x \leq 0.6$) heat treated alloys.

	Volume fraction			Lattice Parameters			
x	1:12	α-(Fe,V)	$ZrFe_2$	1:12		α-(Fe,V)	$ZrFe_2$
				a(Å)	c(Å)	a(Å)	a(Å)
0.0	0.99	0.01		8.509	4.758	2.876	
0.2	0.95	0.05		8.491	4.761	2.875	
0.4	0.91	0.06	0.03	8.483	4.760	2.878	7.027
0.6	0.70	0.23	0.07	8.482	4.757	2.876	7.029

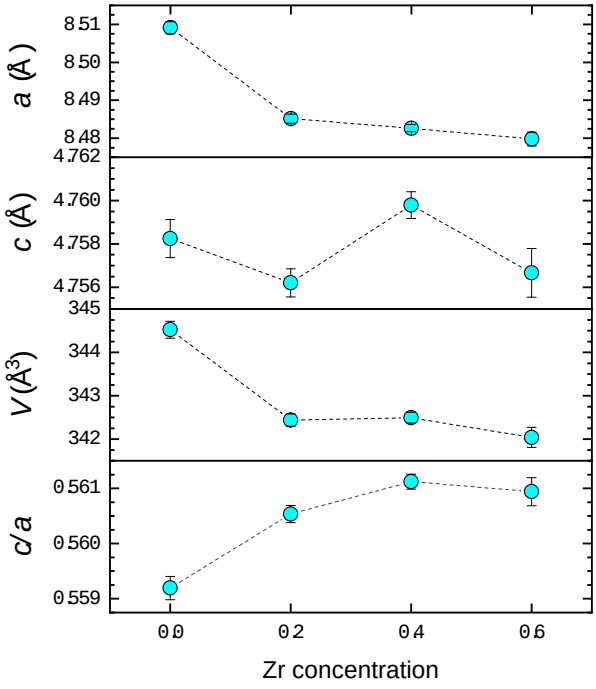

Figure 3.14: Variation of lattice parameters of 1:12 phase with Zr-content in $Sm_{1-x}Zr_xFe_{11}V$ in optimally annealed alloys.

Variations in the lattice parameters, unit cell volume and c/a ratio of 1:12 phase are shown in Fig. 3.14. The constant a decreases monotonically from 8.509 to 8.482 Å with increasing Zr from 0 to 0.6, while c oscillates around 4.759 Å. The unit cell contraction comes with a 0.7% of volume reduction when x goes from 0 to 0.6. The contraction of a was recently observed in the $Sm_{1-y}Zr_y(Fe_{0.8}Co_{0.2})_{11.5}Ti_{0.5}$ ($0 \leq y \leq 0.3$) alloys reported by Tozman et al. [87].

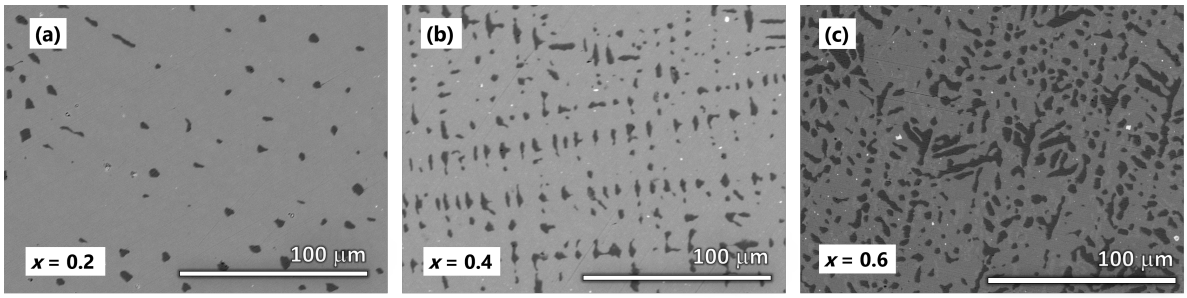

Figure 3.15: BSE-SEM of optimally annealed $Sm_{1-x}Zr_xFe_{11}V$ alloys (a) $x = 0.2$ (b) $x = 0.4$ and (c) $x = 0.6$.

Figure 3.15 shows BSE-SEM micrographs of the annealed alloys $x = 0.2, 0.4, 0.6$. After the annealing, narrow dendrites of α-(Fe,V) between 5 and 20 μm are formed and uniformly distributed, the matrix phase is identified as the 1:12, and the light gray areas as the $ZrFe_2$ Laves phase, this last phase is only visible for $x = 0.6$. A SEM micrograph and an EDX elemental mapping for $x = 0.6$ is shown in Fig. 3.16. From the mixed map, is clear the segregation of the α-(FeV) and the $ZrFe_2$ phases, the former are represented by the green-red dendrites and the latter by the blue-green's. The chemical composition of the 1:12 compounds determined by EDX are listed in the Table 3.9.

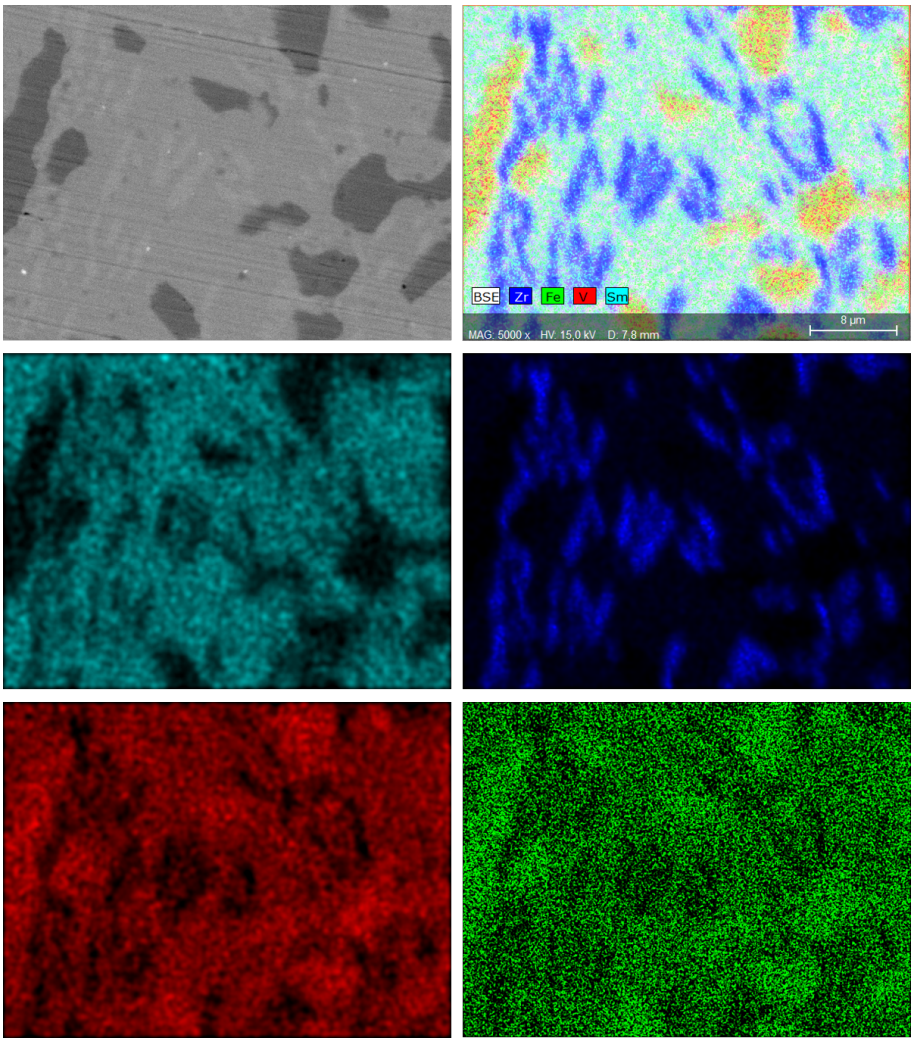

Figure 3.16: SEM and EDX composition images of Sm, Zr, V and Fe elements on the polished surface of the optimally heat treated $Sm_{1-x}Zr_xFe_{11}V$ ($X = 0.6$) alloy.

3.3.2 Magnetic Properties

Thermomagnetic scans, which are presented in Fig. 3.17 confirm that the 1:12 phase is not the only magnetic phase present, but there is also some $ZrFe_2$, and its volume fraction becomes more evident as Zr content increases. $ZrFe_2$ is a ferromagnetic phase of large Fe magnetic moment, $B_{\rm hf}$ and high $T_{\rm C}$. In the literature, Brückner et al. found that $T_{\rm C}$ increases from 337 to 525°C as the Fe content increases [115]. In this case, the $T_{\rm C}$ for x = 0.4 and 0.6 is 436 and 424°C, respectively. On the other hand, the $T_{\rm C}$ of 1:12 phase decreases from 361 to 310°C with the Zr substitution from $x = 0$ to 0.6, respectively. The $T_{\rm C}$ values found are consistent with the phases observed from the XRD patterns.

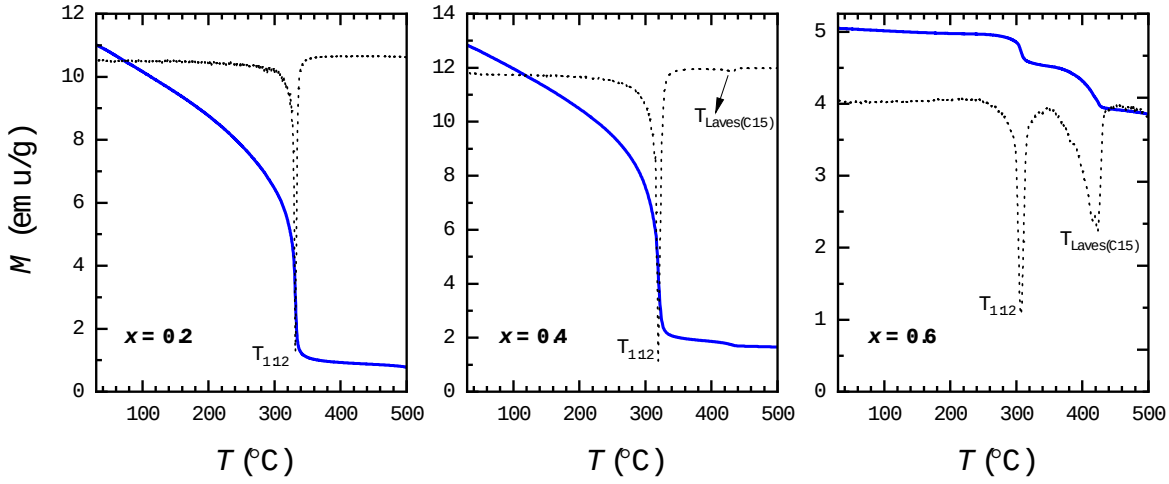

Figure 3.17: $T_{\rm C}$ of optimally annealed $Sm_{1-x}Zr_xFe_{11}V$ alloys.

Figure 3.18 shows the room temperature magnetization curves of the oriented powders of $Sm_{1-x}Zr_xFe_{11}V$ alloys measured $\parallel$ and $\perp$ to the orientation direction. They are arranged in order of increasing Zr content, x. On the right side, the XRD patterns of the oriented powders are shown. The $M_{\rm s}$ values for the 1:12 phase were deduced by subtracting the contribution from the secondary phases taking into account their volume fractions. The $M_{\rm s}$ value at room temperature rises from 115 to 138 Am^2/kg with increasing x from x = 0.0 to 0.6.

The $\mu_0 H_{\rm A}$ was determined in the same way as described in section 3.2.3, by plotting M in the perpendicular direction as a function of $[(\mu_0 H)^{-2}]$, and the minima of the derivative was taken as $\mu_0 H_{\rm A}$. Table 3.9 summarizes the intrinsic magnetic properties together with the

chemical composition of the compounds determined by EDX. As Zr content is increased, the $\mu_0 H_A$ decreases from 11.1 T for x = 0.0 to 8.8 T for x = 0.6, which means that even for highest Zr content the $\mu_0 H_A$ value is reasonably high. In accordance with the anisotropy field, XRD measurements of field oriented powder samples indicate that the easy magnetization direction is along (002) c-axis. The other reflexions like (321), (202) are attributed to the presence of the secondary phases or misoriented grains.

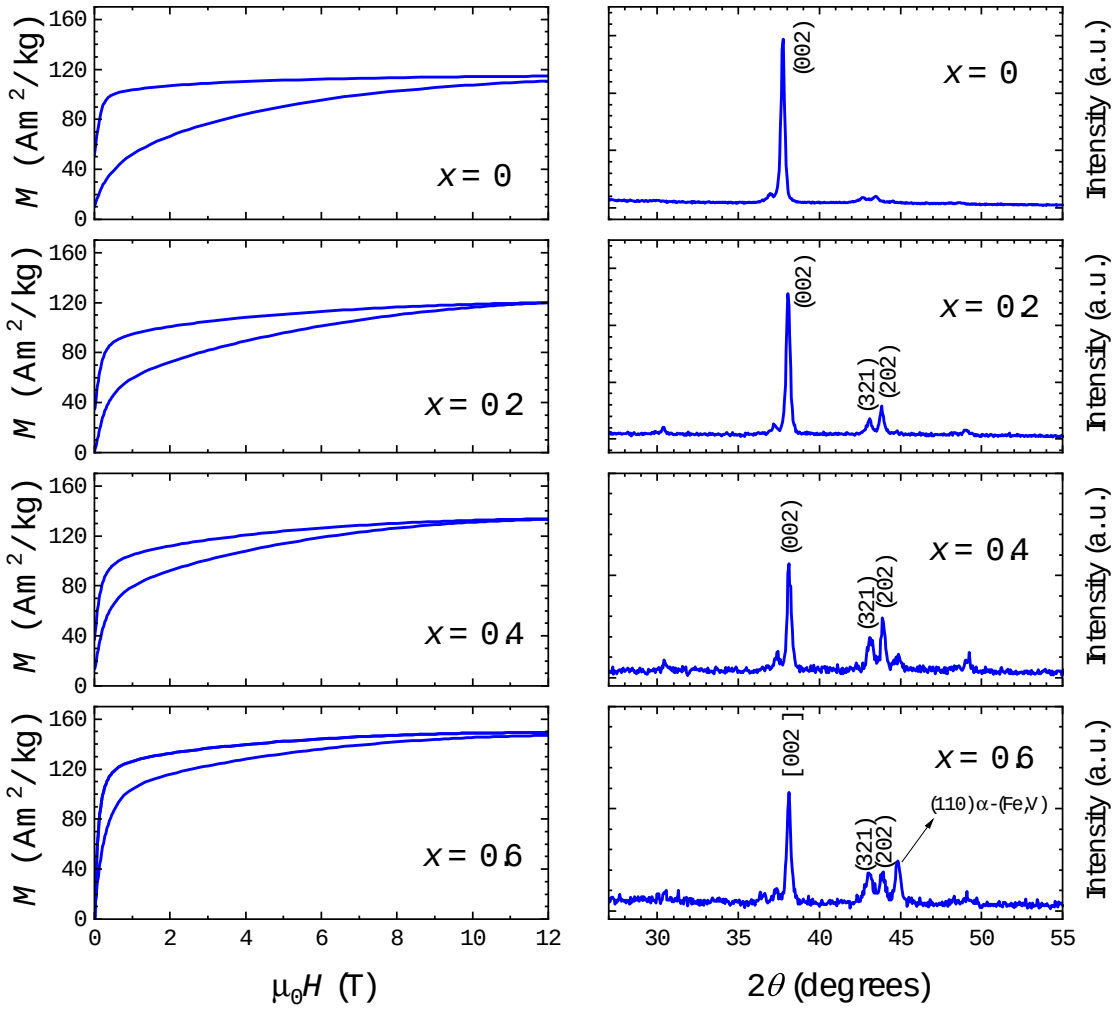

Figure 3.18: (Left) Magnetization curves measured on oriented samples of $Sm_{1-x}Zr_xFe_{11}V$ alloys. (Right) XRD data of oriented samples of $Sm_{1-x}Zr_xFe_{11}V$ alloys.

All the magnetization curves measured in direction $\perp$ to the orientation have a curvature

in the low-field portion. This can be due to the combination of two effects, the presence of a soft phase of high susceptibility α-(Fe,V), and poor alignment, as the < 38 μm particles in the powder samples are certainly not all single crystals and also have irregular external shapes that prevent their perfect alignment. The demagnetization factor of the aligned powders was considered negligible as the $\mu_0 H_A$ was large enough.

Table 3.9: Intrinsic magnetic properties of the 1:12 phase in $Sm_{1-x}Zr_xFe_{11}V$ alloys.

x	Composition	M_s (Am^2/kg)	$\mu_0 H_A$ (T)	T_C (°C)
0.2	$Sm_{0.77}Zr_{0.20}Fe_{10.98}V_{1.05}$	115	9.8	335
0.4	$Sm_{0.61}Zr_{0.40}Fe_{11.03}V_{0.96}$	129	9.2	324
0.6	$Sm_{0.40}Zr_{0.60}Fe_{11.02}V_{0.98}$	138	8.8	310

3.4 Summary and conclusions

In this chapter the intrinsic properties of different Sm-based 1:12 systems were studied both in ribbons and bulk.

In the first section, a series of melt-spun ribbons of $(Sm_{1-x}Ce_x)Fe_9Co_2Ti$ (x = 0.0, 0.25, 0.50, 0.75, 1.0) were studied by Mössbauer spectroscopy. Here, it was possible to establish the highly disordered character of the as-spun ribbons. The B_{hf} showed broad distributions centered around 10 T and 21 T. Mössbauer analysis on heat-treated ribbons allowed to identify the different magnetic responses of the Fe located in the $8i$, $8j$ and $8f$ sites. Analysis on the spectra indicated a redistribution of Co in the $8f$ and $8j$ sites as the Sm was replaced by Ce. For $x \leq 0.5$ the occupation percentage was 70/30 ($8j/8f$), whereas for $x > 0.5$ was 50/50. This coincided with the decreasing of the B_{hf} in the $8j$ site whereas $8f$ was increased. The δ also showed variations for Ce concentrations above 0.5. When the redistribution of Co in the $8j$ and $8f$ sites was 50/50, coincided with the constant behaviour of the H_A.

In order to obtain the $SmFe_{12-x}V_x$ alloys with V content smaller than reported earlier [59, 34, 91], the phases and magnetic properties in the alloys with x varying from 0.5 to 2.0 were studied both experimental and theoretically. The alloys were prepared by arc-melting followed by homogenization at temperatures in the range of 900-1100°C for 1 to 3 days. After the appropriate homogenization, apart from the sample with x = 0.5, the main phase identified was the $ThMn_{12}$

structure, with a very low α-(Fe,V) around 0.5-1%. The volume of the structure slightly reduced with the decrease of the V concentration. A strong peak (002) in the X-ray diffraction patterns was observed for the oriented powders, confirming a uniaxial magnetocrystalline anisotropy. The theoretical results are consistent with the experimental. The reduction of x from 2 to 1, increased the T_{C} from 321 to 361°C, M_{s} from 83 to 115 $\mathrm{Am^2/kg}$ and $\mu_0 H_{\mathrm{A}}$ from 9.8 to 11 T. Regarding the Mössbauer measurements, the decrease of V content from 2 to 1, increased the $\langle B_{\mathrm{hf}} \rangle$ from 21 to 25 T, whereas the $\langle \delta \rangle$ decreased from -0.08 to -0.15 mm/s. The study suggests that the family of $\mathrm{SmFe_{12-x}V_x}$ (x = 1.0, 1.5, 2.0) compounds are good candidates for permanent magnets applications. In particular, the newly synthesized $\mathrm{SmFe_{11}V}$ compound showed superior magnetic properties.

In the last section, substitution of Zr for Sm in $\mathrm{Sm_{1-x}Zr_xFe_{11}V}$ ($0 \leq x \leq 0.6$) was studied in order to analyze the evolution of the magnetic and structural properties with a non rare-earth element. For all the samples optimally annealed, the major phase was the 1:12 phase, followed by α-(Fe,V) and the laves ($\mathrm{MgCu_2}$) $\mathrm{ZrFe_2}$ phase. For high concentrations of Zr there was segregation of Zr and Fe and hence $\mathrm{ZrFe_2}$ was formed. The Laves phase was detected for x = 0.4 and 0.6, with T_{C} of 436 and 424°C, respectively. The formation of α-(Fe,V) increased with the Zr content. The substitution of Zr resulted in a contraction of 0.7% of the 1:12 cell volume. The lattice constant a decreased monotonically from 8.509 to 8.482 Å with increasing Zr from 0 to 0.6, while c oscillated around 4.759 Å. Oriented powder XRD measurements indicated that the easy magnetization direction was along (002) c-axis. As Zr content increased from x = 0.0 to 0.6, the $\mu_0 H_{\mathrm{A}}$ decreased from 11 to 8.8 T and the T_{C} from 361 to 310°C. On the other hand, the M_{s} increased from 115 to 138 $\mathrm{Am^2/kg}$.

Chapter 4

Development of coercivity

4.1 Introduction

Having a material with good intrinsic magnetic properties do not guarantee a good hard magnet, however can be considered as a starting point to process one. Transferring the intrinsic properties into extrinsic properties requires an appropriate processing, and it is a complex task. The development of coercivity in an uniaxial ferromagnetic $4f$-$3d$ compounds is achieved through refinement of the grains. In practice, for permanent magnet manufacturing, this refinement typically involves rapid solidification or powder metallurgy. Although the former had been proven to work for the $ThMn_{12}$-type alloys [116, 117, 94], only powder metallurgy is really suitable in the production of permanent magnets industrially. Mainly, because of its cost effectiveness [118] (mass production ability, low energy consumption and minimum number of steps) and the possibility of being able to control the density, particle size and microstructure.

This chapter presents different approaches to develop coercivity in Sm-Fe-V based alloys with $ThMn_{12}$ structure (hereafter 1:12), such as grain size reduction by mechanical milling, bulk hardening by intergrain boundary phases, and amorphization induced by mechanical milling and melt-spinning and subsequent recrystallization of the hard 1:12 phase upon appropriate heat treatments.

4.2 Grain size reduction by mechanical milling

The starting stoichiometric $SmFe_{10}V_2$ alloy was prepared by arc melting followed by homogenization for 2 days at 1000°C, as it was determined in chapter 3. The heat-treated alloys were crushed into particles of diameter less than < 300 μ, after removing the impurities of the ingots surface. The powders were sealed into a hardened steel vial with several steel balls of 12, 8, 5.5 and 4 mm in the ratio of powder to ball of 1 to 20 in hexane, to protect from oxidation. The powder was high energy ball-milled from 2 min to 4 h. After the milling, the powder was washed with ethanol and dried in a vacuum chamber. For heat treatment, the powder was pressed into cylinders of 5×3 mm in diameter and height, respectively, and sealed in Ar-filled quartz ampoules. The samples were sintered at temperatures ranging from 450 to 1000°C for 20 and 40 min, followed by quenching in water.

4.2.1 Structural and magnetic properties

Figure 4.1(a) presents the XRD patterns of the as-milled powder milled for different times. The XRD patterns of the starting powder show diffraction peaks corresponding to the 1:12 phase and a very low fraction ($< 2\%$) of α-(Fe,V). After 30 min milling, XRD peaks broaden but still the starting alloy patterns remain unchanged. As the milling time increases, there is a slow decomposition into the metastable $TbCu_7$-type (hereafter 1:7) structure and α-(Fe,V) phases. After 4 h of milling the transformation into the 1:7 structure is complete (some reflections of 1:12 phase, for instance the [3 1 0] disappear).

During milling the intensity of the reflections decreases gradually and all peaks become broader with increasing milling time, indicating that a large number of defects and dislocations are formed during the milling. Also the broadened diffraction peaks indicate a finer grain size.

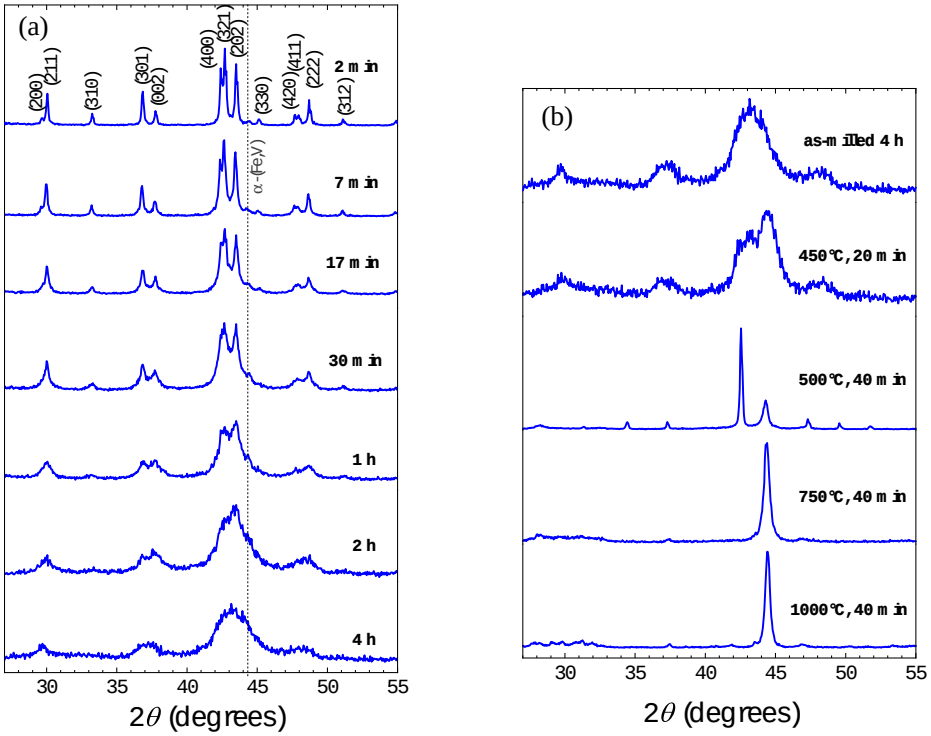

Figure 4.1: X-ray diffraction patterns of $SmFe_{10}V_2$ (a) as-milled powder with different milling times (b) 4 h milled powder annealed at 450, 500, 750 and 1000°C for 40 and 20 min.

It is worth noting that the 1:7 structure has been considered as a precursor of some 1:12 alloys when the intermetallic compounds is prepared by melt-spinning, mechanical alloying or mechanical milling. The formation of the hexagonal 1:7 structure was reported before in Nd-Fe-Ti [119, 120] and Sm-Fe-Ti [121] alloys, prepared by mechanical alloying and subsequent annealing at temperatures ranging from 600 and 850°C respectively. In $NdFe_{11}Ti$ alloy, Tang [122] reported the decomposition of $Nd(Fe,Ti)_{12}$ to $Nd(Fe,Ti)_7$ and α-Fe(Ti) solid solution on mechanical milling. For longer times of 5h milling, it was observed a transformation to an amorphous phase and a supersaturated bcc solid solution of Ti in Fe.

Although it was reported that increasing the annealing temperature promoted the transformation of 1:7 to 1:12 phase, in our case after heat-treating the 4 h milled powder, at temperatures ranging from 450 to 1000°C (see Fig. 4.1(b)), the 1:12 could not be formed. In contrast, there is a crystallization to an unknown phase at 500°C, and at higher temperatures,

only the precipitation of α-(Fe,V) phase occurs.

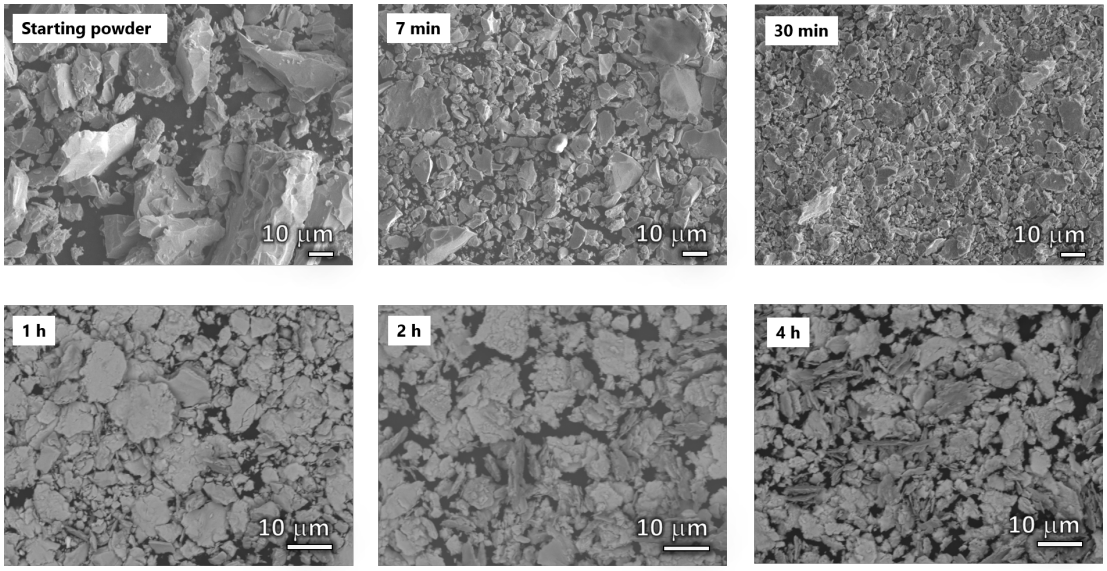

Figure 4.2: SEM Secondary electron micrographs of the $SmFe_{10}V_2$ powder milled at different times.

The SEM secondary electrons images in Fig. 4.2 shows morphology of the $SmFe_{10}V_2$ powders milled up to 4 hours. In the first hour, the as-milled particles with sharp edges evolve into faceted particles. After 1 h, flakes start to form and by 4 hours they become more evident. The average particle size decreases with the increase in milling time, going from 30 to 8.8 µm during the first 30 min, however the size is not uniform throughout. There are bigger particles which have not been milled properly. For longer milling time, the particles are more homogeneous and although the morphology changes, the average size is approximately the same. After milling for 4 h, the average flake size is ranging from 2 to 10 µm with thickness from 0.2 to 0.5 µm.

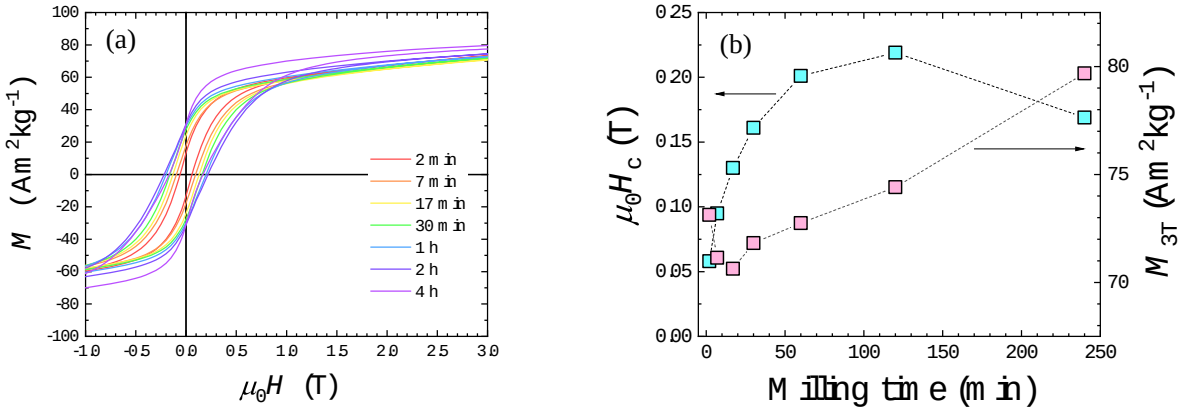

Figure 4.3: (a) Demagnetization curves of the $SmFe_{10}V_2$ powder with different milling times (b) Variation of coercivity and magnetization at 3 T with milling time.

Figure 4.3(a) shows the demagnetization curves of $SmFe_{10}V_2$ powders milled for different times. The $\mu_0 H_c$ value increased from 0.06 T in the starting powder to reaching a maximum of 0.21 T. This increase of $\mu_0 H_c$ may be attributed to the grain size reduction and residual stress. Milling for more than 2 h or more, results in decrease of $\mu_0 H_c$ value which may be attributed to the low anisotropy of the 1:7 structure as observed from XRD in Fig. 4.1(a).

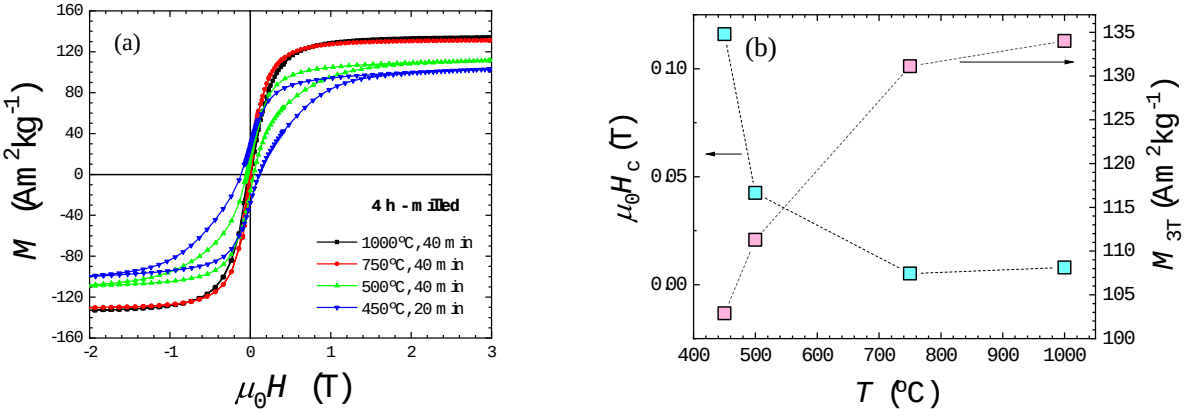

Figure 4.4: (a) Demagnetization curves of the 4 h milled powder heat treated at 450, 500, 750 and 1000°C for 40 and 20 min (b) Variation of coercivity and magnetization at 3 T applied field with temperature.

The 4 h hour milled powder was selected to do different heat treatments at temperatures between 450 and 1000 °C, as the 1:7 structure was completely formed in this powder. From Fig. 4.4(b) can be seen that the $\mu_0 H_c$ decreased and M_{3T} value increases after annealing as it was expected due to the formation of the α-(Fe,V) soft phase. The increase of α-(Fe,V) after annealing results from the Sm evaporation, due to its high vapor pressure and enthalpy of vaporization (see Appendix C).

4.3 Bulk hardening by intergrain boundary phases

One of the alternatives for manufacturing functional magnets, different to the sintering and rapid solidification, is via recrystallization of regularly cast ingots. If formation of the hard magnetic phase is initially suppressed, subsequent heat treatment can be tuned to ensure that the phase crystallizes with the proper microstructure. The only known $R(Fe,M)_{12}$ alloy susceptible to the bulk hardening is the $Sm(Fe,V)_{12}$; it solidifies into a mixture of the α-(Fe,V) and $SmFe_2$ (hereafter 1:2) phases and, after controlled crystallization of the $SmFe_{10}V_2$ phase, develops a $\mu_0 H_c$ value up to 3.7 kOe [123].

One of the strategies to enhance the $\mu_0 H_c$ value by bulk magnetic hardening is, in a similar way to the Alnico magnets. In these magnets, the magnetic hardness originates from the shape anisotropy of FeCo-rich magnetic rods (α_1 phase) which are embedded in a non-magnetic NiAl-rich matrix (α_2 phase). Lanthanum is the only element among the R not forming binary compounds with Fe, and it was also shown to avoid the 1:12 structures [73]. It is, therefore, conceivable that addition of La to $R(Fe,M)_{12}$ alloys will lead to a composite of the $R(Fe,M)_{12}$ and La phases, thus facilitating the development of $\mu_0 H_c$ value through heat treatment. To test this hypothesis, an alloy of $Sm_{0.12}Fe_{0.75}V_{0.13})_{98}La_2$ was prepared by arc melting and homogenized for 10 to 20 h at temperatures 700-800°C.

The XRD patterns shown in Fig. 4.5 reveal that the as-cast alloy is composed of five phases: $Sm(Fe,V)_{12}$ (tetragonal, $I4/mmm$), $SmFe_2$ (cubic, $Im\bar{3}m$), α-(Fe,V) (cubic, $Im\bar{3}m$), Sm_3La (hexagonal, $P6_3/mmc$) and Sm (hexagonal, $P6_3/mmc$). The lattice parameters and *vol.*% are listed in table 4.1.

The $SmFe_2$ Laves phase has a cubic $MgCu_2$-type (C15) structure with space group of $Fd\bar{3}m$ (No. 227) [124, 125]. In this structure, the Sm atoms occupy the $8a$ sites, and Fe atoms the $16d$

sites. It was reported that $SmFe_2$ is ferromagnetic at room temperature (T_C = 688 K) and its saturation moment is 2.68 μ_B/mol (57.1 emu/g) [23, 125].

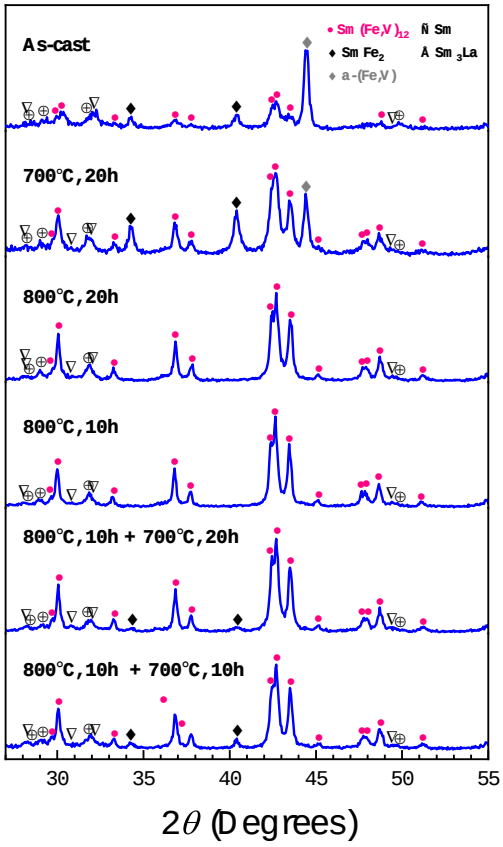

Figure 4.5: The XRD patterns of $(Sm_{0.12}Fe_{0.75}V_{0.13})_{98}La_2$ alloy in as-cast state and after heat treatment at 700°C for 20 h, 800°C for 20 h, 800°C for 10 h, 800°C for 10 h + 700°C for 20 h, 800°C for 10 h + 700°C for 10 h.

The heat-treated sample at 700°C for 20 h shows an increase of 1:12 and 1:2 *vol.*%, and a decrease of α-(Fe,V). The contribution of the α-(Fe,V) becomes neglible (< 1%) or zero, for the heat-treated samples at 800°C. Combination of different heat treatments 800°C for 10 h + 700°C for 20 h, 800°C for 10 h + 700°C for 10 h allow to suppress the α-(Fe,V) and to retain the 1:2 phase. In all heat-treated samples the 1:12 phase exists as the major phase. On the other hand, the Sm and Sm_3La are still present after heat treatment, however in most cases, their *vol.*% decrease in a 40%.

According to previous reports, at ambient conditions Sm normally assumes a rhombohedral structure (α-form) [126, 127]. Upon heating to 731°C, its crystal symmetry changes into hcp, although this transition temperature has been found to be dependent on the metal purity [128]. Further heating to 917°C transforms the metal into a bcc phase. Heating to 300°C combined with compression to 40 kbar results in a dhcp structure [129, 130]. The dhcp phase could be also produced without compression, using a non-equilibrium annealing regime with a rapid temperature change between 400 and 900° [131].

Table 4.1: Lattice parameters and volume fractions of different phases, present in the $Sm_{0.12}Fe_{0.75}V_{0.13})_{98}La_2$ alloy in as-cast state and after heat treatment at different conditions, derived from Rietveld analysis.

Sample	$a_{1:12} \pm \Delta a_{1:12}$	$c_{1:12} \pm \Delta c_{1:12}$	$V_{1:12}$	$V_{1:2}$	$V_{\alpha-(Fe,V)}$	V_{Sm}	V_{Sm_3La}
As cast	8.521 ± 0.004	4.781 ± 0.003	57.5	5.7	30.1	5.3	1.4
700/20h	8.499 ± 0.001	4.757 ± 0.001	69.1	13.5	14.0	2.2	1.2
800/20h	8.517 ± 0.001	4.763 ± 0.001	95.4	0.0	0.0	4.2	0.5
800/10h	8.516 ± 0.001	4.765 ± 0.001	94.9	0.0	0.8	3.7	0.6
800/10h - 700/20h	8.522 ± 0.002	4.767 ± 0.001	95.7	1.0	0.0	2.1	1.3
800/10h - 700/10h	8.522 ± 0.002	4.767 ± 0.001	94.8	1.9	0.0	2.9	0.5

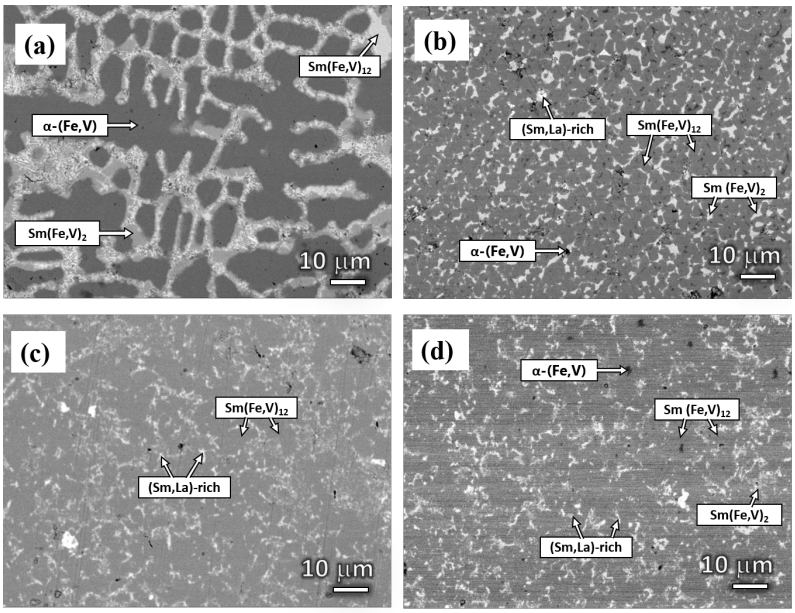

Figure 4.6: The SEM-BSE micrographs of $(Sm_{0.12}Fe_{0.75}V_{0.13})_{98}La_2$ alloy: (a) as-cast and heat-treated alloys at (b) 700°C for 20 h (c) 800°C for 20 h (d) 800 for 10 h + 700°C for 10 h.

Figure 4.6 shows the SEM-BSE microstructures images of as-cast alloy and after heat treatment at 800°C for 20 h, 700°C for 20 h and 800 for 10 h + 700°C for 10 h. The EDX compositional analysis of the alloys reveals that the as-cast ingot consists mostly of α-(Fe,V), 1:2, a small amount of 1:12, Sm and Sm_3La phases. The brighter regions correspond to the Sm and Sm_3La phases. Annealed alloys develop a microstructure consisting of 1:12 grains surrounded by either La (or La-Sm)-rich (at 800°C) or 1:2 (at 700°C). The grain size of heat-treated alloy at 700°C is around 3-6 μm, but in the alloy annealed at 800°C, grain growth occurs and becomes 8-15 μm.

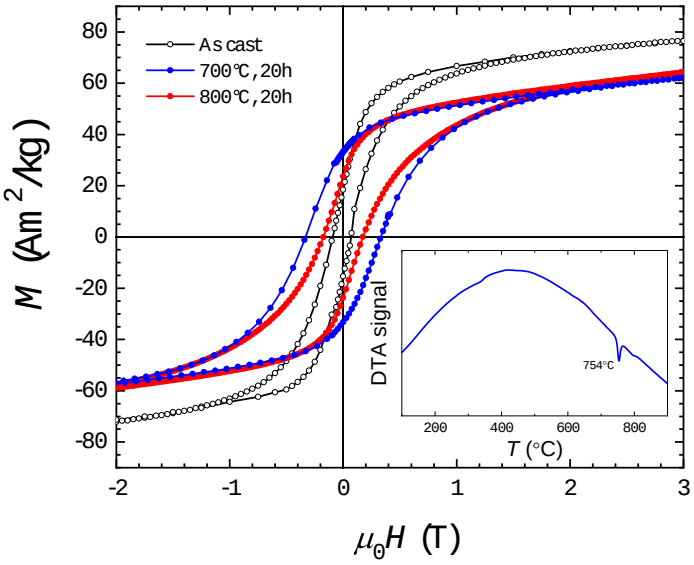

Figure 4.7: Room-temperature hysteresis loops of $(Sm_{0.12}Fe_{0.75}V_{0.13})_{98}La_2$ alloy: as-cast, heat-treated at 800°C and 700°C for 20 h. Inset: DTA scan of heat-treated alloy at 700°C for 20 h.

Table 4.2: Magnetic properties, M_{3T}, M_r and $\mu_0 H_c$ of $(Sm_{0.12}Fe_{0.75}V_{0.13})_{98}La_2$ as-cast and heat-treated alloys extracted from the hysteresis loops in Fig. 4.7.

Sample	M_{3T} (T)	M_r (Am^2/kg)	$\mu_0 H_c$ (Am^2/kg)
As-cast	77	18	0.09
700/20h	62	33	0.33
800/20h	64	24	0.18
800/10h	66	30	0.21
800/10h - 700/20h	64	32	0.26
800/10h - 700/10h	66	31	0.22

Figure 4.7 shows the hysteresis loops of $(Sm_{0.12}Fe_{0.75}V_{0.13})_{98}La_2$ as-cast and heat-treated alloys at 800 and 700°C for 20 h measured by applying a maximum field of 3 T. The as-cast alloy shows a M_{3T}, M_r and $\mu_0 H_c$ values of 77 Am^2/kg, 18 Am^2/kg and 0.09 T, respectively. After annealing at 700°C, the values of M_r and $\mu_0 H_c$ increases to 33 Am^2/kg and 0.33 T,

respectively, and M_{3T} decreases to 62 Am^2/kg. Increasing the heat treatment temperature decreases the value of $\mu_0 H_c$ without significantly affecting the M_{3T} and M_r values. Table 4.2 lists the M_{3T}, M_r and $\mu_0 H_c$ values obtained from the hysteresis loops (Fig. 4.7) along with the values for the rest of the samples. The heat-treated alloy at 700°C exhibiting high $\mu_0 H_c$ of $0.33T$ has the smallest *vol.*% of 1:12 phase (69.1%) and the maximum of 1:2 phase (13.5%) compared to the rest of the annealed alloys.

The M_{3T} does not change significantly with the heat treatment conditions above 800°C as the 4 samples contain almost same *vol.*% of the 1:12 phase($\approx$ 95%). Despite containing smallest *vol.*% of 1:12 phase, the heat-treated alloy at (700°C for 20 h) shows M_{3T} value very close to other annealed samples, this is because of important contribution of α-(Fe,V). The best results achieved were: $\mu_0 M_r$ = 0.37 T, $\mu_0 H_c$ = 3.3 T, $(BH)_{max}$ = 33.7 kJm^{-3}(4.24 MGOe).

The DTA thermogram of the heat-treated alloy at 700°C for 20 h (see Fig. 4.7, inset) reveals a probable eutectic reaction involving the La-Sm phase at 753°C (in the binary alloy systems, the eutectic reaction between La and Fe occurs at 770°C, and the one between Sm and $SmFe_2$ at 720°C). The same eutectic reaction was observed in the heat-treated alloy at 800°C for 20 h. These results suggest that the $\mu_0 H_c$ value is not developing because La addition, but because the combination of other effects, like the grain size and the ratio of 1:12 and 1:2 phases. Shultz et al. reported the presence of 1:2 phase in $Sm_{15}Fe_{70}V_{15}$ alloy prepared by mechanical alloying followed by a heat treatment at 700°C for 30 min. They reported a $\mu_0 H_c$ value of 1.12 T [132].

4.4 Mechanical milling: amorphization and crystallization of off-stoichiometric alloys

As shown in the section 4.2, one of the obstacles to get the 1:12 phase, and hence the $\mu_0 H_c$ value, in the $Sm(Fe,M)_{12}$ alloy system is the Sm losses that occur throughout the processing. In order to compensate the Sm losses, off-stoichoiometric Sm-Fe-V alloys, with nominal composition of $Sm_{12}Fe_{73}V_{15}$ equivalent to $SmFe_{10}V_2$, were prepared and processed to get powder with reasonable $\mu_0 H_c$ value. The method consisted of preparing the master alloy with 1:12 phase, followed by its amorphization by means of mechanical milling, and lastly the crystallization of the nano sized grains of 1:12 phase through short heat tratment. Figure 4.8 illustrates the different stages followed.

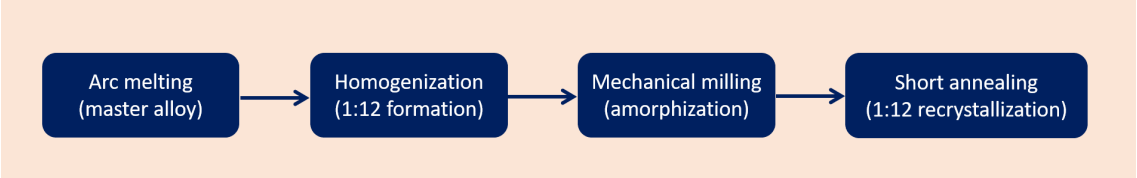

Figure 4.8: Processing flow diagram

Alloys with nominal composition of $Sm_{12}Fe_{73}V_{15}$ were prepared by arc-melting the pure elements Sm (pieces 99.9%), Fe (pieces 99.97%) and V (sheets 99.7%) under Ar atmosphere. The ingots were heat-treated in Ar to maximize the volume fraction of the 1:12 phase at 800°C for 20 h and quenched in water. The ingots were crushed in a hardened steel mortar to obtain powders with particle size < 300 μm. The powders were milled for 10 h under Ar atmosphere in a SPEX mill unit using a custom-made hardened steel vial equipped with a vacuum valve. Steel balls of 12, 8, 5 and 4 mm diameter and a ball to powder to balls mass of 1:20 was used. The powders were sealed in Ar-filled quartz ampoules and subsequently annealed in the temperature range of 600-800°C for 15-45 min.

4.4.1 Homogenized alloy

Figure 4.9 shows the XRD pattern of $Sm_{12}Fe_{73}V_{15}$ alloy annealed at 800°C for 20 h. The homogenized alloy shows reflections from $Sm(Fe,V)_{12}$ (estimated 83.1 *vol.*%), $SmFe_2$ (14.7%), Sm (1.5%) and an almost undetectable α-(Fe,V) phase (0.8%). The lattice parameters obtained by Rietvelt analysis are given in the same figure. In contrast with the stoichiometric alloys (section 4.2), the Sm excess results in the formation of 1:2 phase and the segregation of metallic Sm, both from the same nature than the previous section.

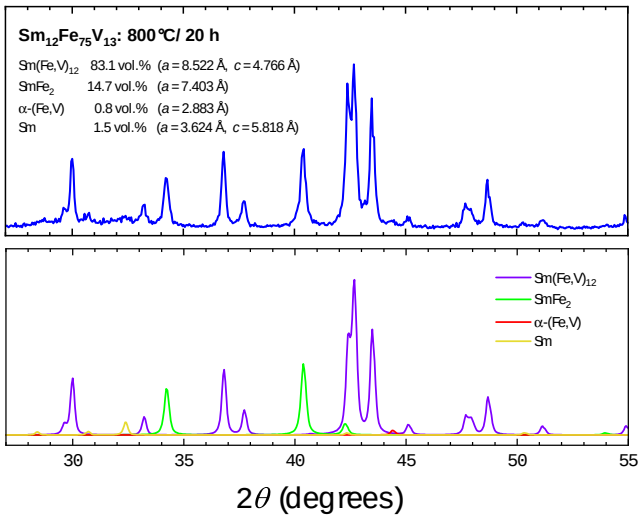

Figure 4.9: (Top) X-ray diffraction pattern of $Sm_{12}Fe_{73}V_{15}$ homogenized at 800°C for 20 h. (Bottom) computed phases from the Rietvelt analysis.

The microstructure of the as-cast sample reveals coarse α-(Fe,V) regions with a dendritic morphology surrounded by small 1:2 grains of 0.1-1 μm. The matrix and brighter regions were detected to be the 1:12 and Sm phases, respectively. As expected, from the XRD results, the predominant phase in the homogenized microstructure is the 1:12 (Fig. 4.10(b)) with small grains of about 1 μm (see the inset of Fig. 4.10). In this case, the matrix and the minor brighter regions are identified to be $SmFe_2$ and Sm phases, respectively. The morphologies indicate that the solidification sequence for the major phase is from α-(Fe,V) to 1:12.

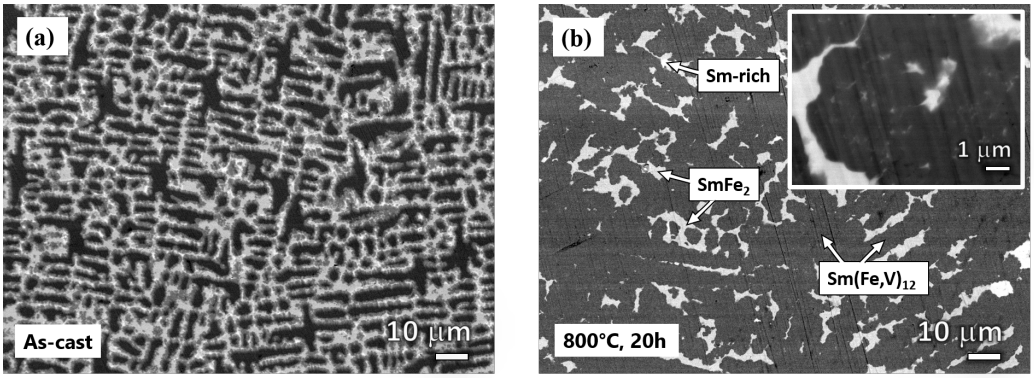

Figure 4.10: SEM-BSE images of $Sm_{12}Fe_{73}V_{15}$ alloy: (a) As-cast (b) homogenized at 800°C for 20 h

4.4.2 Mechanical milling and $Sm(Fe,V)_{12}$ crystallization

After 10 h of milling, the particle size is quite homogeneous and is found to be (3.1 ± 0.4) μm as shown in Fig. 4.11(a). The XRD pattern of the as-milled powder shown in Fig. 4.11(b), depicts a strong broad peak around 44.3° along with an almost negligible broad halo peak. No peaks corresponding to 1:12 and 1:2 phases are present. This indicates the formation of an amorphous phase coexisting with an α-(Fe,V) phase. The small shift from the pure α-Fe diffraction angle ($2\theta = 44.7$°C) suggests a lattice expansion, this is a result from the solid solution of V atoms in the Fe-based bcc lattice. In contrast with the milling of the stoichiometric alloy (section 4.2), it seems that milling in hexane does not facilitate the amorphization of this alloy, and it is more convenient the use of Ar.

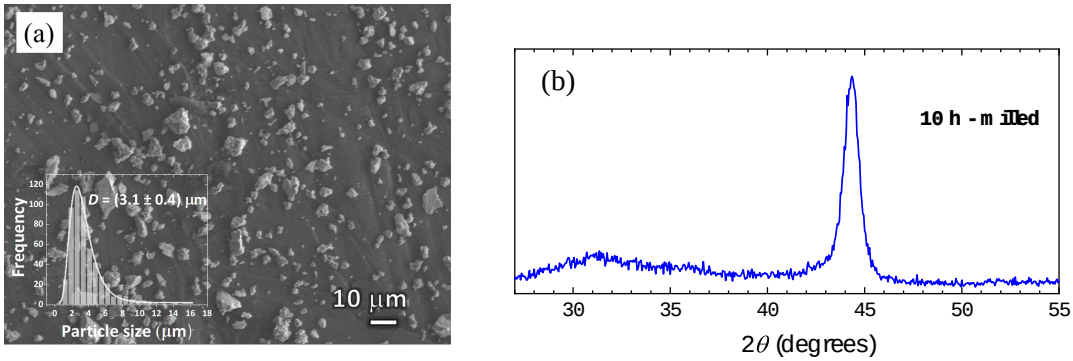

Figure 4.11: The $Sm_{12}Fe_{73}V$ 10 h milled powder (a) SEM secondary electrons-image (b) XRD pattern

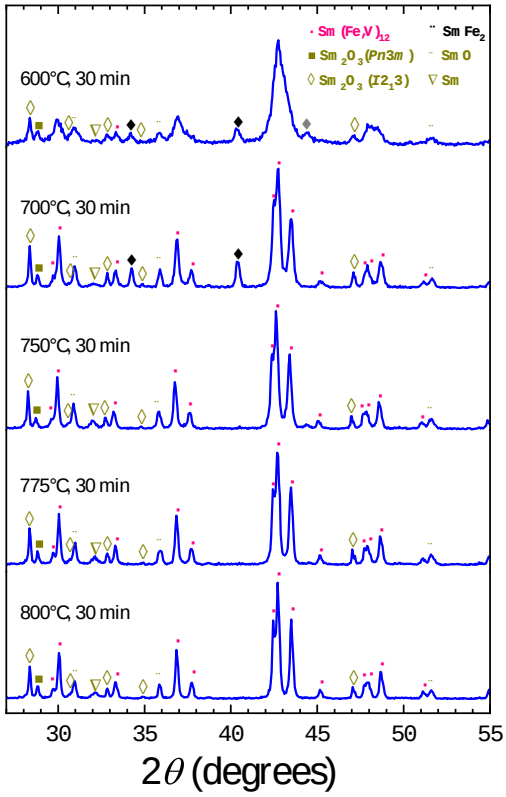

Figure 4.12: X-ray diffraction patterns of as-milled $Sm_{12}Fe_{73}V$ powder annealed at indicated temperatures.

Figure 4.12 shows the XRD patterns of 10 h mechanically milled $Sm_{12}Fe_{73}V_{15}$ sample, heat-treated at temperatures between 600 and 800°C for 30 min. As it is noted, at 600°C broad peaks corresponding to the $Sm(Fe,V)_{12}$ starts to appear and it is completely formed at 700°C. With further increase in the temperature, the 1:12 peaks becomes sharper, as an effect of the cristallite size growth. For all the heat-treated samples, the additional peaks were identified as $SmFe_2$, Sm and Sm-oxides. In particular, 1:2 is present at 600°C, and the *vol.*% increases from 3 to 6% at 700°C. For temperatures above 700°C, the 1:2 phase decomposes, resulting in a Sm segregation, and hence a higher *vol.*% of the 1:12. All the heat-treated samples contain at least 3 different Sm-oxides, SmO (cubic face-centered, space group $Fm3m$) and the sesquioxides Sm_3O_2 (cubic, space group $I2_13$) and Sm_2O_3 (cubic, space group $Pn\bar{3}m$).

It appears that the all Sm-oxides are formed as a direct consequence of the annealing of the very fine powders (≈ 3 μm). In previous investigations from other authors, SmO was formed when a small sliver of Sm metal was heat-treated to 626°C for 15 min in an evacuated vitreous silica capillary [126]. On the other hand, Sm_2O_3 (bixbyite structure $I2_13$) was identified by Goldschmith et al.[133] by using temperatures ranging 600-750°C. In our case, the Sm-oxides physically could be observed as a coating formed in the tube walls during the annealing as shown in Fig. 4.13.

Figure 4.13: Appearance of the tubes after the heat treatment.

The hysteresis loops of $Sm_{12}Fe_{73}V$ 10 h mechanically milled powders and heat-treated at 600, 700, 750, 775 and 800°C for 30 min are illustrated in Fig. 4.14(a). The homogenized sample (not shown here) has a $\mu_0 M_{3T}$ = 0.62 T (64 Am^2kg^{-1}) and $\mu_0 H_c$ = 0.09 T. After milling, the value of $\mu_0 M_r$ increases to 102 Am^2kg^{-1} and the $\mu_0 H_c$ was measured to be 0.02 T. The low value of $\mu_0 H_c$ is due to the absence of high-anisotropy 1:12 phase and the presence of large *vol.*% of the α-(Fe,V) solid solution. For low temperature 600°C, the annealing time is either not sufficient to form 1:12 or the grain size is too small for optimum $\mu_0 H_c$. At high temperatures, for instance 800°C and above, the $\mu_0 H_c$ value drops, due to coarsening of the crystallites. It is well established that the $\mu_0 H_c$ value decreases with increasing grain size, i.e., with increasing the temperature. The effect of temperature on $\mu_0 H_c$ value is shown in Fig. 4.14(b). Among the investigated temperatures, the optimal heat treatment was at 700°C for 30 min, with $\mu_0 H_c$ = 1.03 T, M_{3T} = 64 Am^2kg^{-1} and M_r = 42 Am^2kg^{-1}.

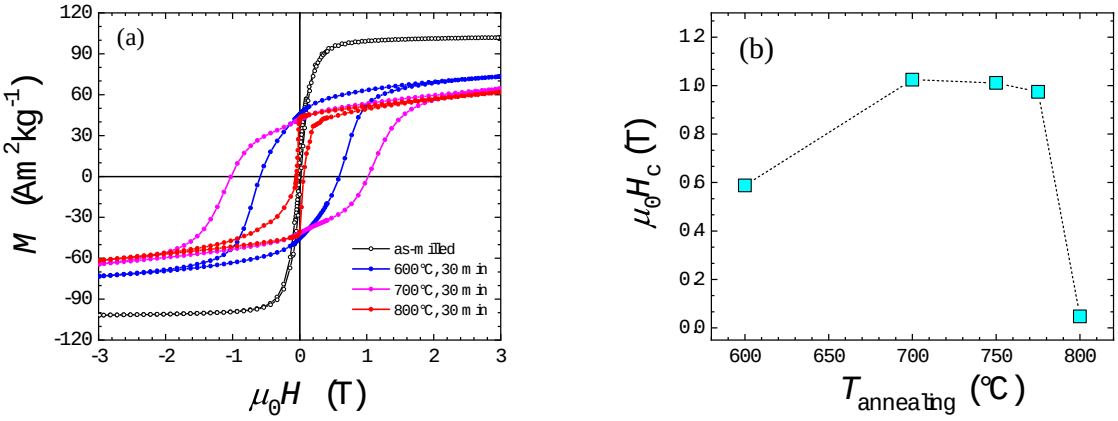

Figure 4.14: (a) Room-temperature hysteresis loops of as-milled $Sm_{12}Fe_{73}V_{15}$ powder and heat-treated at 600, 700 and 800°C (b) Dependence of the $\mu_0 H_c$ on the temperature for mechanically milled $Sm_{12}Fe_{73}V_{15}$ powder (heat-treated for 30 min)

4.4.3 Rapidly solidified ribbons

The process to obtain coercivity by using melt-spinning is very similar to the one used in mechanical milling. It started by making amorphous or nanocrystalline melt-spun ribbons of $Sm_{12}Fe_{73}V_{15}$ alloy, and then is subsequently heat-treated in order to crystallize or grow the hard phase.

Starting ingots of $Sm_{12}Fe_{73}V_{15}$ were made by arc melting the pure element in Ar atmosphere. The ingots were rapidly quenched by melt spinning the molten alloy through a 0.50 mm orifice onto the surface of Cu wheel rotating at a linear speed of 45 m/s. It has been reported that at high wheel speed (more than 35 m/s) a beginning amorphization is observed. The ribbons were ground and sieved using a 325 mesh (< 45 μm particle size) and sealed in quartz tubes under Ar. The ribbons were heat-treated at temperatures ranging from 600 to 900°C for 10-30 min followed by quenching into water.

Figure 4.15(a) shows a hysteresis loop of the ribbons optimally annealed at 700°C for 30 min. The ribbons exhibit a $\mu_0 M_{3T}$ = 89 Am^2kg^{-1}, $\mu_0 M_r$ = 59 Am^2kg^{-1} and $\mu_0 H_c$ = 0.96 T. The presence of α-(Fe,V) is reflected as a kink in the demagnetization curve. The amount of α-(Fe,V) depends on both the heat-treatment conditions and the chemical composition. It is

expected that harder magnetic properties can be obtained by varying the heat treatment as well as by adjusting the sample composition and particularly the amount of impurity elements. XRD measurements show the presence of the 1:12 structure in the heat-treated samples together with a low amount of α-(Fe,V). As in the case of mechanically milled alloys, the 1:12 is formed after crystallization of the amorphous Sm-Fe-V. The microstructure shown in Fig. 4.15(b) shows grain size around 60-100 nm.

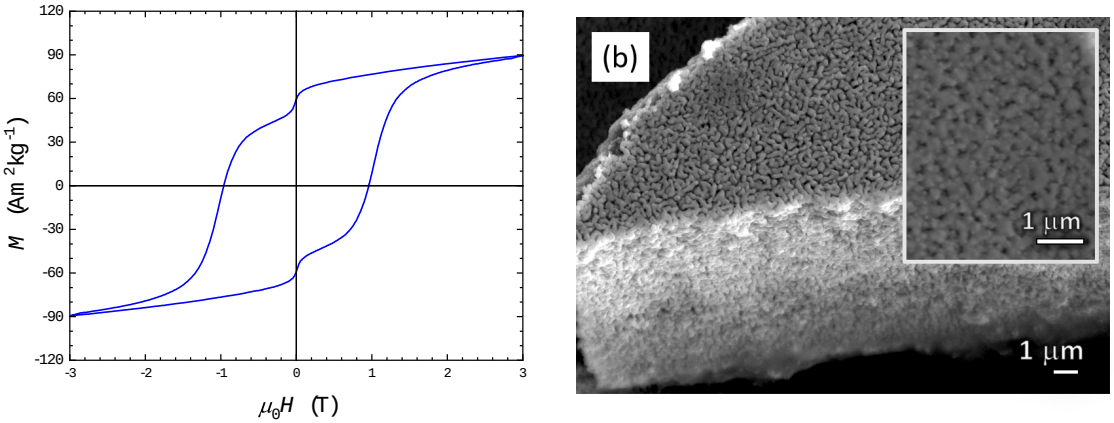

Figure 4.15: (a) Hysteresis curve and (b) secondary electrons image of optimally annealed melt-spun $Sm_{12}Fe_{73}V_{15}$ ribbons.

4.5 Summary and conclusions

This chapter presented different approaches to develop $\mu_0 H_c$ in Sm-Fe-V alloys. In the first part, the stoichiometric $SmFe_{10}V_2$ alloy was mechanical milled in hexane for different times in order to reduce the grain size. As the milling time increased, the XRD peaks of 1:12 phase broaden until there was a decomposition into the metastable 1:7 and α-(Fe,V) phases for 4 h milling. The highest $\mu_0 H_c$ value was found to be 0.21 T and the mean crystallite of nm, computed from Scherrer broadening. After trying different heat treatments for the as-milled powders, the 1:12 phase was not formed.

In the second part, to compensate the Sm-losses during the heat treatment process, we worked with off-stoichiometric $Sm_{12}Fe_{75}V_{13}$ as-cast alloys. As the 1:12 structure was not initially

formed, subsequent heat treatment was made. Also we attempted to improve the microstructure developing an eutectic alloy of Sm-La by adding La. Although a uniform 1:12 microstructure of fine, 1-10 μm grains surrounded by a La-rich phase was obtained, the maximum $\mu_0 H_c$ was 0.33 T. Heat treatments at different temperatures allowed to suppress and to stabilize the $SmFe_2$ phase; the $\mu_0 H_c$ was found to be consistently higher when the $SmFe_2$ phase was present in the alloy.

In the last part, nanocrystalline magnetic powders from $Sm_{12}Fe_{73}V_{15}$ by both mechanical milling and melt spinning from were produced. After performing short heat treatments on the as-milled powders and melt-spun ribbons, the hard 1:12 was formed as majority phase accompanied by a small α-(Fe,V) and other secondary phases such as $SmFe_2$ and Sm-oxides. The $\mu_0 H_c$ value could be tuned optimizing the grain size by varying the heat treatment conditions. $Sm_{12}Fe_{73}V_{15}$ powders and ribbons demonstrated $\mu_0 H_c$ values up to 1 T, comparable to those already published in literature. Despite the presence of the Sm-oxides phases, this material showed reasonable extrinsic magnetic properties.

Chapter 5

Fabrication of bulk Sm-Fe-V based 1:12 magnets

To achieve a practical application for the high-coercivity powder, a process of consolidation or densification is necessary to transform the powder into a bulk material and preferably into a fully-dense magnet. In this process, it is important that the bulk material maintains or develop the proper microstructure to keep or even improve the magnetic properties of the powder in the bulk form. In this chapter, we report the preparation of Sm-Fe-V based bulk magnets by hot compaction of mechanically milled powders. Structural, microstructural and magnetic properties, as well as the thermal stability of $\mu_0 H_c$ and $\mu_0 M_r$ of these magnets are investigated in detail. In the last part of the chapter, we show the results of the attempts we made to obtain an anisotropic magnet by hot deformation of the alloys with substitutions of V by Ti, Cu and Mo metals.

5.1 Introduction

The early attempts to develop reasonable hard magnetic properties in the Sm-based 1:12 alloys, produced $\mu_0 H_c$ values ranging between 0.59-1 T in Sm-Fe-V(Ti) melt-spun ribbons [134, 57, 135] and between 0.5-1.17 T in Sm-Fe-V alloys prepared by mechanical alloying [132]. Additional substitutions in Sm-Fe-(V/Ti,X) with X = Zr, Nb, Mo, W and Ga did not lead to significant improvement in $\mu_0 H_c$ value [136, 117]. Most of the Sm-based compounds have sufficiently

high values of T_C and H_A for technical applications, however experiments with sintering of powdered $Sm(Fe,M)_{12}$ alloys into fully dense magnets were not successful in keeping the powder properties [137].

Only a couple of attempts of producing bonded magnets were successful. Shultz et al. [132] reported a Sm-Fe-V based resin bonded magnet with 1.17 T of $\mu_0 H_c$ prepared from mechanically alloyed powders. Pinkerton et al. [134] reported a bulk magnet of $Sm_{0.89}Fe_{10}V_2$ produced by hot pressing of melt spun ribbons at 850°C, however the $\mu_0 H_c$ was only 0.56 T. The main challenge in making a bulk magnet is to obtain 1:12 phase while suppressing the formation of α−(Fe,M) because of the loss of Sm-metal during the various stages of processing due to evaporation and oxidation. Development of high $\mu_0 M_r$ in the final magnet, optimizing the microstructure and maintaining it throughout the processing of the bulk sample is crucial.

5.2 Hot-pressed magnets

5.2.1 Sample preparation

The as-milled powders $Sm_{12}Fe_{73}V_{15}$ from section 4.4.2 were hot compacted at 650°C in vacuum using a WC die by applying a pressure of ≈ 220 MPa. In this process, the sample was heated to 650°C at a heating rate of 65°C/min and the pressure was applied for 13 min. Finally, the sample was cooled to room temperature and a 92%-dense isotropic magnet was obtained. The hot-compacted sample was then heat-treated at 700°C for 15 to 60 min (hereafter referred to as heat-treated compact) to optimize the coercivity. To obtain an anisotropic magnet, hot-deformation was used as described in the section 5.3.

5.2.2 Structural analysis

Figure 5.1 shows the XRD patterns of $Sm_{12}Fe_{73}V_{15}$ sample at different stages of the processing. The XRD patterns in Fig. 5.1(a) and (b) correspond to the homogenized sample and the as-milled powder,respectively, which were discussed previously in section 4.4.2. The XRD pattern of the hot-compacted sample Fig. 5.1(c) shows very broad peaks indicating very fine grains and is quite similar to the XRD pattern of the powder which was heat-treated at 600°C for 30 min (See Fig. 4.12). The XRD peaks were attributed to the 1:12 and 1:2 phases along with Sm oxides.

The same Sm-oxides were observed in the heat-treated powders presented in section 4.4.2. After a short heat treatment at 700°C for 30 min, the XRD pattern Fig. 5.1(d) of the compacted piece showed sharper and well-defined peaks compared with the previous stage, indicating an increase in the grain size. The phases (and volume fractions) were identified as 1:12 (86.1%), 1:2 (1.9%), SmO (5.0%), Sm_2O_3 (3.1%), Sm_2O_3 (3.1%) and a very small amount of α-(Fe,V) (0.9%). From the volume fractions, one can see how the 1:2 phase is reduced by a 89% after all the processing, which means that the formation of the 1:2 phase (generated by the initial excess of Sm) has prevented loss of the 1:12 phase. The Rietveld refinement parameters are summarized in Table 5.1.

Table 5.1: Lattice parameters of 1:12 phase and volume fractions of different phases present at each stage of the processing of the $Sm_{12}Fe_{73}V_{15}$ magnet.

Stage	Lattice Parameters		Volume fraction					
	a (Å)	b (Å)	$V_{1:12}$ (%)	$V_{1:2}$ (%)	$V_{\alpha\text{-(Fe,V)}}$ (%)	V_{SmO} (%)	$V_{Sm_2O_3}^{(Pn\bar{3}m)}$ (%)	$V_{Sm_2O_3}^{(I2_13)}$ (%)
Homogenized	8.527	4.769	84.9	14.3	0.8			
Hot-compacted	8.489	4.817	87.1	4.1	1.9	2.1	2.4	2.4
Annealed hot-compacted	8.503	4.773	87.1	1.9	0.9	5.0	3.1	3.1

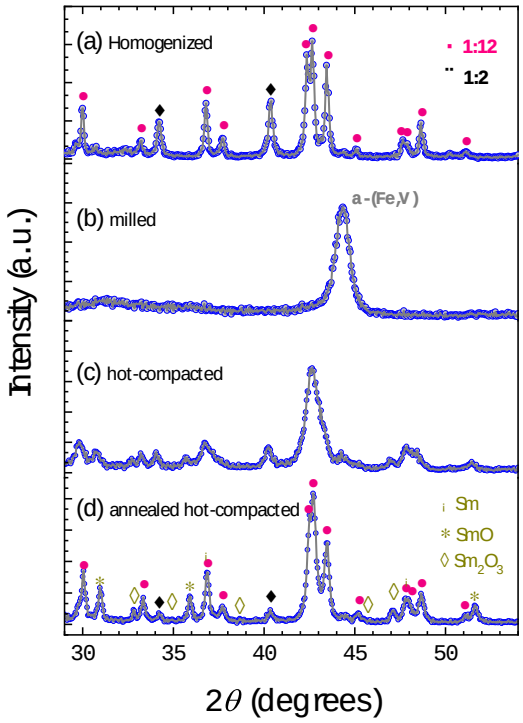

Figure 5.1: The XRD patterns of $Sm_{12}Fe_{73}V_{15}$ (a) alloy homogenized at 800°C for 20 h (b) after high energy milling for 10 h in Ar (c) hot-compacted at 650°C and (d) optimally annealed hot-compacted (heat treated at 700°C for 30 min).

5.2.3 Magnetic properties

Figure 5.2(b) displays the evolution of the hysteresis loops of homogenized, as-milled, hot-compacted and the optimally annealed hot-compacted $Sm_{12}Fe_{73}V_{15}$ samples, measured by applying a maximum field of 3 T at room temperature. Table 5.2 summarizes the magnetic properties of samples at different processing stages. The homogenized sample shows $\mu_0 H_c$ and $\mu_0 M_{3T}$ of 0.09 T and 0.62 T (64 Am^2kg^{-1}), respectively. After milling, the value of $\mu_0 M_r$ increases to (102 Am^2kg^{-1}) and the $\mu_0 H_c$ was measured to be 0.02 T, which is very low due to the absence of high-anisotropy phase and large volume fraction of the α-(Fe,V) solid solution.

As hot-compacted sample exhibit a $\mu_0 M_{3T}$ of 0.64 T (74 Am^2kg^{-1}) and $\mu_0 H_c$ of 0.57 T. Different pieces cut from the compacted were subjected to additional annealing at 700°C for 15 to 60 min to optimize the $\mu_0 H_c$ value. Fig. 5.2(a) shows the hysteresis loops for the corresponding

heat treatments, from here the optimized time was found to be 30 min, however it is clear that the magnetic properties are relatively stable in a time window of 1 h. Optimal heat treatment of the hot-compacted magnet results in an increase of $\mu_0 H_c$ to 1.06 T, the highest value reported so far in 1:12 bulk magnets. The $\mu_0 M_{3T}$, $\mu_0 M_r$ and $(BH)_{max}$ were 0.59 T (64 Am^2kg^{-1}), 0.42 T (46 Am^2kg^{-1}) and 28 kJm^{-3} (3.5 MGOe) respectively. The hysteresis loops of the hot compacted and optimally annealed hot-compacted sample did not show any zero-field steps which could indicate presence of the soft magnetic α-(Fe,V) phase, which is consistent with the XRD results.

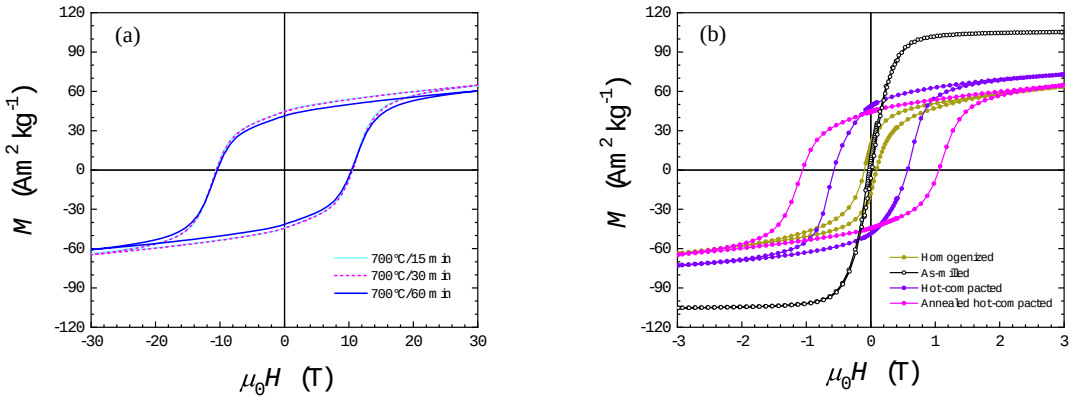

Figure 5.2: Hysteresis loops of $Sm_{12}Fe_{73}V_{15}$ (a) heat-treated compacted pieces at 700°C for 15 to 60 min (b) at different stages of the processing: homogenized, after milling for 10 h, hot-compacted and optimally annealed hot-compacted.

We obtained greater coercivity and better loop rectangularity than Pinkerton and Van Wingerden [134], the only earlier reported fully dense Sm-Fe-V magnet ($\mu_0 H_c$ = 0.56 T, $\mu_0 M_r$ = 0.54 T in $Sm_{15}Fe_{70}V_{15}$). The improvement may be due to the use of high-energy milling to produce the nanocrystalline precursor material rather than the melt-spinning. Indeed, the coercivity values achieved in this work are similar to those reported by Schultz et al. [132] ($\mu_0 H_c$ = 1.17 T, $\mu_0 M_r$ = 0.49 T in $Sm_{15}Fe_{70}V_{15}$) who employed mechanical alloying but did not prepare a fully dense magnet. On the other hand, the higher remanence values reported by Ding and Rosenberg [135] for melt-spun Sm-Fe-Co-V alloys indicate that a partial Co substitution for Fe may increase the energy density of the fully dense Sm-Fe-V magnets even in the absence of the crystallographic texture.

Table 5.2: Magnetic properties of the $Sm_{12}Fe_{73}V_{15}$ sample at different stages of processing. Values of $\mu_0 H_c$, $\mu_0 M_{3T}$ and $\mu_0 M_r$ in the parenthesis are given in Am^2kg^{-1}. The value of $(BH)_{max}$ in parenthesis is given in MGOe.

Stage	$\mu_0 H_c$ (T)	$\mu_0 M_{3T}$ (T)	$\mu_0 M_r$ (T)	$(BH)_{max}$ (kJm^{-3})
Homogenized	0.09	0.62 (64)	0.25 (26)	4 (0.5)
Milled	0.02	- (102)	- (7)	- -
Hot compacted	0.57	0.64 (74)	0.45 (51)	31 (3.8)
Annealed hot-compacted	1.06	0.59 (64)	0.42 (46)	28 (3.5)

In order to study the coercivity mechanism, the virgin and demagnetization curves were measured and are shown in Fig. 5.3. The virgin magnetization curve shows a susceptibility that increases with the applied field going through a maximum at 0.9 T, a field comparable with the maximum coercivity of the sample, consistent with the fact that the maximum amount of reversals occurs at this field. The susceptibility falls off again as the magnetization is approaching to saturation at high fields. The dependence of coercivity and remanent magnetization on applied field $\mu_0 H_m$, which is determined from the demagnetization curves, are plotted in the inset of Fig 5.3. The remanent magnetization and coercivity curves show a similar behavior: a small initial increase with $\mu_0 H_m$ until $\mu_0 H_m$ becomes comparable to the coercivity, whereupon both $\mu_0 H_c$ and M_r increase dramatically to saturation. This kind of behavior is similar to the isotropic nanocrystalline hard magnetic materials (like Nd-Fe-B). However, the role of domain wall-pinning can not be completely discarded.

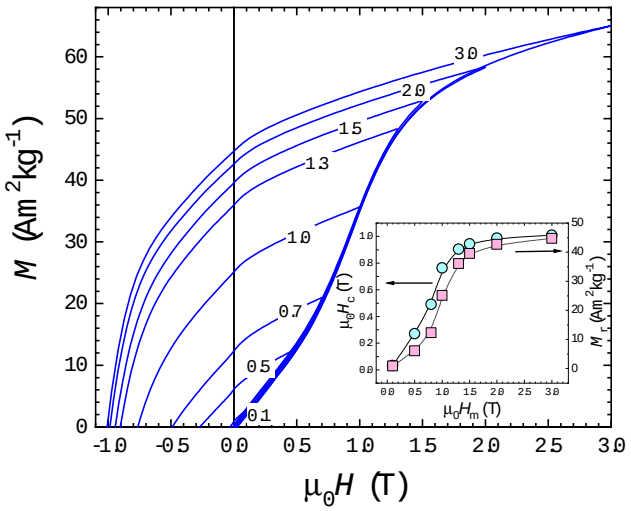

Figure 5.3: Virgin and demagnetization curves at room temperature of the optimally annealed hot-compacted $Sm_{12}Fe_{73}V_{15}$ magnet. The field value on each demagnetization curve is the maximum applied field in T. The sample was thermally demagnetized before the measurement of each curve.

Thermomagnetic curve of the optimally annealed hot-compacted sample is shown in Fig. 5.4. The curve exhibits a pronounced peak known as Hopkinson maximum followed by an abrupt drop of the curve on the high-temperature side, and a minor second step at a slightly higher temperature. The shape of the Hopkinson peak is characteristic of low field susceptibility of many ferromagnets, in which anisotropy falls off more rapidly than magnetization with the temperature. In analyzing the curves, the inflection points are taken as T_C, 330°C for 1:12 and 411°C for 1:2 phase.

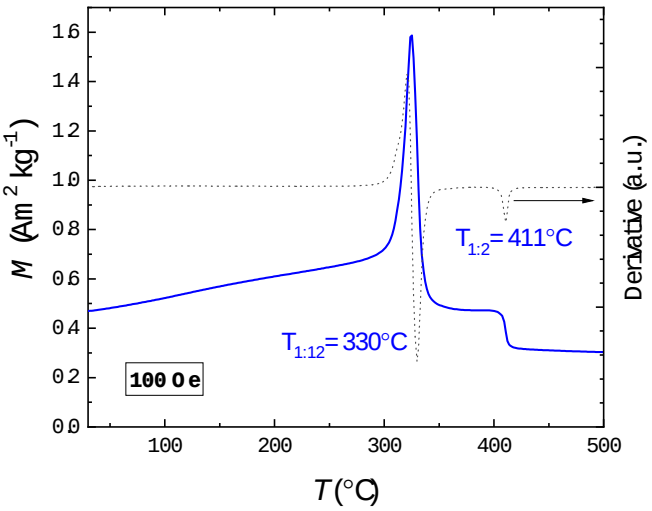

Figure 5.4: Temperature dependence of the magnetization of annealed hot-compacted $Sm_{12}Fe_{73}V_{15}$ magnet under an applied field of 0.01 T. The dotted line shows dM/dT vs. T.

5.2.4 Thermal Effects

Figure 5.5(a) shows the second quadrant of hysteresis loops measured at temperatures ranging from -223 to 327°C for the optimally annealed hot-compacted magnet. The temperature dependence of $\mu_0 M_r$ and $\mu_0 H_c$, are shown in Fig. 5.5(b). Here, $\mu_0 H_c$ and $\mu_0 M_r$ decreases with increasing temperature, and ultimately the $\mu_0 M_r$ becomes zero at the T_C of the 1:12 phase (330°C). Similarly, to the Nd-Fe-B magnets [138], the decrease in $\mu_0 H_c$ is more prominent than $\mu_0 M_r$. The values of $\mu_0 H_c$ and $\mu_0 M_r$ are found to be 2.6 T and 0.5 T (51 Am^2kg^{-1}) at -223°C and 0.5 T and 0.3 T (33 Am^2kg^{-1}) at 177°C, respectively.

Temperature coefficients α and β, are calculated using eq. B.6 and B.7 (see Appendix B, eq. B.6 and B.7). The coefficients of the polynomial regressions and r-square are shown in Table 2. The absolute values of α and β in the temperature range from 20 to 100°C are 0.14%°C^{-1} and 0.39%°C^{-1}, respectively. The coefficient β is significantly lower than that of standard Nd-Fe-B sintered or hot-deformed magnets, which is about 0.55% °C^{-1} [138, 139].

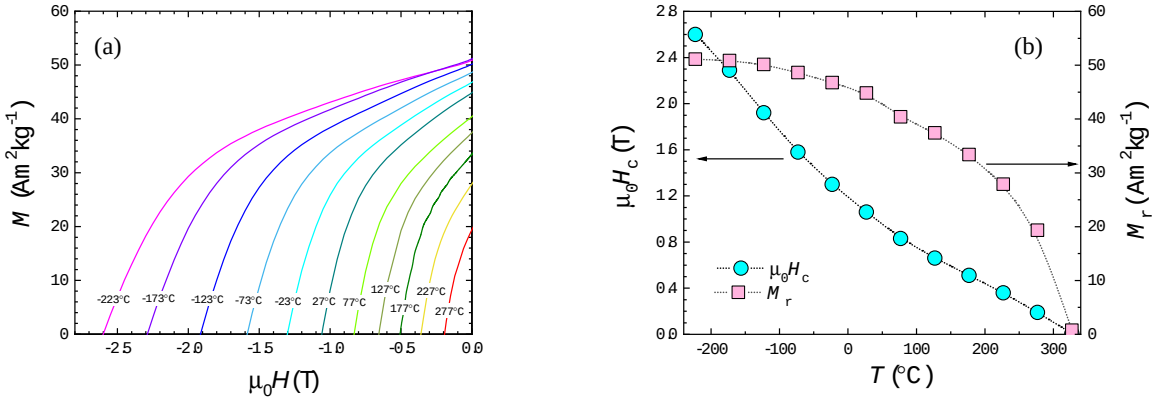

Figure 5.5: (a) Demagnetization curves measured at different temperatures and (b) temperature dependence of coercivity and remanence of the annealed hot compacted $Sm_{12}Fe_{73}V_{15}$ magnet.

5.2.5 Microstructure

After 10 h of intensive milling, the particle size distribution is homogeneous enough, and the particle size is between 2 to 10 μm, as it can be seen in Fig. 5.6(left). Fig. 5.6(right) shows the microstructure of the compacted sample. In general, the grains are well-packed and inter-grain pores of few micrometers (< 5 μm) are only visible at higher magnification. Density was measured indirectly using the Arquimedes method, and it was calculated to be 7.026 g/cm^3, corresponding to the 92% of the density.

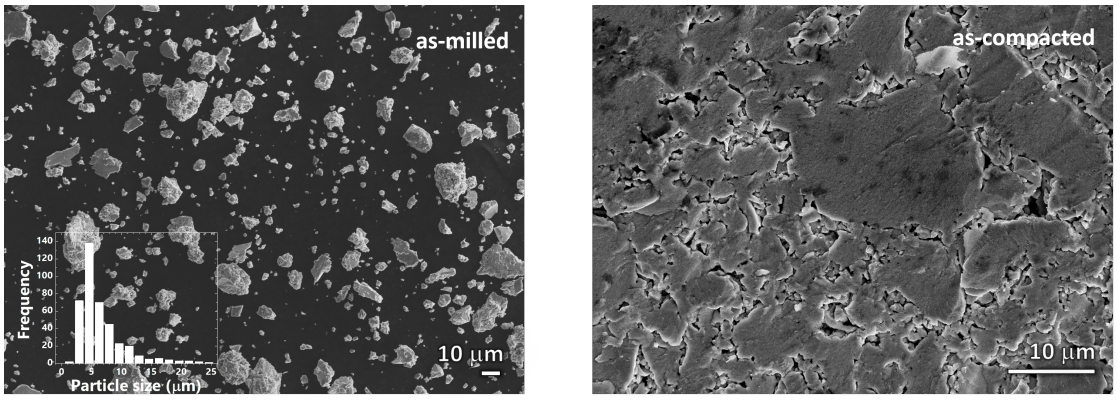

Figure 5.6: SEM secondary electrons-image of as-milled powder and fractured surface of the as-compacted $Sm_{12}Fe_{73}V_{15}$ magnet.

Typical TEM bright field image of the optimally annealed hot-compacted $Sm_{12}Fe_{73}V_{15}$ magnet is shown in Fig. 5.7. The image reveals very fine grains of approximately 89 ± 25 nm with a not too broad distribution. The grains have the shape of irregular prisms and its possible to observe triple junctions, where three grains meet.

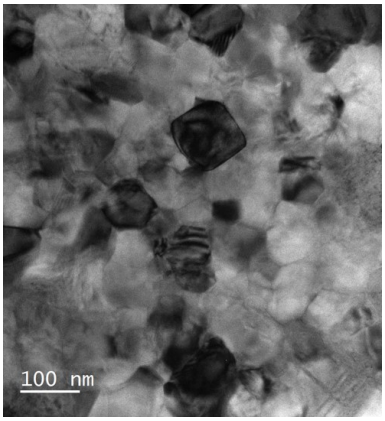

Figure 5.7: Bright field TEM micrograph of the optimally annealed hot-compacted $Sm_{12}Fe_{73}V_{15}$ magnet.

The high $\mu_0 H_c$ obtained in the optimally annealed compacted sample could be attributed to the fine grain size. The as-milled structure aids to the formation of a very fine grain microstructure of 1:12 phase during the hot compaction. The amorphous powder particles of approximately 6 μm evidently transform into tiny polycrystals once they are hot pressed. After

short heat treatment, every particle may contain at about about 67 (6000/89 : size of amorphous particles/average grain size) nanocrystalline grains.

5.3 Hot-deformed magnets

5.3.1 Sample preparation

As mentioned before, to obtain an anisotropic magnet, a hot-compacted magnet with the same composition $Sm_{12}Fe_{73}V_{15}$ was reproduced and deformed up to 75% of its original height, parallel to the press direction at 800°C. The process was employed to the other systems in which V was reduced $Sm_{12}Fe_{76.5}V_{11.5}$ or partially substituted by another transition metal: $Sm_{12}Fe_{73}V_{7.5}Ti_{7.5}$, $Sm_{12}Fe_{73}V_{7.5}Mo_{7.5}$ and $Sm_{12}Fe_{74}V_{12}Cu_2$. Figure 5.8 shows a photograph of how the magnets look before and after the deformation. Surfaces of the hot-compacted and deformed magnets, likely to contain impurities, were machined off prior to characterization. Densities of the magnets were determined with the Archimedes method using water as immersion liquid. Samples cut from the compacted and deformed magnets were immobilized with paraffin wax in teflon holders and used for magnetic measurements. The hysteresis loops were corrected for self-demagnetization effect.

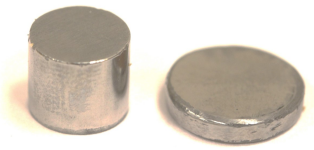

Figure 5.8: Photograph of $Sm_{12}Fe_{73}V_{15}$ hot-compacted (left) and hot-deformed (right) magnets.

Hysteresis loops of $Sm_{12}Fe_{73}V_{15}$ hot-deformed magnet measured parallel ($\parallel$) and perpendicular ($\perp$) to the compression direction (ΔL) are shown in Fig 5.9(a). After deformation at 800°C, $\mu_0 M_{3\mathrm{T}}$ remains almost unchanged at 0.63 T (66.4 $\mathrm{Am^2kg^{-1}}$) and the $\mu_0 H_\mathrm{c}$ is increased to 0.88 T compared with $\mu_0 M_{3\mathrm{T}}$ of 0.64 T (74 $\mathrm{Am^2kg^{-1}}$) and $\mu_0 H_\mathrm{c}$ of 0.57 T of the hot-compacted magnet prepared in section 5.2. An $\mu_0 M_\mathrm{r}$ value of 0.45 T (47 $\mathrm{Am^2kg^{-1}}$) and 0.42 T (44 $\mathrm{Am^2kg^{-1}}$) are

obtained when the hysteresis loops were measured with field applied ⊥ and ∥ directions, respectively, indicating a small degree of anisotropy (DOA) development in the plane perpendicular to the deformation. This is in contrary to that of $Nd_2Fe_{14}B$ based hot-deformed magnets, where the *c*-axis of grains aligns along the press direction [139, 140]. The DOA was calculated using the formula DOA $= (\mu_0 M_r^{\perp} - \mu_0 M_r^{\parallel})/\mu_0 M_r^{\perp}$, where $\mu_0 M_r^{\perp}$ and $\mu_0 M_r^{\parallel}$ are the remanence measured ⊥ and ∥ to the deformation. The deformed magnet shows a DOA value of 0.095. The $(BH)_{max}$ of 33 kJm^{-3} (4.1 MGOe) was obtained from the hysteresis loop measured in ⊥ direction.

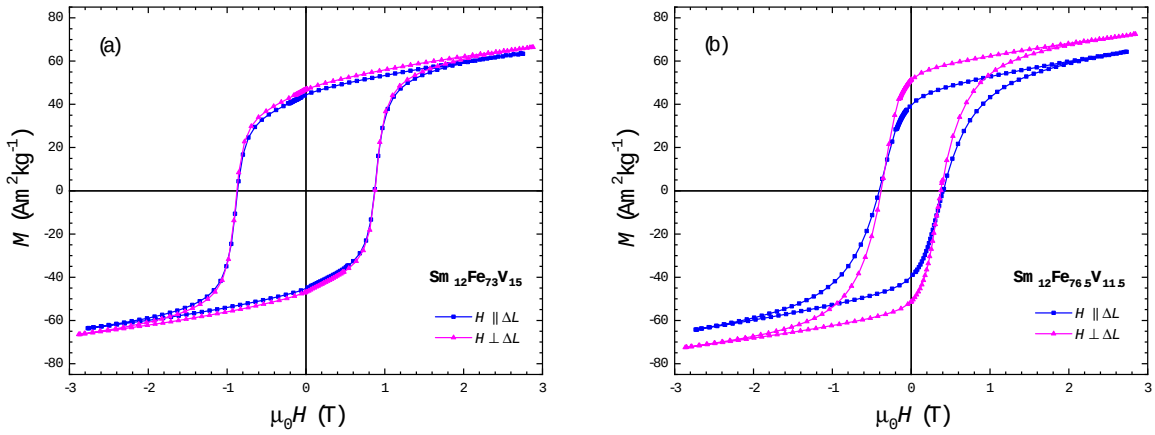

Figure 5.9: Hysteresis loops of the hot-deformed magnet measured parallel (∥) and perpendicular (⊥) to the deformation (a) $Sm_{12}Fe_{73}V_{15}$ and (b) $Sm_{12}Fe_{76.5}V_{11.5}$.

When V content is reduced from 15 to 11.5 at.%, and the compacted magnet is deformed at 1000°C (see Fig. 7(b)), there is a noticeable increase in the DOA to 0.286 resulting in $\mu_0 M_r^{\perp}$ of 0.47 T (52 Am^2kg^{-1}) and $\mu_0 H_c$ of 0.41 T. Also T_C exhibits a notable increase from 330 to 380°C as is displayed in Fig. 5.10. Table 5.3 summarizes the magnetic properties of the $Sm_{12}Fe_{73}V_{15}$ and $Sm_{12}Fe_{76.5}V_{11.5}$ hot-deformed magnets.

Table 5.3: Magnetic properties of $Sm_{12}Fe_{73}V_{15}$ and $Sm_{12}Fe_{76.5}V_{11.5}$ hot-deformed magnets. Values in parenthesis are given in Am^2kg^{-1}. The value of $(BH)_{max}$ in parenthesis is given in MGOe.

Magnet	T_{deform} (°C)	$\mu_0 M_r^{\perp}$ (T)	$\mu_0 M_r^{\parallel}$ (T)	DOA	T_C (°C)	M_{3T} (T)	$\mu_0 H_c$ (T)	$(BH)_{max}$ (kJm^{-3})
$Sm_{12}Fe_{73}V_{15}$	800	0.45 (47)	0.42 (44)	0.067	330	0.63 (66)	0.88	33 (4.1)
$Sm_{12}Fe_{76.5}V_{11.5}$	1000	0.47 (52)	0.37 (40)	0.213	380	0.67 (72)	0.41	29 (3.7)

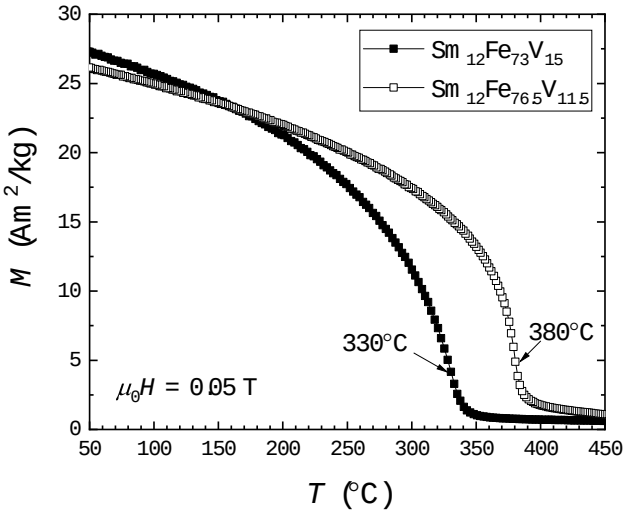

Figure 5.10: M(T) cooling curve measured in a magnetic field of 0.05 T depicting the Curie temperature of the 1:12 phase for $Sm_{12}Fe_{73}V_{15}$ and $Sm_{12}Fe_{76.5}V_{11.5}$.

As revealed by SEM examination in Fig. 5.11(b), much larger grains ranging between 0.3 and 1 μm are observed, which explain the markedly lower $\mu_0 H_c$ of 0.41 T. The grain growth takes place during the deformation at 1000°C. Although texture is clear from the magnetic measurements, the 1:12 grains maintain a nearly equiaxed morphology (unlike, for example, the $Nd_2Fe_{14}B$ grains in the hot-deformed Nd-Fe-B magnets [141]).

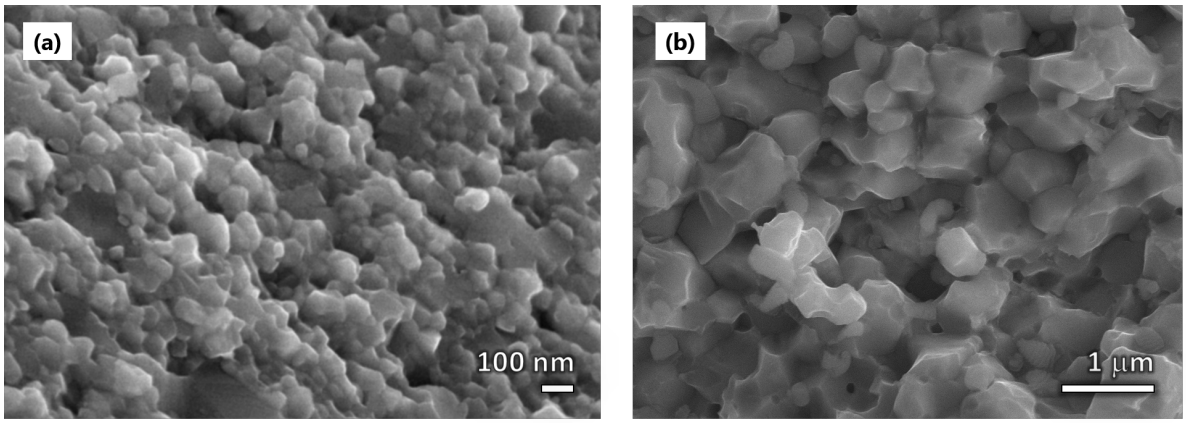

Figure 5.11: SEM Secondary electrons images of hot-deformed magnets (a) $Sm_{12}Fe_{73}V_{15}$ and (b) $Sm_{12}Fe_{76.5}V_{11.5}$.

5.3.2 The Sm-Fe-(V,M) hot-deformed magnets with substitution of V by M = Mo, Ti and Cu

In order study effect of elemental substitution on microstructure and magnetic properties, bulk magnets of Sm-Fe-V with V substituted by Mo, Ti and Cu were produced by following the same route of processing: arc melting → homogenization → ball milling → hot compaction → hot deformation. The compositions of the magnets investigated were $Sm_{12}Fe_{73}V_{7.5}Ti_{7.5}$, $Sm_{12}Fe_{73}V_{7.5}Mo_{7.5}$ and $Sm_{12}Fe_{74}V_{14}Cu_2$.

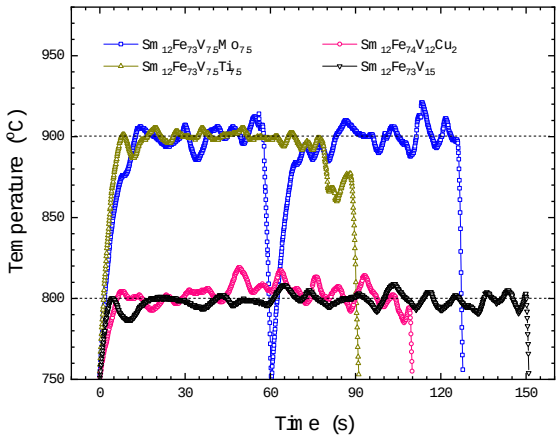

Figure 5.12: Temperature logs recorded during the hot deformation of $Sm_{12}Fe_{73}V_{15}$, $Sm_{12}Fe_{73}V_{7.5}Ti_{7.5}$, $Sm_{12}Fe_{73}V_{7.55}Mo_{7.5}$ and $Sm_{12}Fe_{74}V_{12}Cu_2$ hot compacted magnets

Hot-compacted magnets of $Sm_{12}Fe_{73}V_{15}$, $Sm_{12}Fe_{73}V_{7.5}Ti_{7.5}$, $Sm_{12}Fe_{73}V_{7.55}Mo_{7.5}$ and $Sm_{12}Fe_{74}V_{12}Cu_2$ were hot deformed at 900, 900, 800 and 800°C, respectively. Figure 5.12 shows the profiles of the hot deformation temperatures. The hot-compacted magnets with Cu substitution could be deformed by 75% in a time less than the time required to deform the compact without substitution. For example, the $Sm_{12}Fe_{73}V_{7.5}Cu_{7.5}$ magnet only needed 90 s to be deformed. The partial substitution of Cu seems to aid the deformation. It is not possible to comment on the role of Ti and Mo on the deformation as the temperatures of deformation used are different.

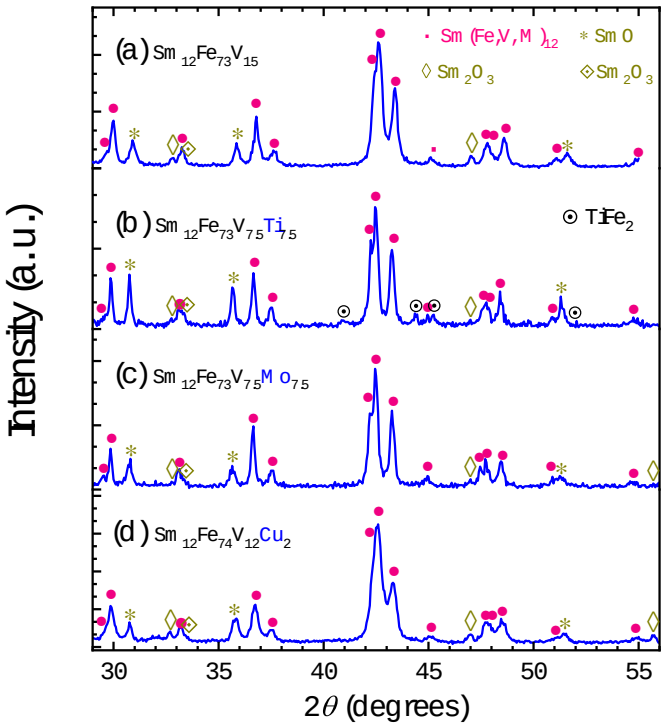

Figure 5.13: XRD patters of hot-deformed magnets (a) $Sm_{12}Fe_{73}V_{15}$ deformed at 800°C (b) $Sm_{12}Fe_{73}V_{7.5}Ti_{7.5}$ deformed at 900°C (c) $Sm_{12}Fe_{73}V_{7.55}Mo_{7.5}$ deformed at 900°C (d) $Sm_{12}Fe_{74}V_{12}Cu_2$ deformed at 800°C.

The XRD patterns of the Sm-Fe-(V,M) (M = Ti, Mo, Cu) hot-deformed magnets are shown in Fig. 5.13. As can be seen, the 1:12 phase is present in all the magnets. However, as deduced from the width of the XRD peaks, $Sm_{12}Fe_{73}V_{15}$ and $Sm_{12}Fe_{74}V_{12}Cu_2$ samples show broader peaks indicating finer grains compared to the $Sm_{12}Fe_{73}V_{7.5}Ti_{7.5}$ and $Sm_{12}Fe_{73}V_{7.5}Mo_{7.5}$ samples. The size of the grains in the hot-deformed magnets depends on the deformation temperature and composition. The former were deformed at lower temperatures (800°C) while the later at 900°C. In all the magnets, except for $Sm_{12}Fe_{73}V_{7.5}Ti_{7.5}$, the volume fraction of the 1:12 phase represents approximately 90%, and the 10% remaining represents Sm-oxides such as SmO (space group $Fm3m$) and 2 types of Sm_2O_3 (space groups $I2_13$ and $Pn\bar{3}m$). In the case of $Sm_{12}Fe_{73}V_{7.5}Ti_{7.5}$, the 1:12 volume fraction is 78% due to the formation of Fe_2Ti (7.5%) and Sm-oxides (14.5%). Table 5.4 summarizes the structural parameters of 1:12 phase and the volume fractions of the phases in the magnets.

The lattice constants of the 1:12 vary according with the element-substituted. A slight

decrease in the a and c constants is observed when V is substituted with Cu, whereas an increase is observed when V is substituted with Ti or Mo. This result is in agreement with the atomic radii of the corresponding elements, as $r_{\mathrm{Mo}} > r_{\mathrm{Ti}} > r_{\mathrm{V}} > r_{\mathrm{Cu}}$ [142]. This effect is especially visible in Fig. 5.13(d) where the $Sm_{12}Fe_{74}V_{12}Cu_2$ XRD pattern is shifted towards higher angles.

Table 5.4: Lattice parameters of the 1:12 phase and volume fractions of the phases present in the hot-deformed magnets. The density values were measured from Archimedes method.

	Lattice Parameters		Volume fraction				
Stage	a (Å)	b (Å)	$V_{1:12}$ (%)	V_{Fe_2Ti} (%)	V_{SmO} (%)	$V_{Sm_2O_3}^{(Pn\bar{3}m)}$ (%)	$V_{Sm_2O_3}^{(I2_13)}$ (%)
$Sm_{12}Fe_{73}V_{15}$	8.503	4.772	89.8		4.8	3.1	2.2
$Sm_{12}Fe_{73}V_{7.5}Ti_{7.5}$	8.533	4.784	77.9	7.5	8.4	1.0	5.1
$Sm_{12}Fe_{73}V_{7.5}Mo_{7.5}$	8.543	4.782	88.8		5.6	1.3	4.2
$Sm_{12}Fe_{74}V_{12}Cu_2$	8.480	4.769	91.1		3.8	2.7	2.3

Figure 5.14(a), (b) and (c) shows the hysteresis loops measured ∥ and ⊥ to the deformation direction for $Sm_{12}Fe_{73}V_{7.55}Ti_{7.5}$, $Sm_{12}Fe_{73}V_{7.55}Mo_{7.5}$ and $Sm_{12}Fe_{74}V_{12}Cu_2$. As can be seen, the $Sm_{12}Fe_{73}V_{7.55}Ti_{7.5}$ and $Sm_{12}Fe_{74}V_{12}Cu_2$ exhibit no texture. The $Sm_{12}Fe_{73}V_{7.55}Mo_{7.5}$ magnet shows a small texture of 20% and the anisotropy is in the plane perpendicular to the deformation direction. The same characteristic was observed for the $Sm_{12}Fe_{73}V_{15}$ and $Sm_{12}Fe_{76.5}V_{11.5}$ magnets.

The magnetic properties derived from the hysteresis loops are listed in Table 5.5. As can be seen, the substitution of V by Ti does not affect the magnetic properties significantly, the $\mu_0 H_{\mathrm{c}}$ remains unchanged at 0.88 T and $\mu_0 M_{3\mathrm{T}}$ and T_{C} slightly decrease from 330 to 325°C and from 0.63 (66) to 0.54 T (58 $\mathrm{Am^2kg^{-1}}$), respectively. On the other hand, the substitution of V by Mo, results in an considerable decrease of T_{C} from 330 to 268°C and $\mu_0 H_{\mathrm{c}}$ from 0.88 T to 0.45 T. The $\mu_0 M_{3\mathrm{T}}$ barely changes being 0.62 T (62 $\mathrm{Am^2kg^{-1}}$). Although the $\mu_0 H_{\mathrm{c}}$ is low, the $(BH)_{\mathrm{max}}$ of 33 $\mathrm{kJm^{-3}}$ is comparable to the 31 $\mathrm{kJm^{-3}}$ of $Sm_{12}Fe_{73}V_{15}$, this is due to the additional 20% degree of texture. The substitution of V by Cu is reflected in a notable increase of T_{C} from 330 to 362°C, $\mu_0 H_{\mathrm{c}}$ from 0.88 to 0.96 T and $\mu_0 M_{3\mathrm{T}}$ from 0.63 (66) to 0.68 T (62 $\mathrm{Am^2kg^{-1}}$). From all the magnets the $Sm_{12}Fe_{74}V_{12}Cu_2$ showed the largest $(BH)_{\mathrm{max}}$ of 42 $\mathrm{kJm^{-3}}$.

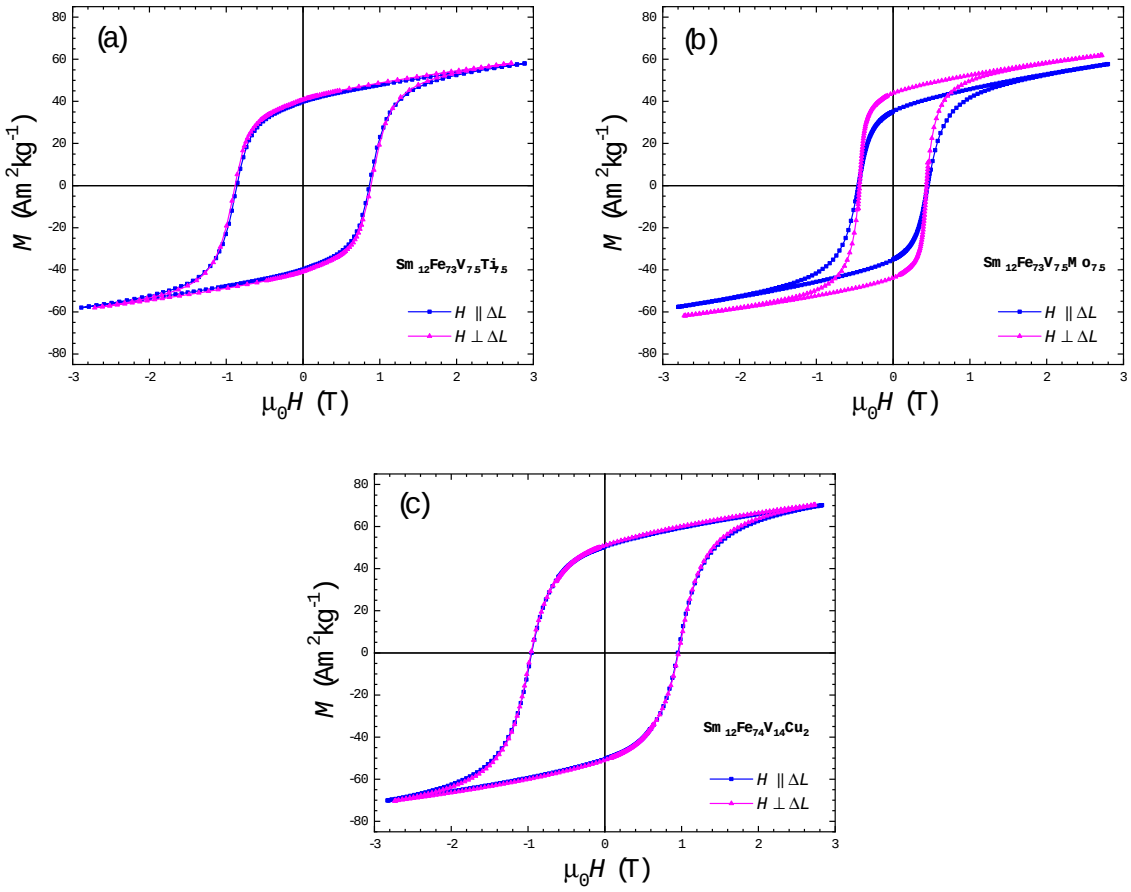

Figure 5.14: Hysteresis loops of hot-deformed magnets measured parallel and perpedicular to the pressing direction (a) $Sm_{12}Fe_{73}V_{7.5}Ti_{7.5}$ (b) $Sm_{12}Fe_{73}V_{7.5}Mo_{7.5}$ (c) $Sm_{12}Fe_{74}V_{12}Cu_2$.

Table 5.5: Magnetic properties of $Sm_{12}Fe_{73}V_{7.5}Ti_{7.5}$, $Sm_{12}Fe_{73}V_{7.5}Mo_{7.5}$ and $Sm_{12}Fe_{74}V_{14}Cu_2$ hot-deformed magnets. Values in parenthesis are given in Am^2kg^{-1}. The value of $(BH)_{max}$ in parenthesis is given in MGOe.

Magnet	T_{deform} (°C)	$\mu_0 M_r^{\perp}$ (T)	$\mu_0 M_r^{\parallel}$ (T)	DOA	T_C (°C)	$\mu_0 M_{3T}$ (T)	$\mu_0 H_c$ (T)	$(BH)_{max}$ (kJm^{-3})
$Sm_{12}Fe_{73}V_{7.5}Ti_{7.5}$	900	0.38 (41)	0.37 (40)	0.026	325	0.54 (58)	0.88	26 (3.2)
$Sm_{12}Fe_{73}V_{7.5}Mo_{7.5}$	900	0.44 (44)	0.35 (35)	0.205	268	0.62 (62)	0.45	31 (3.9)
$Sm_{12}Fe_{74}V_{14}Cu_2$	800	0.49 (51)	0.49 (51)	0.000	362	0.68 (62)	0.96	42 (5.3)

SEM images of a broken piece of $Sm_{12}Fe_{74}V_{12}Cu_2$ show a fine grained structure with grains of 83 ± 17 nm (Fig. 5.15(a)). The grains are well-packed and have the form of well-defined prisms (some of them hexagonal) like in sintered magnets. This magnet with the highest $\mu_0 H_c$ has the most uniform microstructure. The $Sm_{12}Fe_{73}V_{7.5}Mo_{7.5}$ on the other hand shows a much larger grained structure with grains of 1.1 ± 0.3 μm in diameter. The grain morphology corresponds to irregular prisms, and along the boundaries one can observe pores of different sizes.

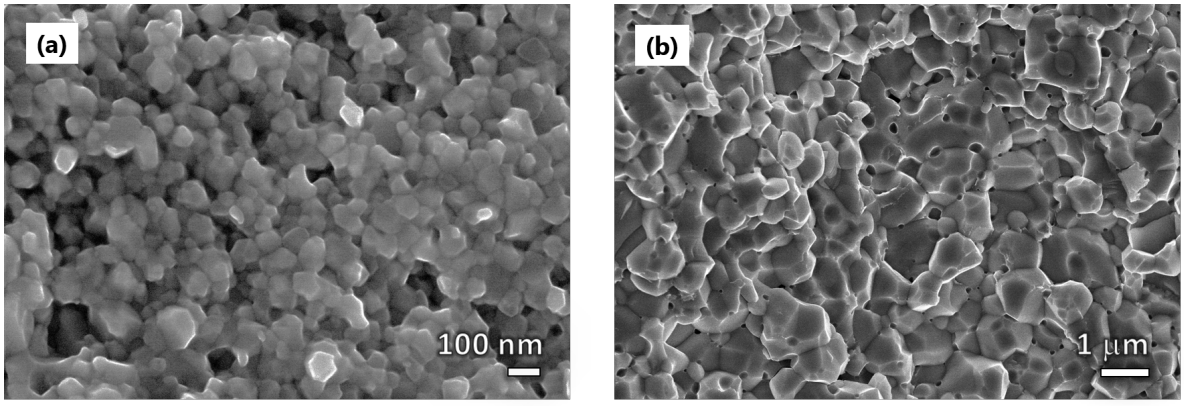

Figure 5.15: Secondary-electrons images of hot-deformed magnets (a) $Sm_{12}Fe_{74}V_{12}Cu_2$ and (b) $Sm_{12}Fe_{73}V_{7.5}Mo_{7.5}$

Figure 5.16 shows a TEM image and EDX elemental map analysis of $Sm_{12}Fe_{73}V_{7.5}Ti_{7.5}$. The microstructure shows a relatively large grain size distribution with grain sizes around 105 ± 30 nm. This can be partly related to the presence of secondary phases such as Fe_2Ti and Sm-oxides. The grain size is coarser than that in $Sm_{12}Fe_{73}V_{15}$ and $Sm_{12}Fe_{74}V_{14}Cu_2$. In the EDX map, the Sm and Ti are not distributed homogeneously. Sm-rich and Ti-rich grains are observed through the sample. The Ti-rich grains corresponds to Fe_2Ti phase.

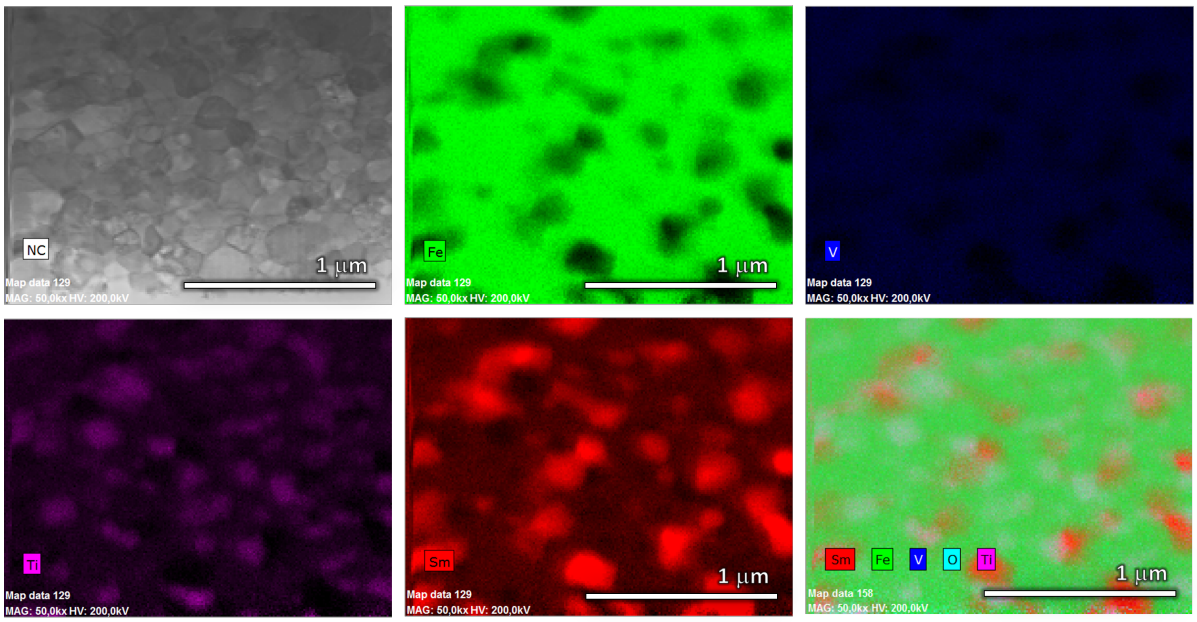

Figure 5.16: TEM/EDX elemental map analysis of $Sm_{12}Fe_{73}V_{7.5}Ti_{7.5}$ hot-deformed magnet.

5.4 Summary and Conclusions

This chapter deals with the fabrication of 1:12 Sm-Fe-V bulk magnets. For this purpose, the as-milled powders produced based on the results from chapter 4, were hot-compacted. In order to obtain anisotropic magnets, the hot-compacted magnets were hot deformed.

In the first section, a bulk magnet based on Sm-Fe-V with 1:12 structure was successfully consolidated into a bulk magnet by pressing mechanically milled $Sm_{12}Fe_{75}V_{13}$ powders at 650°C. The relative density of the as-compacted magnet reached a 92% of the theoretical density. The isotropic magnet exhibited a maximum $\mu_0 H_c$ of 1.06 T, $\mu_0 M_{3T}$ of 0.59 T, $\mu_0 M_r$ of 0.42 T and a $(BH)_{max}$ of 28 kJm^{-3} at 3 T applied field. The T_C was found to be 330°C and the temperature coefficients of remanent magnetization and coercivity, measured in the range of 0-100°C, were α = 0.14%C^{-1} and β = 0.39%C^{-1}, respectively, the latter is comparatively lower than that of NdFeB magnets. Minor hysteresis loops indicated a coercivity mechanism similar to that of the nanocrystalline Nd-Fe-B magnets. The isotropic magnet was hot-deformed up to 75% of its height, and the best magnetic properties obtained were $\mu_0 M_{3T}$ = 0.63 T, $\mu_0 M_r$ = 0.45 T, $\mu_0 H_c$ = 0.88 T and $(BH)_{max}$ = 33 kJm^{-3}.

Following the same route of processing, magnets of Sm-Fe-(V,M) (M = Ti, Mo, Cu) were synthesized in order to investigate the effect on the magnetic properties of $Sm_{12}Fe_{75}V_{13}$ when V was reduced or partially substituted by another transition metal. All the mechanically milled powders were successfully consolidated into fully-dense magnets. A small texture (21%) in the plane perpendicular to the pressing direction was detected for $Sm_{12}Fe_{76.5}V_{11.5}$ deformed at 1000°C. Same type and degree of texture (20%) was also observed in $Sm_{12}Fe_{73}V_{7.5}Mo_{7.5}$ deformed at 900°C. The $Sm_{12}Fe_{74}V_{12}Cu_2$ magnet showed the best performance with T_C = 362°C, $\mu_0 H_c$ = 0.96 T, $\mu_0 M_{3T}$ = 0.68 T (62 Am^2kg^{-1}) and $(BH)_{max}$ = 42kJm^{-3}.

The examination of the microstructure showed that the magnets made of (V,Cu), (V,Ti) and only V were composed of fine grains with sizes between 60 and 150 nm. Although the $Sm_{12}Fe_{73}V_{7.5}Ti_{7.5}$ magnet had larger grains than $Sm_{12}Fe_{75}V_{13}$, the magnetic properties remained constant, including the $\mu_0 H_c$ of 0.88 T. This fact can partly be related with the presence of the secondary phase Fe_2Ti, which is homogeneously distributed through the sample. From all the magnets, the $Sm_{12}Fe_{74}V_{12}Cu_2$ microstructure was the most uniform and reminds the microstructure of a sintered magnet, the small amount of Cu, not only improve the magnetic properties but also slightly refine the grain size. On the other hand, the substitution of V by Mo, favored the grain growth during the hot deformation, this has a detrimental influence on the T_C and $\mu_0 H_c$ which were 268°C and 0.45 T. Despite the $\mu_0 H_c$ of this magnet decreased severely mainly due to the grain coarsening, the small texture developed in this magnet led a $(BH)_{max}$ of 31 kJm^{-3}.

The most striking result was that some of the 1:12 Sm magnets developed a texture perpendicular to the deformation direction. This kind of behavior is different from that of die-upset Nd-Fe-B magnets, and is similar to that of observed in Mn-Al hot-deformed magnets [143, 144]. This kind of texture would indicate the use of hot extrusion rather than die-upsetting for the development of bulk magnets. These results encourage the study on highly textured ultrafine-grained magnets, reopening the development of 1:12 Sm-based anisotropic magnets.

Chapter 6

Conclusions

The main conclusions of this thesis are summarized as follows.

- Mössbauer analysis on the as-spun and heat-treated ribbons of $(Sm_{1-x}Ce_x)Fe_9Co_2Ti$ (x = 0.0, 0.25, 0.50, 0.75, 1.0) allowed to investigate the amorphous and crystalline character of the ribbons. The Sm substitution by Ce led to a redistribution of Co in the $8f$ and $8j$ sites. For $x \leq 0.5$, the occupation percentage for $8j$ and $8f$ sites was 70 and 30% whereas for $x > 0.5$ was 50 and 50%, respectively.

- The study of the 1:12 phase stability dependance on the content of stabilizing element V in $SmFe_{12-x}V_x$ alloys, revealed that 1:12 phase can be obtained in alloys with V content as low as x = 1.0. The $\mu_0 H_A$, $\mu_0 M_s$ and T_C were enhanced as the V concentration was reduced. The newly synthesized $SmFe_{11}V$ compound showed M_s of 1.12 T, large $\mu_0 H_A$ of 11 T, and a moderate T_C of 361°C. These properties make it an interesting candidate for permanent magnets applications. Further decrease in V content to x = 0.5, the 1:12 phase was not formed, instead 2:17 and α-(Fe,V) phases were observed.

- The substitution of Zr for Sm in $Sm_{1x}Zr_xFe_{11}V$ ($0 \leq x \leq 0.6$) alloys resulted to be positive. Although higher concentrations of Zr led to the formation of secondary phases such as $ZrFe_2$ and α-(Fe,V), the magnetic properties are still reasonables for permanent applications. For Zr = 0.6, the magnetic properties were $\mu_0 H_A$ = 8.8 T, M_s = 138 Am^2/kg and T_C = 310°C.

- An intergrain phase of La-rich was formed by performing different heat treatments to $(Sm_{0.12}Fe_{0.75}V_{0.13})_{98}La_2$ alloy. Although a uniform microstructure of 1-10 mm grains surrounded by a La-rich phase was obtained, the maximum $\mu_0 H_c$ was only 0.33 T. The different heat treatments allowed to suppress and to stabilize the $SmFe_2$. The $\mu_0 H_A$ was found to be consistently higher when the $SmFe_2$ phase was present in the alloy.

- Mechanical milling of stoichiometric $SmFe_{10}V_2$ alloy, led to a decomposition of the 1:12 into 1:7 structure. The $\mu_0 H_c$ increased continuously during milling up to a certain time, and then decreases. The highest $\mu_0 H_c$ value was found to be 0.21 T. After trying different heat treatments for the as-milled powders, the 1:12 phase was not formed.

- Following a controlled route of processing, nanocrystalline $Sm_{12}Fe_{73}V_{15}$ powders demonstrated $\mu_0 H_c$ values up to 1 T. The route of processing consisted of arc melting⟶homogenization of the 1:12→amorphization of the alloy by mechanical milling→ crystallization of the 1:12 phase using short heat treatments.

- One of the advantages of using the mechanical milling to obtain the powders instead of mechanical alloying was relatively short milling time. As the milled powder was already alloyed, and only a transformation of phase had to be induced mechanically, the milling time required to amorphization of the 1:12 phase was only 5 hours. Whereas the other authors [145] reported 60 h to obtain the same phase by mechanical alloying of blended elemental powders.

- Mechanical milling starting from the already alloyed materials favored to the formation of a well distributed amorphous matrix, which contributed later to the homogeneous formation of the 1:12 phase. Furthermore, the sizes of the nanograins could be appropriately controlled during the subsequent crystallizing process, which contributed to the improvement of the magnetic properties of the powders.

- The transformation from the amorphous phase into the tetragonal 1:12 phase depends critically on the annealing temperature and the sample composition. Milling in hexane does not facilitate the amorphization of this alloy, and it is more convenient the use of Ar.

- A bulk magnet based on Sm-Fe-V with 1:12 structure was successfully consolidated by hot pressing the mechanically milled $Sm_{12}Fe_{75}V_{13}$ powders. The density of the as-compacted

magnet reached a 92% of the theoretical density. The isotropic magnet exhibited a maximum $\mu_0 H_c$ of 1.06 T, $\mu_0 M_{3T}$ of 0.59 T, $\mu_0 M_r$ of 0.42 T and a $(BH)_{max}$ of 28 kJm^{-3} at 3 T applied field. The T_C was found to be 330°C and the temperature coefficients of remanent magnetization and coercivity, measured in the range of 0-100°C, were α = 0.14%C^{-1} and β = 0.39%C^{-1}, respectively, the latter was comparatively lower than that of NdFeB magnets.

- In the hot-deformed magnets, a small texture (≈ to 20%) perpendicular to the pressing direction was observed for $Sm_{12}Fe_{76.5}V_{11.5}$ and $Sm_{12}Fe_{73}V_{7.5}Mo_{7.5}$ magnets deformed at 1000 and 900°C, respectively. This type of texture is different from that of die-upset Nd-Fe-B magnets, and would indicate the use of hot extrusion rather than die-upsetting for the development of bulk magnets.

- The use of an small amount of Cu to substitute V in $Sm_{12}Fe_{74}V_{12}Cu_2$, slightly reduces the grain size, and results beneficial for the magnetic properties T_c = 362°C, $\mu_0 H_c$ = 0.96 T, $\mu_0 M_{3T}$ = 0.68 T (62 Am^{2}kg^{-1}) and $(BH)_{max}$ = 42kJm^{-3}. Substitution of Ti for V, does not change the magnetic properties. This fact can partly be related with the presence of the secondary phase Fe_2Ti, which is homogeneously distributed through the sample. Substitution of Mo favored the grain growth (≈ 1 mm) during the hot deformation, this had a detrimental influence on the T_c and $\mu_0 H_c$ which were 268°C and 0.45 T.

Appendix A

Conversion of Units

Table A.1 gives the conversion factors from the cgs unit to the SI unit. To convert a cgs unit to SI, multiply the cgs value by the conversion factor C.

Table A.1: Relation between commonly used units in magnetism (after Ref. [15]).

Quantity	Symbol	Gaussian & cgs emu[a]	Conversion factor C	SI & rationalized mks
Magnetic induction	B	gauss (G)	10^{-4}	tesla (T) Wb/m^2
Magnetic field strength	H	Oersted (Oe), Gb/cm	$10^3/4\pi$	A/m
(Volume) magnetization	M	emu/cm^3	10^3	A/m
(Volume) magnetization	$4\pi M$	G	$10^3/4\pi$	A/m
Magnetic Polarization	J, I	emu/cm^3	$4\pi \times 10^{-4}$	T, Wb/m^2
intensity of magnetization				
(Mass) magnetization	σ, M	emu/g	1	Am^2/kg
			$4\pi\times^{-7}$	Wb m/kg
Magnetic moment	m	emu, erg/G	10^{-3}	Am^2, J/T
Anisotropy constant	K	erg/cm^3	10^{-7}	MJ/m^3
Energy product	BH	MGOe	$10^2/4\pi$	kJ/m^3
Demagnetization factor	D, N	dimensionless	$1/4\pi$	dimensionless

[a] Gaussian units and cgs emu are the same for magnetic properties, and are based on $B = H + 4\pi M$
The upper one is recognized under SI and is based on $B = \mu_0(H + M)$ where $\mu_0 = 4\pi \times 10^{-7}$ H/m.
The lower one is not recognized under SI and is based on $B = \mu_0 H + J$.

Appendix B

Thermal coefficients

The Taylor expansion of second order of M_{r} around a T is given by

$$M_{\mathrm{r}}(T_0 + \Delta T) = |M_r|_{T_0} + \left.\frac{\mathrm{d}M_{\mathrm{r}}}{\mathrm{d}T}\right|_{T_0} \Delta T + \frac{1}{2} \left.\frac{\mathrm{d}^2 M_{\mathrm{r}}}{\mathrm{d}T^2}\right|_{T_0} (\Delta T)^2 \tag{B.1}$$

with $\Delta T = T - T_0$ and $(\Delta T)^2 = T^2 - 2T_0T + T_0^2$.
Reducing eq. B.1, M_{r} can be written as

$$M_{\mathrm{r}(T)} = a_{\mathrm{r}}T^2 + b_{\mathrm{r}}T + c_{\mathrm{r}}, \tag{B.2}$$

where a_{r}, b_{r} and c_{r} are the regression coefficients of the quadratic function. For T_1 and T_2, M_{r} can be expressed as

$$M_{\mathrm{r}(T_1)} = a_{\mathrm{r}}T_1^2 + b_{\mathrm{r}}T_1 + c_{\mathrm{r}} \tag{B.3}$$

and

$$M_{\mathrm{r}(T_2)} = a_{\mathrm{r}}T_2^2 + b_{\mathrm{r}}T_2 + c_{\mathrm{r}} \tag{B.4}$$

respectively. Subtracting eq. B.3 from eq. B.4,

$$
\begin{aligned}
M_{\mathrm{r}(T_2)} - M_{\mathrm{r}(T_1)} &= a_r(T_2^2 - T_1^2) + b_r(T_2 - T_1) \\
M_{\mathrm{r}(T_2)} - M_{\mathrm{r}(T_1)} &= a_r(T_2 - T_1)(T_2 + T_1) + b_r(T_2 - T_1) \\
\frac{M_{\mathrm{r}(T_2)} - M_{\mathrm{r}(T_1)}}{(T_2 - T_1)} &= a_r(T_2 + T_1) + b_r \\
\frac{M_{\mathrm{r}(T_2)} - M_{\mathrm{r}(T_1)}}{M_{r(T_1)}} \frac{1}{\Delta T} &= \frac{a_r(T_2 + T_1) + b_r}{M_{r(T_1)}}
\end{aligned}
\tag{B.5}
$$

then, the α coefficient is

$$
\alpha = \frac{a_{\mathrm{r}}(T_2 - T_1) + b_{\mathrm{r}}}{M_{\mathrm{r}(T_1)}}. \tag{B.6}
$$

Following the same procedure one can obtain,

$$
\beta = \frac{a_{\mathrm{c}}(T_2 + T_1) + b_{\mathrm{c}}}{\mu_0 H_{\mathrm{c}(T_1)}}. \tag{B.7}
$$

Appendix C

Physical properties of different elements

Physical properties of some elements used in this work after Ref. [146]

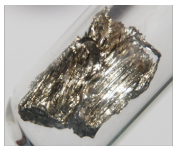

Samarium	
Electron configuration	[Xe] 4f6 6s2
Melting point	1345 K (1072°C)
Boiling point	2173 K (1900°C)
Density (near RT)	7.52 g/cm^3
Heat of vaporization	192 kJ/mol
Atomic radius	180 pm
Oxidation states Electronegativity	+1, +2, +3, +4 (1.17)
Magnetic ordering	Paramagnetic

Vapor pressure						
P (Pa)	1	10	100	1 k	10 k	100 k
at T (K)	1001	1106	1240	(1421)	(1675)	(2061)

Iron	
Electron configuration	[Ar] 3d^6 4s^2
Melting point	1811 K (1538°C)
Boiling point	3134 K (2862°C)
Density (near RT)	7.874 g/cm^3
Heat of vaporization	340 kJ/mol
Atomic radius	126 pm
Oxidation states Electronegativity	−4, −2, −1, +1, +2, +3, +4, +5, +6, +7, (1.83)
Curie temperature	1043 K (770°C)

Vapor pressure						
P (Pa)	1	10	100	1 k	10 k	100 k
at T (K)	1728	1890	2091	2346	2679	3132

Vanadium	
Electron configuration	[Ar] 3d^3 4s^2
Melting point	2183 K (1910°C)
Boiling point	3680 K (3407°C)
Density (near RT)	6.0 g/cm^3
Heat of vaporization	444 kJ/mol
Atomic radius	134 pm
Oxidation states Electronegativity	−3, −1, +1, +2, +3, +4, +5 (1.63)
Magnetic ordering	Paramagnetic

Vapor pressure						
P (Pa)	1	10	100	1 k	10 k	100 k
at T (K)	2101	2289	2523	2814	3187	3679

Appendix D

Supplementary plots of chapter 3

D.1 X-ray diffraction patterns of $Sm_{1-x}Zr_xFe_{11}V$

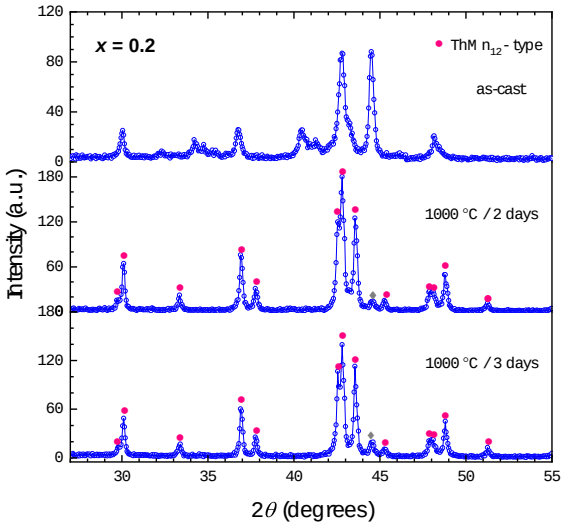

Figure D.1: XRD patterns of $Sm_{0.2}Zr_{0.2}Fe_{11}V$ heat-treated alloys.

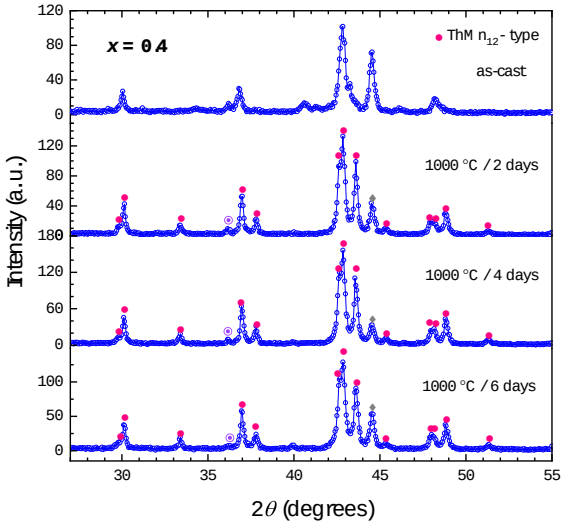

Figure D.2: XRD patterns of $Sm_{0.6}Zr_{0.4}Fe_{11}V$ heat-treated alloys.

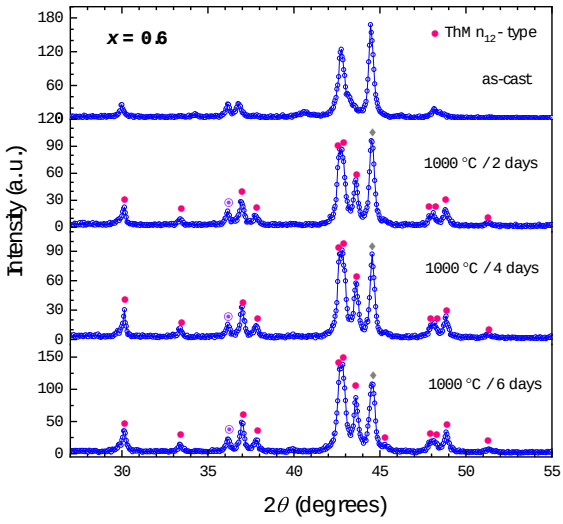

Figure D.3: XRD patterns of $Sm_{0.4}Zr_{0.6}Fe_{11}V$ heat-treated alloys.

List of Publications

- G. C. Hadjipanayis, A. M. Gabay, A. M. Schönhöbel, A. Martn-Cid, J. M.Barandiaran, D. Niarchos, $ThMn_{12}$-Type Alloys for Permanent Magnets, *Engineering*, (2019). https://doi.org/10.1016/j.eng.2018.12.011

- A. M. Schönhöbel, R. Madugundo, A. M. Gabay, J. M. Barandiarn, G. C. Hadjipanayis, The Sm-Fe-V based 1:12 bulk magnets, *J. Alloys Compd.*, 791, 11221127 (2019). https://doi.org/10.1016/j.jallcom.2019.03.249

- J. M. Barandiaran, A. Martin-Cid, A. M. Schönhöbel, J. S. Garitaonandia, M. Gjoka, D. Niarchos, S. Makridis, A. Paski, A. Aubert, F. Mazaleyrat, G. C. Hadjipanayis, Nitrogenation and sintering of (Nd-Zr)$Fe_{10}Si_2$ tetragonal compounds for permanent magnets applications, *J. Alloys Compd.*, 784, 9961002 (2019). https://doi.org/10.1016/j.jallcom.2019.01.044

- A. M. Schönhöbel, R. Madugundo, O. Y. Vekilova, O. Eriksson, H. C. Herper, J. M. Barandiarn, G. C. Hadjipanayis, Intrinsic magnetic properties of $SmFe_{12-x}V_x$ alloys with reduced V-concentration, *J. Alloys Compd.*, 786, 969974 (2019). https://doi.org/10.1016/j.jallcom.2019.01.332

- A. Martin-Cid, D. Salazar, A. M. Schönhöbel, J. S. Garitaonandia, J. M. Barandiaran, G. C. Hadjipanayis, Magnetic properties and phase stability of tetragonal $Ce_{1-x}Sm_xFe_9Co_2Ti$ 1:12 phase for permanent magnets, *J. Alloys Compd.*, 749, 640644 (2018). https://doi.org/10.1016/j.jallcom.2018.03.325

- R. Madugundo, N. V. Rama Rao, A. M. Schönhöbel, D. Salazar, A. A. El-Gendy, Recent Developments in Nanostructured Permanent Magnet Materials and Their Process-

ing Methods. In Magnetic Nanostructured Materials (pp. 157198) (2018). Elsevier. https://doi.org/10.1016/B978-0-12-813904-2.00006-1

Bibliography

[1] S. Massari and M. Ruberti, "Rare earth elements as critical raw materials: Focus on international markets and future strategies," *Resources Policy*, vol. 38, no. 1, pp. 36–43, 2013.

[2] EU Commission, "Study on the review of the list of critical raw materials," *European Comissmion*, no. June, p. 93, 2017.

[3] O. Gutfleisch, "Controlling the properties of high energy density permanent magnetic materials by different processing," *J. Phys. D: Appl. Phys.*, vol. 33, pp. 157–172, 2000.

[4] J. Coey, P. Stamenov, S. Porter, M. Venkatesan, R. Zhang, and T. Iriyama, "Sm-Fe-N revisited; remanence enhancement in melt-spun Nitroquench material," *Journal of Magnetism and Magnetic Materials*, vol. 480, pp. 186 – 192, 2019.

[5] J. Cui, J. P. Choi, G. Li, E. Polikarpov, J. Darsell, N. Overman, M. Olszta, D. Schreiber, M. Bowden, T. Droubay, M. J. Kramer, N. A. Zarkevich, L. L. Wang, D. D. Johnson, M. Marinescu, I. Takeuchi, Q. Z. Huang, H. Wu, H. Reeve, N. V. Vuong, and J. P. Liu, "Thermal stability of MnBi magnetic materials," *Journal of Physics: Condensed Matter*, vol. 26, p. 064212, jan 2014.

[6] T. Ohtani, N. Kato, S. Kojima, K. Kojima, Y. Sakamoto, I. Konno, M. Tsukahara, and T. Kubo, "Magnetic properties of Mn-Al-C permanent magnet alloys," *IEEE Transactions on Magnetics*, vol. 13, pp. 1328–1330, sep 1977.

[7] H. Kronmüller and M. Fahnle, *Micromagnetism and the Microstructure of Ferromagnetic Solids*. Cambridge University Press, UK, 2003.

[8] A. M. Gabay and G. C. Hadjipanayis, "Recent development earth-lean/free permanent magnetst," Presented in International Conference on Fine Particle Magnetism, Gijón, Spain, 2019.

[9] "Element scarcity-euchems periodic table." `http://www.euchems.eu/euchems-periodic-table/`. Accessed: 2019-07-04.

[10] S. Sugimoto, T. Shimono, H. Nakamura, T. Kagotani, M. Okada, and M. Homma, "Phase Relation of Sm-Fe-V Alloys around the Compound $Sm_3(Fe,V)_{29}$," *Materials Transactions, JIM*, vol. 37, no. 3, pp. 494–498, 1996.

[11] J. M. D. Coey, *Magnetism of localized electrons on the atom*, p. 97127. Cambridge University Press, 2010.

[12] "Comparison of comprehensive performances of various permanent magnets." `http://www.meank-magnet.com/uploads/file/various-permanent-magnets-comparison.pdf`. Accessed: 2019-05-29.

[13] "Rare earth metals." `http://mineralprices.com/rare-earth-metals/`. Accessed: 2019-07-04.

[14] L. Bessais and C. Djega-Mariadassou, "Structure and magnetic properties of nanocrystalline $Sm(Fe_{1-x}Co_x)_{11}Ti$ ($x \leq 2$)," *Physical Review B*, vol. 63, no. January, p. 054412, 2001.

[15] R. B. Goldfarb and F. R. Fickett, "Units for Magnetic Properties," *U.S. Department of Commerce, National Bureau of Standards Publication, Boulder, Colorado*, vol. 696, p. 1, 1985.

[16] T. Mishima, "Nickel-aluminum steel for permanent magnets," *Stahl U. Eisen.*, vol. 53, p. 79, 1931.

[17] R. McCurrie, "Chapter 3 The structure and properties of alnico permanent magnet alloys," in *Ferromagnetic Materials* (E. P. Wohlfarth, ed.), vol. 3, ch. The Struct, pp. 107–188, Amsterdam: North Holland: Elsevier, 1982.

[18] J. J. Went, G. W. Rathenau, E. W. Gorter, and G. W. Van Oosterhout, "Ferroxdure, a Class of New Permanent Magnet Materials," *Philips Tech. Rev.*, vol. 13, pp. 194–208, 1952.

[19] G. C. Hadjipanayis, R. C. Hazelton, and K. R. Lawless, "New iron-rare-earth based permanent magnet materials," *Applied Physics Letters*, vol. 43, no. 8, pp. 797–799, 1983.

[20] J. J. Croat, J. F. Herbst, R. W. Lee, and F. E. Pinkerton, "High-energy product Nd-Fe-B permanent magnets," *Applied Physics Letters*, vol. 44, pp. 148–149, jan 1984.

[21] J. J. Croat, J. F. Herbst, R. W. Lee, and F. E. Pinkerton, "Pr-Fe and Nd-Fe-based materials: A new class of high-performance permanent magnets (invited)," *Journal of Applied Physics*, vol. 55, pp. 2078–2082, mar 1984.

[22] M. Sagawa, S. Fujimura, N. Togawa, H. Yamamoto, and Y. Matsuura, "New Material for Permanent Magnets on a Base of Nd and Fe," *Journal of Applied Physics*, vol. 55, pp. 2083–2087, 1984.

[23] KHJ Buschow, "Intermetallic compounds of rare-earth and 3d transition metals," *Reports on Progress in Physics*, vol. 40, no. 10, pp. 1179–1256, 1977.

[24] L. Baczewski, D. Givord, J. Alameda, B. Dieny, J. Nozieres, J. Rebouillat, and J. Prejean, "Magnetism in Rare-Earth-Transition Metal Systems. Magnetization Reversal and Ultra-High Susceptibility in Sandwiched Thin Films Based on Rare-earth and Cobalt Alloys," *Acta Physica Polonica A*, vol. 83, pp. 629–641, may 1993.

[25] K. H. J. Buschow, "Intermetallic compounds of rare earth elements and Ni, Co, or Fe," *Physica Status Solidi (a)*, vol. 7, pp. 199–210, sep 1971.

[26] J. F. Herbst and J. W. Wilkins, "Relativistic calculations of 3d excitation energies in the rare-earth metals," *Phys. Rev. B*, vol. 20, pp. 2999–3005, Oct 1979.

[27] L. D. Landau, E. M. Lifshitz, and L. P. Pitaevski, *Electrodynamics of Continuous Media. Vol. 8 in Course of Theoretical Physics.* Elsevier, second ed., 1984 (First published in 1960).

[28] H.-S. Li and J. Coey, "Chapter 1 Magnetic properties of ternary rare-earth transition-metal compounds," in *Handbook of Magnetic Materials*, vol. 6, pp. 1–83, Elsevier, 1991.

[29] C. Tannous and J. Gieraltowski, "The Stoner-Wohlfarth model of ferromagnetism," *European Journal of Physics*, vol. 29, pp. 475–487, mar 2008.

[30] H. Krönmuller and M. Sagawa, "Analysis of the magnetic hardening mechanism in RE-FeB permanent magnets," *Journal of Magnetism and Magnetic Materials*, vol. 74, pp. 291–302, 1988.

[31] J. D. Livingston, "Magnetic domains in sintered Fe-Nd-B magnets," *Journal of Applied Physics*, vol. 57, no. 8, pp. 4137–4139, 1985.

[32] T. Inoue, K. Goto, and T. Sakurai, "Magnetic Domains of Single-Domain Particles of $SmCo_5$ Observed by the Colloid-SEM Method," *Japanese Journal of Applied Physics*, vol. 22, pp. L695–L697, nov 1983.

[33] C. Yang, L. Jia, S. Wang, C. Gao, D. Shi, Y. Hou, and S. Gao, "Single Domain $SmCo_5$-Co Exchange-coupled Magnets Prepared from Core/shell $Sm[Co(CN)_6]\cdot 4H_2O$-GO Particles: A Novel Chemical Approach," *Scientific Reports*, vol. 3, p. 3542, Dec 2013.

[34] K. Buschow, "Permanent magnet materials based on tetragonal rare earth compounds of the type $RFe_{12-x}M_x$," *Journal of Magnetism and Magnetic Materials*, vol. 100, pp. 79–89, nov 1991.

[35] A. Gabay and G. Hadjipanayis, "Recent developments in RFe_{12}-type compounds for permanent magnets," *Scripta Materialia*, vol. 154, pp. 284–288, sep 2018.

[36] R. Madugundo, N. V. R. Rao, A. M. Schönhöbel, D. Salazar, and A. A. El-Gendy, "Recent Developments in Nanostructured Permanent Magnet Materials and Their Processing Methods," in *Magnetic Nanostructured Materials: From Lab to Fab* (A. El-Gendy, J. M. Barandiaran, and R. L. Hadimani, eds.), ch. 6, pp. 157–198, Amsterdam: Elsevier, 1st ed., 2018.

[37] J. V. Florio, R. E. Rundle, and A. I. Snow, "Compounds of thorium with transition metals. I. The thoriummanganese system," *Acta Crystallographica*, vol. 5, no. 4, pp. 449–457, 1952.

[38] W. Haije, J. Spijkerman, F. De Boer, K. Barker, and K. Buschow, "Magnetic structure of rare earth compounds of the type $RFe_{10}V_2$," *Journal of the Less Common Metals*, vol. 162, pp. 285–295, sep 1990.

[39] W. Suski, "The $ThMn_{12}$-Type compounds of rare earths and actinides: Structure, magnetic and related properties," in *Handbook on the physics and chemistry of rare earths*

(K. A. Gschneidner and L. J. Eyring, eds.), vol. 22, pp. 143–294, Amsterdam: Elsevier, 1996.

[40] A. Niessen, F. de Boer, R. Boom, P. de Châtel, W. Mattens, and A. Miedema, "Model predictions for the enthalpy of formation of transition metal alloys II," *Calphad*, vol. 7, pp. 51–70, jan 1983.

[41] K. H. J. Buschow, "Structure and properties of some novel ternary Fe-rich rare-earth intermetallics (invited)," *Journal of Applied Physics*, vol. 63, pp. 3130–3135, apr 1988.

[42] K. Ohashi, Y. Tawara, R. Osugi, and M. Shimao, "Magnetic properties of Fe-rich rare-earth intermetallic compounds with a $ThMn_{12}$ structure," *Journal of Applied Physics*, vol. 64, pp. 5714–5716, nov 1988.

[43] X. C. Kou, R. Grössinger, and G. Wiesinger, "Intrinsic magnetic properties of $RFe_{10}Mo_2$ compounds (R = Y, Pr, Nd, Sm, Gd, Tb, Dy, Ho, Er, or Tm)," *Physical Review B*, vol. 51, no. 13, pp. 8254–8265, 1995.

[44] M. Solzi, L. Pareti, O. Moze, and W. I. F. David, "Magnetic anisotropy and crystal structure of intermetallic compounds of the $ThMn_{12}$ structure," *Journal of Applied Physics*, vol. 64, pp. 5084–5087, nov 1988.

[45] Y.-c. Yang, X.-d. Zhang, L.-s. Kong, Q. Pan, S.-l. Ge, J.-l. Yang, Y.-f. Ding, B.-s. Zhang, C.-t. Ye, and L. Jin, "Neutron diffraction study of the nitride $YTiFe_{11}N_x$," *Solid State Communications*, vol. 78, pp. 313–316, apr 1991.

[46] Y. Wang, G. Hadjipanayis, A. Kim, D. Sellmyer, and W. Yelon, "Structure and magnetic properties of $RFe_{10}V_2N_x$ compounds," *Journal of Magnetism and Magnetic Materials*, vol. 104-107, pp. 1132–1134, feb 1992.

[47] O. Isnard, S. Miraglia, M. Guillot, and D. Fruchart, "Hydrogen effects on the magnetic properties of $RFe_{11}Ti$ compounds," *journal of alloys and compounds*, vol. 275-277, pp. 637–641, 1998.

[48] T. Sinnemann, K. Erdmann, M. Rosenberg, and K. H. J. Buschow, "A Mössbauer and NMR spectroscopy study of $RFe_{12-x}M_x$ intermetallics," *Hyperfine Interactions*, vol. 50, pp. 675–683, jun 1989.

[49] J. Rubín, J. Garitaonandia, J. Bartolomé, M. Barandiarán, E. Palacios, D. Fruchart, and S. Miraglia, "A comparison of Mössbauer spectroscopy and neutron diffraction studies of the preferential site occupation of Co in $ErFe_{10.4-x}Co_xMo_{1.6}$," *Solid State Communications*, vol. 106, no. 12, pp. 821 – 826, 1998.

[50] K. Ohashi, T. Yokoyama, R. Osugi, and Y. Tawara, "THE MAGNETIC AND STRUCTURAL PROPERTIES OF R-Ti-Fe TERNARY COMPOUNDS," *IEEE Transactions on Magnetics*, vol. 23, no. 5, pp. 3101–3103, 1987.

[51] K. E. N. Ohashi, Y. Tawara, and R. Osugi, "Identification of the intermetallic compound consisting of Sm, Ti, Fe," *Journal of The Less-Common Metals*, vol. 139, pp. L1–L5, 1988.

[52] S. A. Nikitin, I. S. Tereshina, T. Ivanova, and Y. F. Popov, "Magnetic properties of $SmFe_{11-x}Co_xTi$ monocrystal compounds," *NEWS. ISKCON. CEP*, vol. 3, no. 2, pp. 69–73, 1996.

[53] F. De Boer, Y.-K. Huang, D. De Mooij, and K. Buschow, "Magnetic properties of a series of novel ternary intermetallics ($RFe_{10}V_2$)," *Journal of the Less Common Metals*, vol. 135, pp. 199–204, nov 1987.

[54] D. De Mooij and K. Buschow, "Some novel ternary $ThMn_{12}$-type compounds," *Journal of the Less Common Metals*, vol. 136, pp. 207–215, jan 1988.

[55] E. W. Singleton, J. Strzeszewski, G. C. Hadjipanayis, and D. J. Sellmyer, "Magnetic and structural properties of melt-spun rare-earth transition-metal intermetallics with ThMn12 structure," *Journal of Applied Physics*, vol. 64, pp. 5717–5719, nov 1988.

[56] F. E. Pinkerton, C. D. Fuerst, and J. F. Herbst, "Nitriding of melt-spun Nd-Fe-Mo alloys," *Journal of Applied Physics*, vol. 75, no. 10, pp. 6015–6017, 1994.

[57] M. Okada, A. Kojima, K. Yamagishi, and M. Homma, "High coercivity in melt-spun $SmFe_{10}(Ti,M)_2$ ribbons (M=V/Cr/Mn/Mo)," *IEEE Transactions on Magnetics*, vol. 26, no. 5, p. 1376, 1990.

[58] X. Kou, E. Sinnecker, R. Grössinger, G. Wiesinger, T. Zhao, J. Liu, and F. de Boer, "Magnetocrystalline anisotropy of $SmFe_{12-x}Mo_x$ compounds with x = 0.5, 1.0, 1.5, 2.0 or 3.0," *Journal of Magnetism and Magnetic Materials*, vol. 140-144, pp. 1025–1026, feb 1995.

[59] Y. Z. Wang and G. C. Hadjipanayis, "Effect of nitrogen on the structural and magnetic properties of intermetallic compounds with the $ThMn_{12}$ structure," *Journal of Applied Physics*, vol. 70, pp. 6009–6011, nov 1991.

[60] Y.-c. Yang, X.-d. Zhang, S.-l. Ge, Q. Pan, L.-s. Kong, H. Li, J. Yang, B. Zhang, Y. Ding, and C. Ye, "Magnetic and crystallographic properties of novel Fe-rich rare-earth nitrides of the type $RTiFe_{11}N_{1-\delta}$ (invited)," *Journal of Applied Physics*, vol. 70, pp. 6001–6005, nov 1991.

[61] L. X. Liao, Z. Altounian, and D. H. Ryan, "Structure and magnetic properties of $RFe_{11}TiN_x$ (R = Y, Sm, and Dy)," *Journal of Applied Physics*, vol. 70, pp. 6006–6008, nov 1991.

[62] J. Hu, T. Wang, S. Zhang, Y. Wang, and Z. Wang, "Structure and magnetic properties of RTi1.1Fe10.9," *Journal of Magnetism and Magnetic Materials*, vol. 74, pp. 22–26, aug 1988.

[63] S. A. Nikitin, I. S. Tereshina, E. A. Ovtchenkov, V. N. Verbetsky, and A. A. Salamova, "Effect Of Interstitial Hydrogen and Nitrogen on the Magnetocrystalline Anisotropy and Magnetostriction of Rare-Earth-Transition-Metal Intermetallics," in *Hydrogen Materials Science and Chemistry of Metal Hydrides*, vol. 74(1), pp. 23–33, Dordrecht: Springer Netherlands, aug 2002.

[64] Q. Pan, Z. Liu, and Y. Yang, "Structural and magnetic properties of $Ce(Fe,M)_{12}N_x$ interstitial compounds, M = Ti, V, Cr, and Mo," *Journal of Applied Physics*, vol. 76, pp. 6728–6730, nov 1994.

[65] W. Mao, B. Cheng, J. Yang, X. Pei, and Y. Yang, "Synthesis and characterization of hard magnetic materials: $PrFe_{10.5}V_{1.5}N_x$," *Applied Physics Letters*, vol. 70, no. 22, pp. 3044–3046, 1997.

[66] M. Anagnostou, C. Christides, M. Pissas, and D. Niarchos, "Preparation and characterization of the $NdFe_{10}T_2N_x$ (T = Mo, V) compounds with the $ThMn_{12}$ tetragonal-type structure," *Journal of Applied Physics*, vol. 70, no. 10, pp. 21–24, 1991.

[67] Y. Z. Wang, B. P. Hu, X. L. Rao, G. C. Liu, L. Yin, W. Y. Lai, W. Gong, and G. C. Hadjipanayis, "Structural and magnetic properties of $NdFe_{12-x}Mo_xN_{1-\delta}$ compounds," *Journal of Applied Physics*, vol. 73, pp. 6251–6253, may 1993.

[68] K. Y. Guslienko, E. H. C. P. Sinnecker, and R. Grossinger, "Magnetic anisotropy and magnetic phase transitions in $RFe_{10}Mo_2$ (R= Pr, Nd, Sm, Dy, Ho, Er, Tm)," *Physical Review B*, vol. 55, pp. 380–388, jan 1997.

[69] D. Goll, R. Loeffler, R. Stein, U. Pflanz, S. Goeb, R. Karimi, and G. Schneider, "Temperature dependent magnetic properties and application potential of intermetallic $Fe_{11-x}Co_xTiCe$," *Phys. Status Solidi RRL*, vol. 8, no. 10, pp. 862–865, 2014.

[70] A. M. Gabay, A. Martín-Cid, J. M. Barandiaran, D. Salazar, and G. C. Hadjipanayis, "Low-cost $Ce_{1-x}Sm_x(Fe,Co,Ti)_{12}$ alloys for permanent magnets," *AIP Advances*, vol. 6, no. 5, p. 056015, 2016.

[71] H. Wuest, L. Bommer, A. M. Huber, D. Goll, T. Weissgaerber, and B. Kieback, "Preparation of nanocrystalline $Ce_{1-x}Sm_x(Fe,Co)_{11}Ti$ by melt spinning and mechanical alloying," *Journal of Magnetism and Magnetic Materials*, vol. 428, no. December 2016, pp. 194–197, 2017.

[72] C. P. Wang, Y. Hu, S. Y. Yang, Y. Lu, Q. W. Jiang, and X. J. Liu, "Experimental Investigation of Phase Equilibria in the Fe-Si-Zr Ternary System," *Journal of Phase Equilibria and Diffusion*, vol. 34, pp. 277–288, Aug 2013.

[73] A. M. Gabay, R. Cabassi, S. Fabbrici, F. Albertini, and G. C. Hadjipanayis, "Structure and permanent magnet properties of $Zr_{1-x}R_xFe_{10}Si_2$ alloys with R = Y, La, Ce, Pr and Sm," *Journal of Alloys and Compounds*, vol. 683, pp. 271–275, 2016.

[74] M. Gjoka, V. Psycharis, E. Devlin, D. Niarchos, and G. Hadjipanayis, "Effect of Zr substitution on the structural and magnetic properties of the series $Nd_{1-x}Zr_xFe_{10}Si_2$ with the $ThMn_{12}$ type structure," *Journal of Alloys and Compounds*, vol. 687, pp. 240–245, 2016.

[75] A. M. Gabay and G. C. Hadjipanayis, "$ThMn_{12}$-type structure and uniaxial magnetic anisotropy in $ZrFe_{10}Si_2$ and $Zr_{1-x}Ce_xFe_{10}Si_2$ alloys," *Journal of Alloys and Compounds*, vol. 657, pp. 133–137, 2016.

[76] S. Sakurada, A. Tsutai, and M. Sahashi, "A study on the formation of $ThMn_{12}$ and $NaZn_{13}$ structures in $RFe_{10}Si_2$," *Journal of Alloys and Compounds*, vol. 187, pp. 67–71, aug 1992.

[77] D. Wang, S. Liou, P. He, D. J. Sellmyer, G. Hadjipanayis, and Y. Zhang, "$SmFe_{12}$ and $SmFe_{12}N_x$, films fabricated by sputtering," *Journal of Magnetism and Magnetic Materials*, vol. 124, pp. 62–68, 1993.

[78] H. Sun, T. Tomida, and S. Hirosawa, "Magnetic properties and microstructure studies of Sm-Fe magnetic thin films Magnetic properties and microstructure studies of Sm-Fe magnetic thin films," *Journal of Applied Physics*, vol. 328, pp. 328–334, 1997.

[79] Y. Hirayama, Y. K. Takahashi, S. Hirosawa, and K. Hono, "Intrinsic hard magnetic properties of $Sm(Fe_{1-x}Co_x)_{12}$ compound with the $ThMn_{12}$ structure," *Scripta Materialia*, vol. 138, pp. 62–65, sep 2017.

[80] T. Sato, T. Ohsuna, M. Yano, A. Kato, and Y. Kaneko, "Permanent magnetic properties of $NdFe_{12}N_x$ sputtered films epitaxially grown on V buffer layer," *Journal of Applied Physics*, vol. 122, p. 053903, aug 2017.

[81] R. M. German, *A-Z of Powder Metallurgy*. Elsevier, 2005.

[82] R. K. Mishra, "Microstructure of hot-pressed and die-upset NdFeB magnets," *Journal of Applied Physics*, vol. 62, pp. 967–971, aug 1987.

[83] R. A. Brand, *NORMOS-90 Users Manual*. D-47048, Duisburg: Laboratorium für Angewandte Physik, Universität Duisburg, 2002.

[84] C. Zhou, F. E. Pinkerton, and J. F. Herbst, "Magnetic properties of $CeFe_{11-x}Co_xTi$ with $ThMn_{12}$ structure," *Journal of Applied Physics*, vol. 115, p. 17C716, may 2014.

[85] S. Suzuki, T. Kuno, K. Urushibata, K. Kobayashi, N. Sakuma, K. Washio, H. Kishimoto, A. Kato, and A. Manabe, "A $(Nd,Zr)(Fe,Co)_{11.5}Ti_{0.5}N_x$ compound as a permanent magnet material," *AIP Advances*, vol. 4, p. 117131, nov 2014.

[86] S. Suzuki, T. Kuno, K. Urushibata, K. Kobayashi, N. Sakuma, K. Washio, M. Yano, A. Kato, and A. Manabe, "A new magnet material with ThMn12 structure: $(Nd_{1-x}Zr_x)(Fe_{1-y}Co_y)_{11+z}Ti_{1-z}N_\alpha(\alpha = 0.6 - 1.3)$," *Journal of Magnetism and Magnetic Materials*, vol. 401, pp. 259–268, mar 2016.

[87] P. Tozman, H. Sepehri-Amin, Y. K. Takahashi, S. Hirosawa, and K. Hono, "Intrinsic magnetic properties of $Sm(Fe_{1-x}Co_x)_{11}Ti$ and Zr-substituted $Sm_{1-y}Zr_y(Fe_{0.8}Co_{0.2})_{11.5}Ti_{0.5}$compounds with $ThMn_{12}$ structure toward the development of permanent magnets," *Acta Materialia*, vol. 153, pp. 354–363, 2018.

[88] C. Zhou, D. Haddad, R. S. Kukreja, F. E. Pinkerton, K. Sun, and M. J. Kramer, "Magnetic hardening of CeFe11Ti and the effect of TiC addition," *IEEE Transactions on Magnetics*, vol. 51, no. 4, pp. 4–7, 2015.

[89] R. Verhoef, F. de Boer, Z. Zhi-dong, and K. Buschow, "Moment reduction in $RFe_{12-x}T_x$ compounds (R = Gd, Y and T = Ti, Cr, V, Mo, W)," *Journal of Magnetism and Magnetic Materials*, vol. 75, pp. 319–322, dec 1988.

[90] X. Zhong, F. de Boer, D. de Mooij, and K. Buschow, "Magnetic coupling in the tetragonal rare earth iron compounds of the type $R(Fe,V)_{12}$," *Journal of the Less Common Metals*, vol. 163, pp. 123–132, oct 1990.

[91] J. Yang, S.-z. Dong, Y.-c. Yang, and B.-p. Cheng, "Structural and magnetic properties of $RFe_{10.5}V_{1.5}N_x$," *Journal of Applied Physics*, vol. 75, pp. 3013–3016, mar 1994.

[92] H. Du, J. Han, W. Zhang, C. Wang, W. Wang, S. Liu, H. Chen, X. Zhang, and Y. Yang, "Determination of the zirconium site in zirconium-substituted $Nd(Fe,Mo,Zr)_{12}$ compounds," *Journal of Magnetism and Magnetic Materials*, vol. 283, pp. 316–321, dec 2004.

[93] N. Sakuma, S. Suzuki, T. Kuno, K. Urushibata, K. Kobayashi, M. Yano, A. Kato, and A. Manabe, "Influence of Zr substitution on the stabilization of $ThMn_{12}$-type $(Nd_{1-\alpha}Zr_{\alpha})(Fe_{0.75}Co_{0.25})_{11.25}Ti_{0.75}N_{1.2-1.4}$ ($\alpha = 0 - 0.3$) compounds," *AIP Advances*, vol. 6, p. 056023, may 2016.

[94] A. Martin-Cid, D. Salazar, A. Schönhöbel, J. Garitaonandia, J. Barandiaran, and G. Hadjipanayis, "Magnetic properties and phase stability of tetragonal $Ce_{1-x}Sm_xFe_9Co_2Ti$ 1:12 phase for permanent magnets," *Journal of Alloys and Compounds*, vol. 749, pp. 640–644, jun 2018.

[95] J. J. Garitaonandia-Saiz, *La espectroscopia Mössbauer en el estudio de transiciones y transformaciones de fase magnéticas.* PhD thesis, Universidad del Pais Vasco, March 1998.

[96] C. Denissen, R. Coehoorn, and K. Buschow, "^{57}Fe Mössbauer study of $RFe_{12-x}T_x$ compounds (T = V, Cr, Mo)," *Journal of Magnetism and Magnetic Materials*, vol. 87, pp. 51–56, jun 1990.

[97] N. N. Greenwood and A. Earnshaw, *Chemistry of the Elements.* Butterworth-Heinemann, second ed., 1997.

[98] T. Fukazawa, H. Akai, Y. Harashima, and T. Miyake, "First-principles Study of Intersite Magnetic Couplings and Curie Temperature in $RFe_{12-x}Cr_x$(R = Y, Nd, Sm)," *Journal of the Physical Society of Japan*, vol. 87, p. 044706, apr 2018.

[99] K. D. Durst and H. Kronmüller, "Determination of intrinsic magnetic material parameters of $Nd_2Fe_{14}B$ from magnetic measurements of sintered $Nd_{15}Fe_{77}B_8$ magnets," *Journal of Magnetism and Magnetic Materials*, vol. 59, pp. 86–94, may 1986.

[100] S. K. Pal, K. P. Skokov, T. Groeb, S. Ener, and O. Gutfleisch, "Properties of magnetically semi-hard (FexCo1-x)3B compounds," *Journal of Alloys and Compounds*, vol. 696, pp. 543–547, 2017.

[101] R. Grössinger, R. Krewenka, and K. H. J. Buschow, "Note on the anisotropy fields in tetragonal $RFe_{10}V_2$ compounds," *Journal of Alloys and Compounds*, vol. 186, no. 2, pp. 11–15, 1992.

[102] K. Buschow, "Chapter 4 Magnetism and processing of permanent magnet materials," in *Handbook of Magnetic Materials*, vol. 10, pp. 463–593, Elsevier Science, 1997.

[103] R. Helmholdt, J. Vleggaar, and K. Buschow, "Note on the crystallographic and magnetic structure of $YFe10V_2$," *Journal of the Less Common Metals*, vol. 138, pp. L11–L14, mar 1988.

[104] R. Helmholdt, J. Vleggaar, and K. Buschow, "Crystallographic and magnetic structure of $TbFe_{10}V_2$ and $ErFe_{10}V_2$," *Journal of the Less Common Metals*, vol. 144, pp. 209–214, dec 1988.

[105] G. Kresse and J. Hafner, "Ab initio molecular dynamics for open-shell transition metals," *Physical Review B*, vol. 48, pp. 13115–13118, nov 1993.

[106] G. Kresse and J. Furthmüller, "Efficiency of ab-initio total energy calculations for metals and semiconductors using a plane-wave basis set," *Computational Materials Science*, vol. 6, pp. 15–50, jul 1996.

[107] G. Kresse and J. Furthmüller, "Efficient iterative schemes for ab initio total-energy calculations using a plane-wave basis set," *Physical Review B*, vol. 54, pp. 11169–11186, oct 1996.

[108] P. E. Blöchl, "Projector augmented-wave method," *Physical Review B*, vol. 50, pp. 17953–17979, dec 1994.

[109] J. P. Perdew, K. Burke, and M. Ernzerhof, "Generalized Gradient Approximation Made Simple," *Physical Review Letters*, vol. 77, pp. 3865–3868, oct 1996.

[110] H. J. Monkhorst and J. D. Pack, "Special points for Brillouin-zone integrations," *Physical Review B*, vol. 13, pp. 5188–5192, jun 1976.

[111] J. M. Wills and B. R. Cooper, "Synthesis of band and model Hamiltonian theory for hybridizing cerium systems," *Physical Review B*, vol. 36, pp. 3809–3823, sep 1987.

[112] J. M. Wills, O. Eriksson, P. Andersson, A. Delin, O. Grechnyev, and M. Alouani, *Full-Potential Electronic Structure Method*, vol. 167 of *Springer Series in Solid-State Sciences*. Berlin, Heidelberg: Springer Berlin Heidelberg, 2010.

[113] P. E. Blöchl, O. Jepsen, and O. K. Andersen, "Improved tetrahedron method for Brillouin-zone integrations," *Physical Review B*, vol. 49, pp. 16223–16233, jun 1994.

[114] R. L. Johannes, R. Haydock, and V. Heine, "Phase Stability in Transition-Metal Laves Phases," *Physical Review Letters*, vol. 36, pp. 372–376, feb 1976.

[115] W. Brückner, R. Perthel, K. Kleinstück, and G. E. R. Schulze, "Magnetic Properties of $ZrFe_2$ and $TiFe_2$ within Their Homogeneity Range," *Physica Status Solidi (b)*, vol. 29, no. 1, pp. 211–216, 1968.

[116] E. W. Singleton, J. Strzeszewski, and G. C. Hadjipanayis, "High coercivity in rapidly quenched $Sm(Fe,T)_{12}$-type magnets," *Applied Physics Letters*, vol. 54, no. 19, pp. 1934–1936, 1989.

[117] J. Wecker, M. Katter, K. Schnitzke, and L. Schultz, "Magnetic hardening of Sm-Fe-Ti alloys," *Journal of Applied Physics*, vol. 67, pp. 4951–4953, may 1990.

[118] "Economic advantages, european powder metallurgy association." `https://www.epma.com/powder-metallurgy-economic-advantages`. Accessed: 2019-05-08.

[119] Z. Q. Jin, X. K. Sun, W. Liu, X. G. Zhao, Q. F. Xiao, Y. C. Sui, Z. D. Zhang, Z. G. Wang, and H. X. Qin, "Dependence of magnetic properties on microstructure in mechanically alloyed Nd-Fe-Ti-N," *Journal of Magnetism and Magnetic Materials*, vol. 169, no. 1-2, pp. 135–144, 1997.

[120] Z.-q. Jin, X. K. Sun, W. Liu, X. G. Zhao, Q. F. Xiao, Y. C. Sui, Z. D. Zhang, and Z. Wang, "Structure and magnetic properties of mechanical alloyed NdFeTi compounds and their nitrides," *Journal of Applied Physics*, vol. 79, no. 8, p. 5525, 2002.

[121] J. Ding, P. McCormick, and R. Street, "Mechanically alloyed $R11Fe_{84}Ti_5$ with R = Nd and Sm and their nitrides," *Journal of Alloys and Compounds*, vol. 217, pp. 108–111, jan 1995.

[122] S. L. Tang, C. H. Wu, B. W. Wang, X. M. Jin, G. S. Li, B. Z. Ding, and Y. C. Chuang, "Nonequilibrium phase transformation of $NdFe_{11}Ti$ compound during mechanical milling," *Journal of Magnetism and Magnetic Materials*, vol. 188, no. 3, pp. 387–392, 1998.

[123] S. Sugimoto, T. Shimono, H. Nakamura, T. Kagotani, M. Okada, and M. Homma, "Magnetic properties and microstructures of the $(SmFe_{10}V_2)_{1-x}$ $(Sm_2Fe_{17})_x$ cast alloys," *Materials Chemistry and Physics*, vol. 42, no. 95, pp. 298–301, 1995.

[124] J. Cannon, D. Robertson, and H. Hall, "Synthesis of lanthanide-iron laves phases at high pressures and temperatures," *Materials Research Bulletin*, vol. 7, pp. 5–11, jan 1972.

[125] H. Samata, N. Fujiwara, Y. Nagata, T. Uchida, and M. D. Lan, "Crystal Growth and Magnetic Properties of $SmFe_2$," *Japanese Journal of Applied Physics*, vol. 37, pp. 5544–5548, oct 1998.

[126] F. H. Ellinger and W. H. Zachariasen, "The Crystal Structure of Samarium Metal and of Samarium Monoxide," *Journal of the American Chemical Society*, vol. 75, pp. 5650–5652, nov 1953.

[127] A. H. Daane, R. E. Rundle, H. G. Smith, and F. H. Spedding, "The crystal structure of samarium," *Acta Crystallographica*, vol. 7, pp. 532–535, sep 1954.

[128] G. J. McCarthy and J. J. Rhyne, *The Rare Earths in Modern Science and Technology*. Springer US, 1978.

[129] A. Jayaraman and R. C. Sherwood, "Phase Transformation in Samarium Induced by High Pressure and Its Effect on the Antiferromagnetic Ordering," *Phys. Rev.*, vol. 134, pp. A691–A692, May 1964.

[130] A. Jayaraman, "Solid-Liquid and Solid-Solid Transformations in the Rare-Earth Metals at High Pressures," *Phys. Rev.*, vol. 139, pp. A690–A696, Aug 1965.

[131] N. Shi and D. Fort, "Preparation of samarium in the double hexagonal close packed form," *Journal of the Less Common Metals*, vol. 113, no. 2, pp. 21–23, 1985.

[132] L. Schultz, K. Schnitzke, and J. Wecker, "High coercivity in mechanically alloyed Sm-Fe-V magnets with a $ThMn_{12}$ crystal structure," *Applied Physics Letters*, vol. 56, pp. 868–870, feb 1990.

[133] V. M. Goldschmidt, F. Ulrich, and Barth, "Geochemical distribution laws of the elements. IV. The crystal structure of the oxides of the rare earth metals.," *Skrifter utgit av det norske Videnskap-Akademii Oslo. (I) Matem.-Naturvid. Klasse*, vol. 5, 1925.

[134] F. Pinkerton and D. Van Wingerden, "Magnetic hardening of $SmFe_{10}V_2$ by melt-spinning," *IEEE Transactions on Magnetics*, vol. 25, no. 5, pp. 3306–3308, 1989.

[135] J. Ding and M. Rosenberg, "Magnetic hardening of melt-spun and crystallized Sm-Fe-V and Sm-(Fe, Co)-V alloys," *Journal of The Less-Common Metals*, vol. 161, no. 2, pp. 369–374, 1990.

[136] Y. Wang and G. Hadjipanayis, "Magnetic properties of Sm-Fe-Ti-V alloys," *Journal of Magnetism and Magnetic Materials*, vol. 87, pp. 375–378, jul 1990.

[137] Y. Wang, G. C. Hadjipanayis, A. Kim, N. C. Liu, and D. J. Sellmyer, "Magnetic and structural studies in Sm-Fe-Ti magnets," *Journal of Applied Physics*, vol. 67, pp. 4954–4956, may 1990.

[138] B. M. Ma, W. L. Liu, Y. L. Liang, D. W. Scott, and C. Bounds, "Comparison of the improvement of thermal stability of NdFeB sintered magnets: Intrinsic and/or microstructural," *Journal of Applied Physics*, vol. 75, no. 1, pp. 6628–6630, 1994.

[139] H. Kim, Y. Kim, and H. Kim, "Magnetic properties and texture of NdFeB magnets fabricated by current-applied-pressure-assisted process," *Journal of Magnetism and Magnetic Materials*, vol. 224, pp. 173–179, mar 2001.

[140] K. Khlopkov, O. Gutfleisch, R. Schäfer, D. Hinz, K. H. Müller, and L. Schultz, "Interaction domains in die-upset NdFeB magnets in dependence on the degree of deformation," *Journal of Magnetism and Magnetic Materials*, vol. 272-276, no. SUPPL. 1, pp. 2003–2005, 2004.

[141] R. Lee, E. Brewer, and N. Schaffel, "Processing of Neodymium-Iron-Boron melt-spun ribbons to fully dense magnets," *IEEE Transactions on Magnetics*, vol. 21, pp. 1958–1963, sep 1985.

[142] J. C. Slater, "Atomic Radii in Crystals," *The Journal of Chemical Physics*, vol. 41, pp. 3199–3204, nov 1964.

[143] R. Madugundo and G. C. Hadjipanayis, "Anisotropic Mn-Al-(C) hot-deformed bulk magnets," *Journal of Applied Physics*, vol. 119, p. 013904, jan 2016.

[144] Y. Sakamoto, A. Ibata, S. Kojima, and T. Ohtani, "New MnAlC permanent magnets exhibiting macroscopically-plane magnetic-anisotropy," *IEEE Transactions on Magnetics*, vol. 16, pp. 1056–1058, sep 1980.

[145] L. Schultz and J. Wecker, "Coercivity in $ThMn_{12}$-type magnets," *Journal of Applied Physics*, vol. 64, no. 15 November, pp. 5711–5713, 1988.

[146] "List of data references for chemical elements." `https://en.wikipedia.org/wiki/List_of_data_references_for_chemical_elements`. Accessed: 2019-07-22.